

# Cubosome and Hexosome Microparticles: Shape, Rheology, and Templating

**Haiqiao Wang**

A thesis submitted in fulfilment  
of the requirements for the degree of  
Doctor of Philosophy



**UNSW**  
SYDNEY

**School of Chemical Engineering**  
**Faculty of Engineering**  
**University of New South Wales**

20 September 2019



# Thesis/Dissertation Sheet

Surname/Family Name	: Wang
Given Name/s	: Haiqiao
Abbreviation for degree as give in the University calendar	: PhD
Faculty	: Engineering
School	: Chemical Engineering
Thesis Title	: Cubosome and Hexosome Microparticles: Shape, Rheology, and Templating

Cubosomes and hexosomes are soft particles of cubic and hexagonal phases, formed by self-assembled amphiphilic lipids. They have attracted great attention because of applications in drug delivery. Cubosomes and hexosomes have been produced at the nanoscale, exhibiting unique shapes and symmetries, but a better understanding of links between particle shapes and mesoscale structures is needed for controlled production and broader applications.

In this thesis, a bottom-up method based on a precursor emulsion is developed to produce microscale cubosomes and hexosomes in a controlled way. Emulsion droplets containing water, ethanol, the lipid glyceryl monooleate, and the desired additives are suspended in a yield stress fluid, and transform into liquid crystals with solid-like rheology and controlled size and shape. Cubosomes are polyhedral particles formed by growing facets on precursor droplets. Hexosomes are bicones and spinning tops with rotational symmetry. Small angle X-ray scattering confirms the particles are cubosomes and hexosomes, and links particle shapes to microstructures. The micron-scale liquid crystalline particles provide a route to understanding the effects on production of soft particles with ordered microstructure and unique shapes.

The produced cubosomes and hexosomes are used as templates to polymerize various monomers and produce polymeric particles with unique micron-scale geometric shapes. The amphiphilicity of particles allows incorporation of various organic monomers. Photopolymerization in the lipid templates creates polymerized particles preserving the shapes of cubosomes and hexosomes. Particle shapes are controlled by varying the structures and hydrophobicity of the monomers. Monomers also control the elasticity of the final particles produced.

Although ultrasound is widely used to produce hexosomes in the top-down method, there are no direct studies of the process, and their effects on hexosome properties. We use high-speed microscopic imaging to directly observe bubble formation and degradation of bulk hexagonal phase, forming liquefied precursor materials that disperse and rapidly crystallize into hexosomes. Ultrasonic dispersal of the viscoelastic hexagonal phase is quantitatively related to the liquid crystal rheology, providing a process design basis as well as awareness of particle intermediate states that could affect short-time retention of solubilized active molecules.

## Declaration relating to disposition of project thesis/dissertation

I hereby grant to the University of New South Wales or its agents the right to archive and to make available my thesis or dissertation in whole or in part in the University libraries in all forms of media, now or here after known, subject to the provisions of the Copyright Act 1968. I retain all property rights, such as patent rights. I also retain the right to use in future works (such as articles or books) all or part of this thesis or dissertation.

I also authorise University Microfilms to use the 350 word abstract of my thesis in Dissertation Abstracts International (this is applicable to doctoral theses only).

.....

Signature

Witness Signature

Date

The University recognises that there may be exceptional circumstances requiring restrictions on copying or conditions on use. Requests for restriction for a period of up to 2 years must be made in writing. Requests for a longer period of restriction may be considered in exceptional circumstances and require the approval of the Dean of Graduate Research.

**FOR OFFICE USE ONLY** Date of completion of requirements for Award:



## Copyright Statement

I hereby grant The University of New South Wales or its agents the right to archive and to make available my thesis or dissertation in whole or part in the University libraries in all forms of media, now or hereafter known, subject to the provisions of the Copyright Act 1968. I retain all proprietary rights, such as patent rights. I also retain the right to use in future works (such as articles or books) all or part of this thesis or dissertation.

I also authorise University Microfilms to use the abstract of my thesis in Dissertation Abstract International (this is applicable to doctoral thesis only).

I have either used no substantial portions of copyright material in my thesis or I have obtained permission to use copyright material; where permission has not been granted I have applied/will apply for a partial restriction of the digital copy of my thesis or dissertation.

Signed .....

Date .....

## Authenticity Statement

I certify that the Library deposit digital copy is a direct equivalent of the final officially approved version of my thesis. No emendation of content has occurred and if there are any minor variations in formatting, they are the result of the conversion to digital format.

Signed .....

Date .....



## **Originality Statement**

I hereby declare that this submission is my own work and to the best of my knowledge it contains no material previously published or written by another person, or substantial portions of material which have been accepted for the award of any other degree or diploma at UNSW or any other educational institute, except where due acknowledgment is made in the thesis. Any contribution made to the research by others, with whom I have worked at UNSW or elsewhere, is explicitly acknowledged in the thesis. I also declare that the intellectual content of this thesis is the product of my own work, except to the extent that assistance from others in the project's design and conception or in style, presentation and linguistic expression is acknowledged.

Signed .....

Date .....





## INCLUSION OF PUBLICATIONS STATEMENT

UNSW is supportive of candidates publishing their research results during their candidature as detailed in the UNSW Thesis Examination Procedure.

**Publications can be used in their thesis in lieu of a Chapter if:**

- The student contributed greater than 50% of the content in the publication and is the “primary author”, ie. the student was responsible primarily for the planning, execution and preparation of the work for publication
- The student has approval to include the publication in their thesis in lieu of a Chapter from their supervisor and Postgraduate Coordinator.
- The publication is not subject to any obligations or contractual agreements with a third party that would constrain its inclusion in the thesis

Please indicate whether this thesis contains published material or not.

- This thesis contains no publications, either published or submitted for publication (if this box is checked, you may delete all the material on page 2)*
- Some of the work described in this thesis has been published and it has been documented in the relevant Chapters with acknowledgement (if this box is checked, you may delete all the material on page 2)*
- This thesis has publications (either published or submitted for publication) incorporated into it in lieu of a chapter and the details are presented below*

### CANDIDATE’S DECLARATION

I declare that:

- I have complied with the Thesis Examination Procedure
- where I have used a publication in lieu of a Chapter, the listed publication(s) below meet(s) the requirements to be included in the thesis.

<b>Name</b> Haiqiao Wang	<b>Signature</b>	<b>Date (dd/mm/yy)</b>
-----------------------------	------------------	------------------------

### Postgraduate Coordinator’s Declaration (to be filled in where publications are used in lieu of Chapters)

I declare that:

- the information below is accurate
- where listed publication(s) have been used in lieu of Chapter(s), their use complies with the Thesis Examination Procedure
- the minimum requirements for the format of the thesis have been met.

<b>PGC’s Name</b>	<b>PGC’s Signature</b>	<b>Date (dd/mm/yy)</b>
-------------------	------------------------	------------------------

For each publication incorporated into the thesis in lieu of a Chapter, provide all of the requested details and signatures required

<b>Details of publication #1:</b>					
<i>Full title:</i> Soft polyhedral particles based on cubic liquid crystalline emulsion droplets					
<i>Authors:</i> Haiqiao Wang, Per B. Zetterlund, Cyrille Boyer, Ben J. Boyd, Stuart W. Prescott, Patrick T. Spicer					
<i>Journal or book name:</i> Soft Matter					
<i>Volume/page numbers:</i> 13, 8492-8501					
<i>Date accepted/ published:</i> 25 October 2017					
<b>Status</b>	<i>Published</i>	<b>Yes</b>	<i>Accepted and In press</i>		<i>In progress (submitted)</i>
<b>The Candidate's Contribution to the Work</b>					
I'm the first author of the article					
<b>Location of the work in the thesis and/or how the work is incorporated in the thesis:</b>					
Chapter 2					
<b>Primary Supervisor's Declaration</b>					
I declare that:					
<ul style="list-style-type: none"> <li>the information above is accurate</li> <li>this has been discussed with the PGC and it is agreed that this publication can be included in this thesis in lieu of a Chapter</li> <li>All of the co-authors of the publication have reviewed the above information and have agreed to its veracity by signing a 'Co-Author Authorisation' form.</li> </ul>					
<i>Supervisor's name</i>		<i>Supervisor's signature</i>		<i>Date (dd/mm/yy)</i>	
Patrick T. Spicer					

<b>Details of publication #2:</b>					
<i>Full title:</i> Large Hexosomes from Emulsion Droplets: Particle Shape and Mesostructure Control					
<i>Authors:</i> Haiqiao Wang, Per B. Zetterlund, Cyrille Boyer, Ben J. Boyd, Timothy J. Atherton, Patrick T. Spicer					
<i>Journal or book name:</i> Langmuir					
<i>Volume/page numbers:</i> 34, 13662-13671					
<i>Date accepted/ published:</i> 15 October 2018					
<b>Status</b>	<i>Published</i>	<b>Yes</b>	<i>Accepted and In press</i>		<i>In progress (submitted)</i>
<b>The Candidate's Contribution to the Work</b>					
I'm the first author of the article					
<b>Location of the work in the thesis and/or how the work is incorporated in the thesis:</b>					
Chapter 3					
<b>Primary Supervisor's Declaration</b>					
I declare that:					
<ul style="list-style-type: none"> <li>the information above is accurate</li> <li>this has been discussed with the PGC and it is agreed that this publication can be included in this thesis in lieu of a Chapter</li> <li>All of the co-authors of the publication have reviewed the above information and have agreed to its veracity by signing a 'Co-Author Authorisation' form.</li> </ul>					
<i>Supervisor's name</i>		<i>Supervisor's signature</i>		<i>Date (dd/mm/yy)</i>	
Patrick T. Spicer					

<b>Details of publication #3:</b>					
<b>Full title:</b> Polymerization of cubosome and hexosome templates to produce complex microparticle shapes					
<b>Authors:</b> Haiqiao Wang, Per B. Zetterlund, Cyrille Boyer, Patrick T. Spicer					
<b>Journal or book name:</b> Journal of Colloid and Interface Science					
<b>Volume/page numbers:</b> 546, 240-250					
<b>Date accepted/ published:</b> 22 March 2019					
<b>Status</b>	<i>Published</i>	<b>Yes</b>	<i>Accepted and In press</i>		<i>In progress (submitted)</i>
<b>The Candidate's Contribution to the Work</b>					
<b>I'm the first author of the article</b>					
<b>Location of the work in the thesis and/or how the work is incorporated in the thesis:</b>					
<b>Chapter 4</b>					
<b>Primary Supervisor's Declaration</b>					
I declare that:					
<ul style="list-style-type: none"> <li>• the information above is accurate</li> <li>• this has been discussed with the PGC and it is agreed that this publication can be included in this thesis in lieu of a Chapter</li> <li>• All of the co-authors of the publication have reviewed the above information and have agreed to its veracity by signing a 'Co-Author Authorisation' form.</li> </ul>					
<b>Supervisor's name</b> Patrick T. Spicer		<b>Supervisor's signature</b>		<b>Date (dd/mm/yy)</b>	



## Abstract

Cubosomes and hexosomes are soft particles of cubic and hexagonal phases, formed by self-assembled amphiphilic lipids. They have attracted great attention because of applications in drug delivery. Cubosomes and hexosomes have been produced at the nanoscale, exhibiting unique shapes and symmetries, but a better understanding of links between particle shapes and mesoscale structures is needed for controlled production and broader applications.

In this thesis, a bottom-up method based on a precursor emulsion is developed to produce microscale cubosomes and hexosomes in a controlled way. Emulsion droplets containing water, ethanol, the lipid glyceryl monooleate, and the desired additives are suspended in a yield stress fluid, and transform into liquid crystals with solid-like rheology and controlled size and shape. Cubosomes are polyhedral particles formed by growing facets on precursor droplets. Hexosomes are bicones and spinning tops with rotational symmetry. Small angle X-ray scattering confirms the particles are cubosomes and hexosomes, and links particle shapes to microstructures. The micron-scale liquid crystalline particles provide a route to understanding the effects on production of soft particles with ordered microstructure and unique shapes.

The produced cubosomes and hexosomes are used as templates to polymerize various monomers and produce polymeric particles with unique micron-scale geometric shapes. The amphiphilicity of particles allows incorporation of various organic monomers. Photopolymerization in the lipid templates creates polymerized particles preserving the shapes of cubosomes and hexosomes. Particle shapes are controlled by varying the structures and hydrophobicity of the monomers. Monomers also control the elasticity of the final particles produced.

Although ultrasound is widely used to produce hexosomes in the top-down method, there are no direct studies of the process, and their effects on hexosome properties. We use high-speed microscopic imaging to directly observe bubble formation and degradation of bulk hexagonal phase, forming liquefied precursor materials that disperse and rapidly crystallize into hexosomes. Ultrasonic dispersal of the viscoelastic hexagonal phase is quantitatively related to the liquid crystal rhe-

ology, providing a process design basis as well as awareness of particle intermediate states that could affect short-time retention of solubilized active molecules.

## Acknowledgments

First I have my supervisor A/Prof Patrick Spicer to thank for all the great instructions, suggestions, and help. You not only guide me through my research, but also help me to find my passion. Thank you for giving me so much encouragement and confidence, and making my four-year PhD so fantastic and unforgettable. Working with you has a profound impact on how I think not only about colloid science, but also about the promising future.

I would like to express my gratitude to my joint supervisors Prof Per Zetterlund and Prof Cyrille Boyer, for all the support and guidance on the project. I'm also grateful to Dr Stuart Prescott for great help and valuable advice and discussions in group meeting.

I would like to thank Prof Ben Boyd (Monash University) for the help with experiment at Australian Synchrotron SAXS and helpful discussions of cubosomes and hexosomes.

I'm grateful to A/Prof Timothy Atherton (Tufts University) for discussions of hexosome shape and microstructure, and Dr Jiangtao Xu for help with photopolymerization.

Thanks to Dr Vincent Poulichet for ultrasound device set-up and experiment design.

I would like to thank Mr Seth Lindberg and Dr Marco Caggioni (Procter & Gamble Company, USA) for financial support, and UNSW School of Chemical Engineering for PhD scholarship.

Many thanks to Camillo Taraborrelli and Eh Hau Pan for lab and instrument management. And thanks to EMU for providing facilities, and the help of Dr Yin Yao with SEM.

Thanks to all the Complex Fluids group members: Jie, Goldina, Zengyi, Prerna, Vincent, Matthew, Isaac, Wenjia, Zhiwei, Haoda, Hao, Firoozeh, Maryam, Aline. Thank you for making the lab a place with enjoyable atmosphere. It's a great thing to have all of you as my colleagues and friends throughout my PhD.

Thanks to all my friends in CAMD: Dewen, Sam, Jiacheng, Zhai, Haiwang, Cheng, Fumi, Awin, Yasemin, Siva, Kenward, Susan, Nat, Zixuan, Henry, Gervase, Yingying,

Yiting, Huijie, Tony, Guofeng, Chenyu, Liwen, and Zilong. Our friendship is a fortune in my life.

Finally, I acknowledge my parents and grandparents for encouraging me to pursue my dreams, and always giving me support and unconditional love.



# Contents

<b>Abstract</b>	<b>i</b>
<b>1 Introduction</b>	<b>1</b>
1.1 Bicontinuous cubic phase and hexagonal phase . . . . .	1
1.2 Progress in cubosomes and hexosomes . . . . .	7
1.2.1 Microstructure and particle shapes . . . . .	7
1.2.2 Design of amphiphiles . . . . .	11
1.2.3 Design of preparation methods . . . . .	12
1.2.4 Applications in drug delivery . . . . .	15
1.3 Particle preparation with controlled shapes . . . . .	17
1.4 Shape preservation from templates . . . . .	18
1.5 Project aims and overview . . . . .	20
1.6 References . . . . .	22
<b>2 Soft polyhedral particles based on emulsion droplets</b>	<b>29</b>
2.1 Introduction . . . . .	29
2.2 Materials and methods . . . . .	31
2.3 Results and discussion . . . . .	34
2.3.1 Transition from droplets to cubosomes . . . . .	34
2.3.2 Effects of precursor droplet size . . . . .	41
2.3.3 Additive effects on surface and molecular packing . . . . .	43
2.3.4 Anisotropy in composition and deformation . . . . .	47
2.4 Conclusions . . . . .	51
2.5 References . . . . .	52
<b>3 Large hexosomes from emulsion droplets</b>	<b>57</b>
3.1 Introduction . . . . .	57
3.2 Materials and Methods . . . . .	62
3.3 Results and discussion . . . . .	65
3.3.1 Formation of microscale hexosomes from droplets . . . . .	65
3.3.2 Shape and phase transition by hydrophobic additives . . . . .	68

3.3.3	Elasticity of hexosomes . . . . .	74
3.3.4	Ordered microstructure in hexosomes . . . . .	76
3.4	Conclusions . . . . .	80
3.5	References . . . . .	80
<b>4</b>	<b>Polymerization of cubosome and hexosome templates</b>	<b>87</b>
4.1	Introduction . . . . .	87
4.2	Materials and methods . . . . .	89
4.3	Results and discussion . . . . .	91
4.3.1	Template synthesis . . . . .	91
4.3.2	Polymerization of hexosomes by hydrophobic monomers . . . . .	92
4.3.3	Polymerization of cubosomes by hydrophobic monomers . . . . .	97
4.3.4	Soft polymerized particles by hydrophilic monomer . . . . .	99
4.4	Conclusions . . . . .	107
4.5	References . . . . .	108
<b>5</b>	<b>Particle-scale studies of hexosome formation by ultrasonication</b>	<b>113</b>
5.1	Introduction . . . . .	113
5.2	Materials and methods . . . . .	115
5.3	Results and discussion . . . . .	116
5.4	Conclusions . . . . .	124
5.5	References . . . . .	125
<b>6</b>	<b>Conclusions and future work</b>	<b>129</b>
<b>A</b>	<b>Supplementary Figures for Chapter 3</b>	<b>135</b>
<b>B</b>	<b>Supplementary Figures for Chapter 4</b>	<b>139</b>

# Chapter 1

## Introduction

### 1.1 Bicontinuous cubic phase and hexagonal phase

Amphiphilic lipids can self-assemble and form liquid crystal phases of different microstructures depending on the intrinsic molecular geometry. The dimensionless shape parameter, critical packing parameter (CPP), provides a useful measure of molecular shape to predict the aggregation behavior.<sup>1,2</sup> As Figure 1.1 shows, when  $CPP < 1$ , normal phases are formed, such as the normal micelle ( $L_1$ ), bicontinuous cubic phase ( $V_1$ ) and hexagonal phase ( $H_1$ ). When  $CPP = 1$ , lipids aggregate into lamellar phase ( $L_\alpha$ ). With  $CPP > 1$ , reversed phases are developed, for example the reversed bicontinuous cubic phase ( $V_2$ ), reversed hexagonal ( $H_2$ ) phase, and the reversed micelle ( $L_2$ ).<sup>3</sup>

In these phases,  $V_2$  and  $H_2$  phases have attracted the greatest attention due to the unique microstructures and macroscopic properties. In  $V_2$  phase, there are two networks of non-intersecting water nanochannels embedded in the hydrophobic matrices.<sup>4</sup> Basically the  $V_2$  phase is composed of lipid bilayers. The bilayers are curved and arranged in periodic three-dimensional cubic-lattice micro-structures. The contorted bilayers are in the shape of infinite periodic minimal surfaces (IPMS), similar to a saddle. On the surface, the mean curvature at any point is zero.<sup>5-7</sup> Based on the X-ray crystallographic investigations, there are three forms of bicontinuous cubic phase: diamond  $Pn3m$  (D), gyroid  $Ia3d$  (G), and primitive  $Im3m$  (P).<sup>8</sup> The

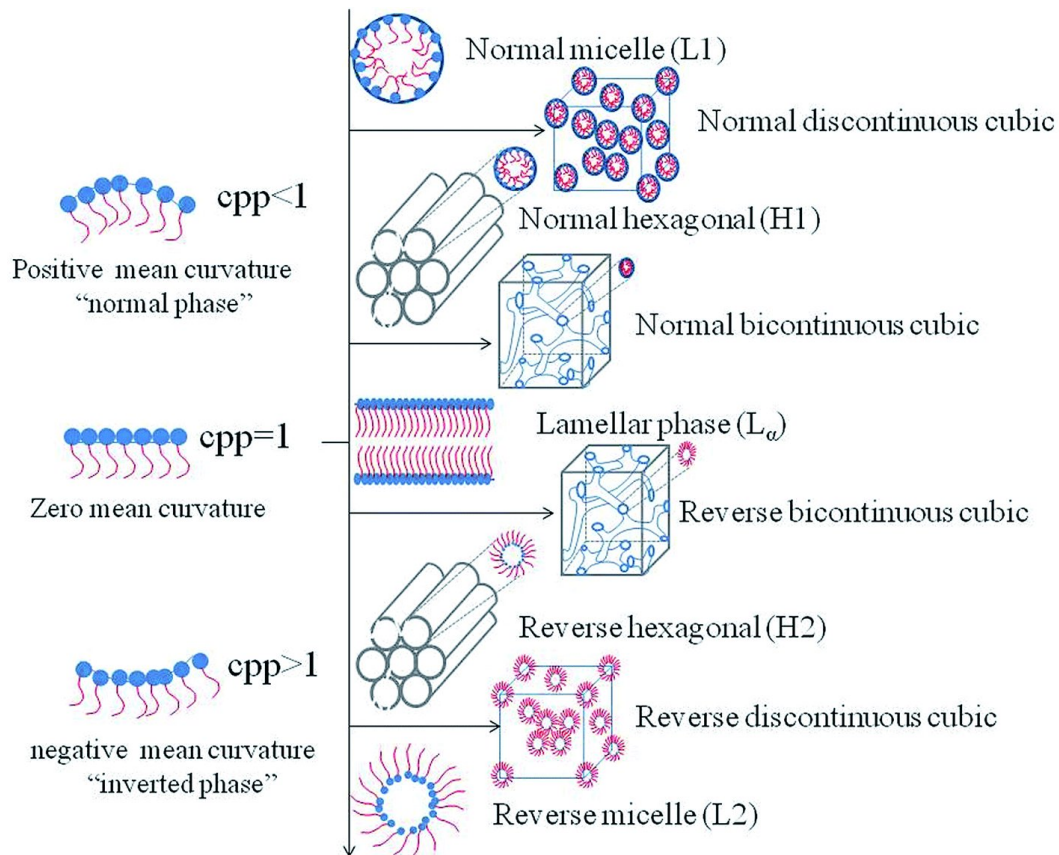


**Figure 1.1:** Schematic representations of common structures and their corresponding CPP.<sup>3</sup>

three unit cells are shown in Figure 1.2.<sup>9</sup> The bulk phase of  $V_2$  is a gel material which is temperature-stable, and optically isotropic with a high elastic modulus of about  $10^5$  Pa.<sup>6,7,10</sup>

In  $H_2$  phase, amphiphilic lipids are self-assembled into cylindrical micelles and pack in a two-dimensional hexagonal lattice, as in Figure 1.3a.<sup>11</sup> The hexagonal lattice plane is perpendicular to cylindrical axis, and water channels pass through the core of each cylinder.<sup>12</sup> Hexagonal phase is optically anisotropic and birefringent. The birefringence textures performed by  $H_2$  phase in polarizing microscopy are related to defects and certain arrangement of microstructure.<sup>13,14</sup> There are different configurations formed in the bulk  $H_2$  phase. Because of the elastic strain energy of

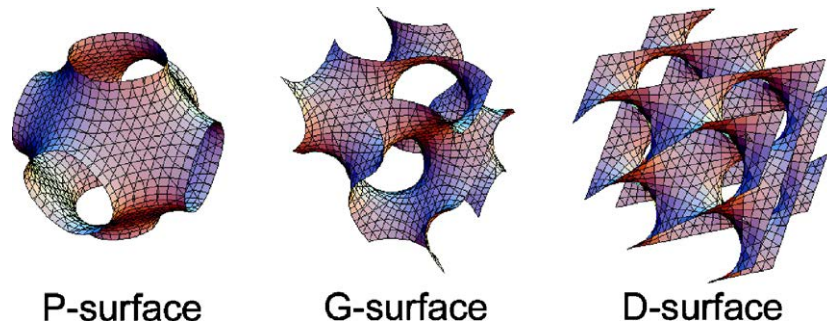


**Figure 1.2:** Calculated approximate representations of the cubic unit cells most frequently encountered in aqueous surfactant systems.<sup>9</sup>

cylindrical micelles, deformations such as bending, splay, and twist of cylinders are common, and result in multi-domain phases.<sup>15,16</sup> In the confinement of different length scales, two monodomains of  $H_2$  phase form, as in Figure 1.3b and c.<sup>11</sup> Straight cylinders with undulation are observed in capillaries with a diameter of 1.0 mm or a similar equivalent size.<sup>11,17</sup> Cylindrical micelles are parallel (Figure 1.3b), and show a bright and stripe pattern because of the undulation induced by thermomechanical instability.<sup>18</sup> Formation of the other configuration, like ringed cylinders, needs a smaller length scale, for example in a 0.2 mm diameter capillary. In this case, the closed cylindrical micelles rotate around the central long axis of the capillary (Figure 1.3c) with a colorful and symmetric birefringence pattern.

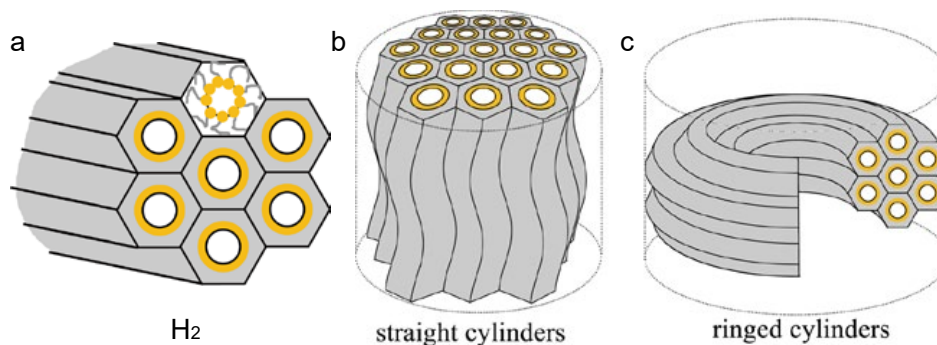


**Figure 1.3:** (a) Cross section of  $H_2$  phase microstructure: cylindrical micelles are stacked to form the hexagonal lattice. Two arrangements of cylinders of the  $H_2$  phase: (b) straight cylinders with undulation and (c) ringed cylinders.<sup>11</sup>

The inverse hexagonal phase can be prepared from cubic phase by increasing the CPP of lipids. There are various ways to trigger the phase transition from  $V_2$  to  $H_2$  phase. For example, addition of hydrophobic molecules increases the effective volume of the lipid hydrocarbons, increases the negative curvature, and consequently transforms the contorted bicontinuous bilayers to hexagonally packed cylinders.<sup>19–22</sup> Increasing temperature,<sup>23,24</sup> and adjusting pH<sup>25,26</sup> have the same effect on microstructure and also cause the phase transition.

The bulk  $H_2$  phase is a highly viscoelastic gel-like material. Figure 1.4 shows that the elastic modulus of  $H_2$  phase is about  $10^4$  Pa, one magnitude lower than  $V_2$  phase at the same composition formed, after phase transition when temperature is increased.<sup>27</sup> The rheological properties of  $H_2$  phase can be further adjusted by varying the composition and microstructural reorientation, which will be discussed with experimental results in Chapter 3 and Chapter 5.

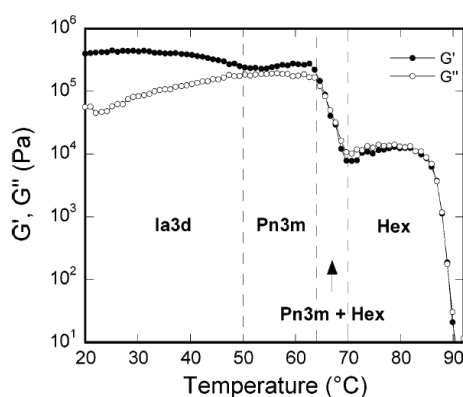


**Figure 1.4:** Elastic modulus  $G'$ , and viscous modulus  $G''$  as a function of temperature for the system formed by 80 wt% Dimodan UIJ (commercial-grade form of monolinolein) and 20 wt% water.<sup>27</sup>

Small-angle X-ray scattering (SAXS) is a powerful structural method, and it is indispensable for confirmation of liquid crystalline phases. The position of Bragg peaks with scattering vector  $q$  is related to the nature of each phase. The phase type is identified by correlating  $q$  values of peaks with Miller indices ( $hkl$ ) for known

## 1.1. Bicontinuous cubic phase and hexagonal phase

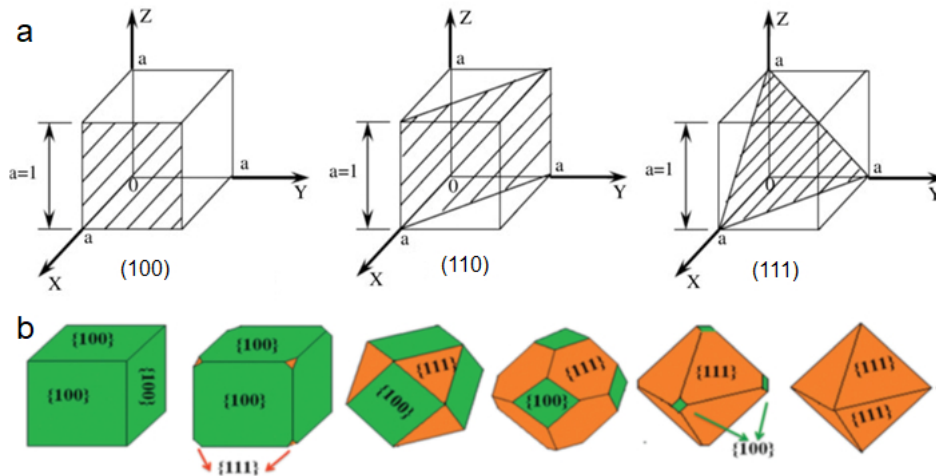


**Figure 1.5:** (a) Miller indices of facets in a cubic crystal;<sup>29</sup> (b) shapes of polyhedra with different ratios of (100) to (111) facets.<sup>30</sup>

phases. For example, the ratio of  $\sqrt{2} : \sqrt{3} : \sqrt{4}$  corresponds to bicontinuous  $Pn3m$  phase, and the ratio of  $\sqrt{1} : \sqrt{3} : \sqrt{4}$  is the characteristic for hexagonal phase ( $p6mm$ ). The lattice parameters of the microstructure can be calculated using the  $q$  value of the first peak and the corresponding  $hkl$ .<sup>28</sup>

Miller indices ( $hkl$ ) are a set of numbers which represent the orientation of a facet in crystal by considering how the facet intersects the main crystallographic axes. In a cubic unit cell, Miller indices of a facet are the reciprocals of the fractional intercepts on the  $x$ ,  $y$ , and  $z$  axes, as shown in Figure 1.5a.<sup>29</sup> The shape of crystal is determined by the relative growth rates different crystal facets. During crystal growth, the shape can change if there is a mix of different facets on the surface. Figure 1.5b shows shapes of a cubic crystal with different ratios of (100) and (111) facets. The single crystal can evolve from a cube to a cuboctahedron and then to an octahedron, with an increasing ratio of (111) to (100) facet areas.<sup>30,31</sup>

One of the most studied systems of lyotropic liquid crystal is monoolein-water, which has rich phase behavior, as shown in Figure 1.6.<sup>32</sup> Monoolein is the most commonly used lipid of all the monoacylglycerols, as liquid crystalline phases of  $L_\alpha$ ,

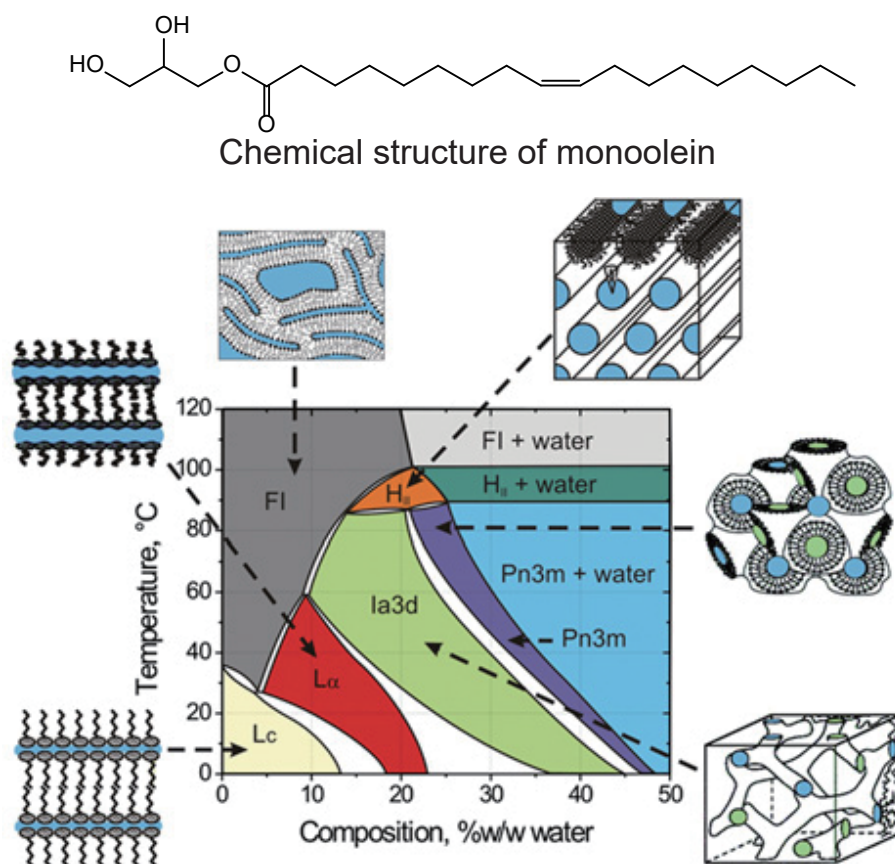


**Figure 1.6:** Chemical structure of monoolein, and temperature-composition phase diagram of monoolein-water system with cartoon representations of the various phases.<sup>32</sup>

bicontinuous  $Ia3d$  and  $Pn3m$  form in the hydrating process at ambient temperature, and monoolein is commercially available in relatively high purity at a low cost.<sup>33</sup> Many works use optical microscopy observations and X-ray diffraction to complete the phase diagram in Figure 1.6,<sup>34–36</sup> and efforts have been taken to ensure it represents equilibrium behavior.<sup>33</sup> Monoolein is the lipid used for most experiments in this thesis.



## 1.2 Progress in cubosomes and hexosomes

The bulk  $V_2$  and  $H_2$  phase in equilibrium with excess water can be dispersed into particles, cubosomes and hexosomes respectively, in analogy with liposomes which are dispersed lamellar liquid crystalline particles. Due to the low solubility of lipids, after dispersing in aqueous phase, cubosomes and hexosomes can keep the same internal microstructure as in the bulk. These liquid crystalline particles were first made by Larsson in 1989 by shaking cubic monoolein-water phase in a bile salt solution.<sup>37</sup> The dispersion is kinetically stable with stabilizers like surfactants, block copolymers, and amphiphilic proteins.<sup>7</sup> The most used techniques for studying cubosomes and hexosomes are SAXS and cryo-electron microscopy (cryo-EM). Same as the bulk liquid crystalline phases, the phase of particles can be identified by SAXS. As liquid crystals cannot keep their structure without water, cryo-EM is the only way to observe particle morphology in nanoscale. Most studies of cubosomes and hexosomes are based on phase identification via SAXS and cryo-EM observations, and this section briefly describes recent progress in these particles.

### 1.2.1 Microstructure and particle shapes

Cubosomes and hexosomes are observed to be in unique shapes with certain symmetries, as the highly ordered microstructure and elasticity of  $V_2$  and  $H_2$  phase overwhelms fluid interfacial tension to keep the anisotropic shapes.

Cubosomes studied in most works are in the size range of 100 – 500 nm, and from cryo-TEM images, they are square, whether in the space group of  $Pn3m$  or  $Im3m$ , as shown in Figure 1.7. The light grey dots are alternating water channels, and the dark matrix is the oil channels, revealing a unit cell structure. Vesicles are often found

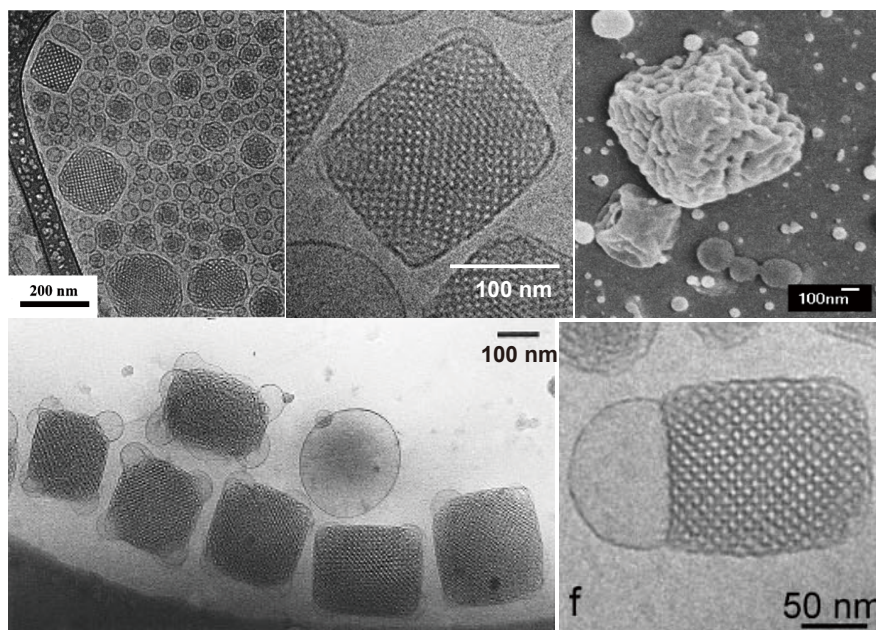


**Figure 1.7:** Cryo-EM images of cubosomes in nanoscale. Particles at the top are in the space group  $Pn3m$ , the bottom ones are  $Im3m$ .<sup>6,38–41</sup>

to coexist with cubosomes, and particles are covered with lamellar structures when block copolymers are used as stabilizer.<sup>40,42</sup>

However, cryo-TEM only gives information on two-dimensional shape, the three-dimensional shape is elusive. Other techniques are needed to obtain structures in three dimensions. The only work that studied cubosomes using cryo-SEM shows that three-dimensional cubosomes are polyhedra with facets, as the top right image shows in Figure 1.7.<sup>39</sup> Cryo-electron tomography (CET) is used to directly visualize the internal three-dimensional organization, the bicontinuous cubic structure, and the two independent water channels.<sup>43</sup> Observation of cubosomes, especially the three-dimensional structure, is limited by the difficult and complex sample preparations for cryo-EM. In order to study the phase and shape transition, cubosomes with larger sizes have been made to allow observations via optical microscopy.

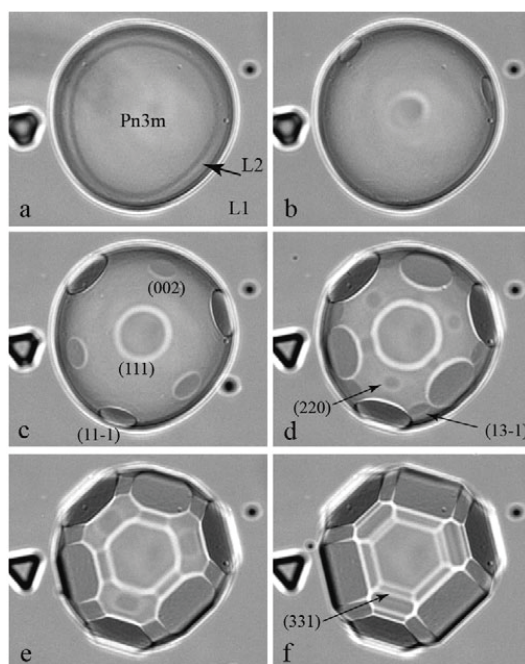


**Figure 1.8:** Variation of the shape of a  $Pn3m$ -in- $L1$  crystal of monoolein at  $58^\circ\text{C}$  due to lowering of the ethanol concentration in water in the isothermal phase transition.<sup>44</sup>

Pieranski and coworkers directly observe the formation of single cubosomes by depositing a drop of lipid with a diameter of  $100 - 500 \mu\text{m}$  on glass slide. With controlled humidity and temperature, the hemisphere of lipid can be gradually transformed into a faceted cubosome as water diffuses inside the lipid drop and induces formation of cubic phase.<sup>45</sup> Figure 1.8 shows the shape variation in an isothermal process where the lipid drop is immersed in the mixed solvent of water and ethanol. With decreasing ethanol concentration,<sup>6</sup> cubic phase forms and facets appear at the surface of drop. Facets grow over time and rough surfaces disappear in the meantime, and the drop crystallizes into a polyhedron with sharp edges.<sup>44</sup> The direct observation shows relation between the cubic microstructure and particle shape, and the indexed facets with different energies can be correlated with inorganic crystals, giving a better understanding of structures of not only liquid crystal but also

crystals in general.<sup>46,47</sup> Cubosomes in microscale are prepared in other ways and observed in optical microscopy in Chapter 2, demonstrating the similar formation process of crystallization and controlled particle shapes.

Hexosomes made in previous works were mostly nanoparticles, and they are the same as nanoscale cubosomes, requiring cryo-EM techniques for observation.<sup>20,48,49</sup> Common morphologies of hexosomes are summarized in Figure 1.9a. Two-dimensional structures obtained by cryo-TEM suggest that hexosomes can be in various shapes, including flat disk-like hexagonal prisms, spheres, twisted ellipsoids, and bicones.<sup>41,50,51</sup> Cryo-SEM imaging shows that some hexosomes adopt a spinning top shape, a short cylinder capped by a cone at both ends, and biconical shapes with a central raised spine, as shown in the bottom right smaller images in Figure 1.9a.<sup>52</sup>

Multiple mesostructures have been proposed to explain the different shapes based on the water channels observed in cryo-TEM images (Figures 1.9b and c). The flat hexagonal prisms are thought to be hexagonally packed cylindrical micelles aligned perpendicular to the largest face (Figure 1.9b).<sup>50</sup> Spherical and ellipsoidal hexosomes are drawn in Figure 1.9c, with cylindrical micelles curved into a circle or ellipse, and they are probably closed in some particles. The hexagonal array is normal to the cylinder axis.<sup>41</sup>

Although chromonic liquid crystal particles have different rheology and building blocks from hexosomes, they exhibit the same spinning top and biconical shapes as hexosomes observed in cryo-SEM. The shapes have rotating symmetry, with a microstructure of hexagonal columns curled around the central symmetry axis (Figure 1.9d) to minimize total interfacial energy.<sup>53</sup> This arrangement can also be found in microscale hexosomes with similar shapes and symmetry as described in Chapter 3.

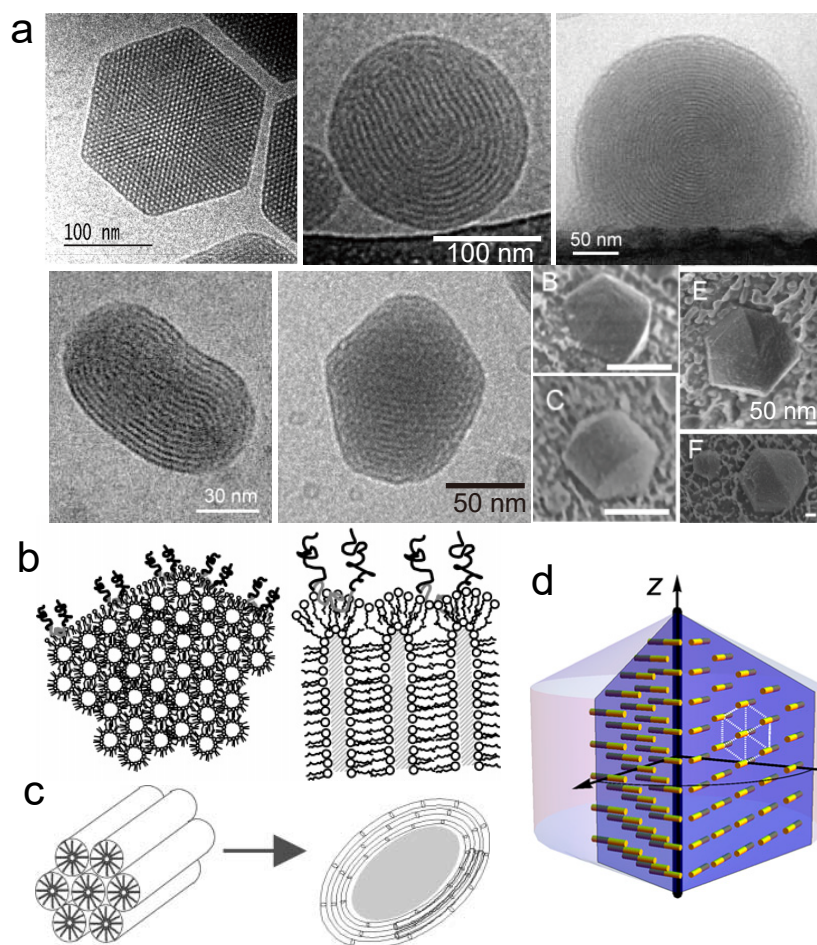


**Figure 1.9:** Morphology and microstructure of hexosomes: (a) cryo-EM images; (b-d) assumed microstructural arrangement based on observations.<sup>41,50-53</sup>

### 1.2.2 Design of amphiphiles

Principles for liquid crystalline particles design are summarized in a recent review.<sup>2</sup> The design rules are based on the non-covalent forces that drive amphiphile self-assembly, and give criteria for selecting for lipid and solvent.

Controlling bilayer curvature is an important way to change properties of liquid crystalline particles, including incorporating molecules with different geometries.<sup>12</sup> For example, cubosomes can be highly swollen by addition of the positively charged lipid DOTAP into monoolein.<sup>54</sup> The larger water channels in swollen cubosomes can

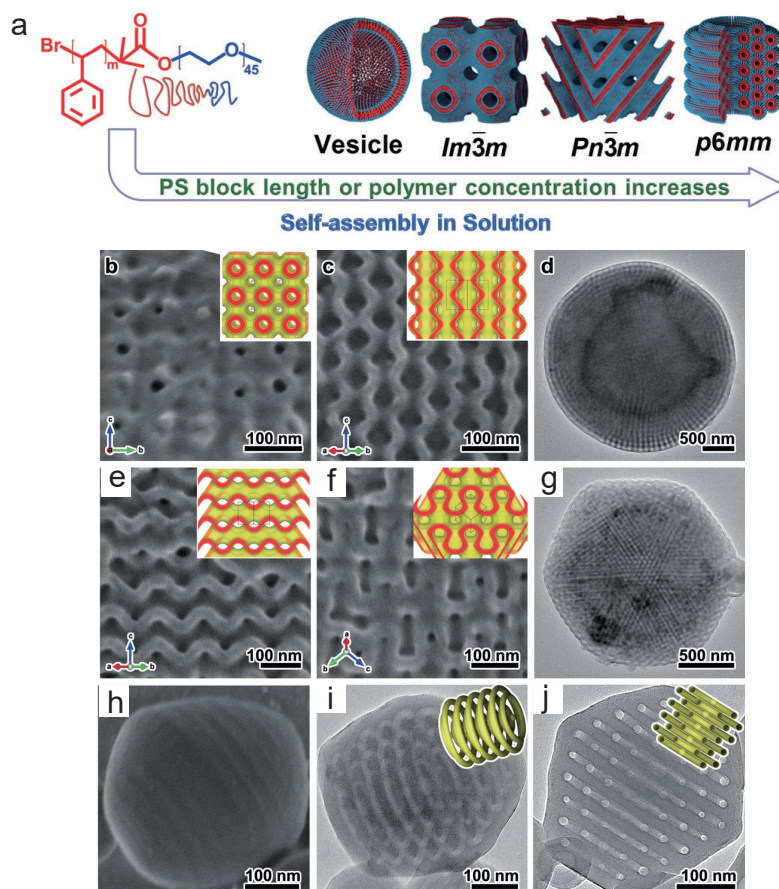
provide more space for crystallization of membrane protein.<sup>55</sup> Compositions are also adapted for specific applications. There are over 130 additives that have been incorporated in applicable cubosomes, especially bioactive lipids added to produce novel colloidal carriers.<sup>56,57</sup>

There are molecules designed and synthesized in order to make liquid crystalline structures with unique properties. Manni et al. synthesized a family of lipids which were modified by cyclopropyl in hydrophobic chains. They exhibit liquid crystalline phase behavior at low temperature which is different from normal lipids. Water inside the cubic and hexagonal structures are amorphous without forming ice due to nano-confinement.<sup>58</sup>

Synthetic amphiphilic block copolymers can self-assemble into cubosomes and hexosomes in aqueous solution by tailoring the volume fractions of the hydrophilic or hydrophobic block, as shown in Figure 1.10a.<sup>59,60</sup> These polymer analogues form the same liquid crystalline phases as in lipid systems but with larger sizes of water channels. Such inverse microstructures are rarely observed in most self-assembly of polymer. Polymers form stronger aggregates than lipid, which can keep the same structures without water, so cryo-EM is not necessary as it can be observed in EM. Figures 1.10b-j show particle morphologies and the well-defined interior structures obtained from TEM and SEM after freeze-drying. Due to the easier observation, cubosomes and hexosomes formed by block copolymers provide model systems for fundamental studies of self-assembly of lipids.<sup>61,62</sup>

### **1.2.3 Design of preparation methods**

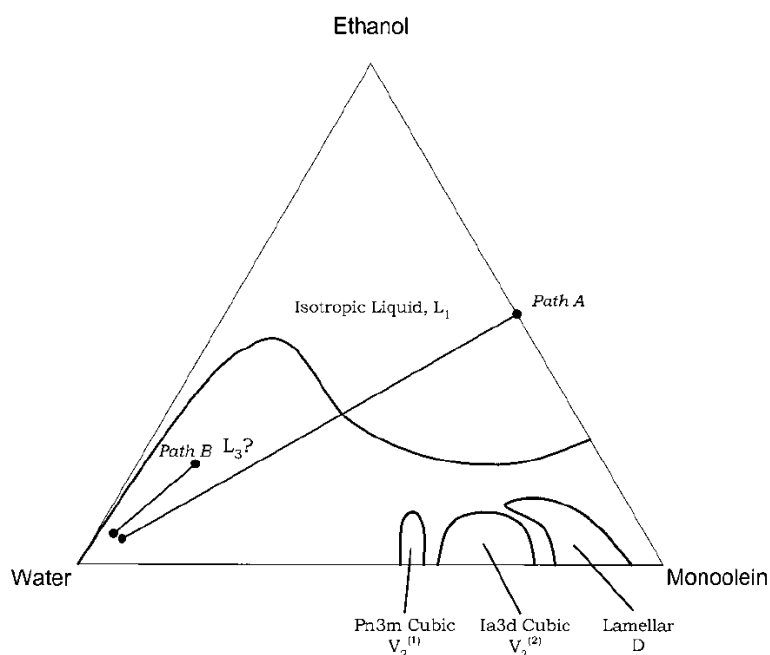
The most used method of production of liquid crystalline particles is the top-down approach. The bulk phase is made first by mixing lipid with water, producing an extremely viscous gel. Then the bulk phase is dispersed into nanoparticles in excess



**Figure 1.10:** Controlled self-assembly of PS-*b*-PEO into cubosomes and hexosomes: (a) schematic of self-assembly by tailoring the volume fraction of PS block; (b-j) EM images of *Im3m* cubosomes, *Pn3m* cubosomes, and *P6mm* hexosomes with structural models from top to bottom respectively.<sup>59</sup>

water with block copolymer as stabilizer. Due to the high viscoelasticity of the bulk phase, the dispersion process needs high energy, for example ultrasound or high-pressure homogenization.<sup>9,63</sup> So more methods have been developed in order to avoid high-energy processing, and make particle production more controllable.

A bottom-up process was developed to produce cubosomes, starting from water-like solutions rather than a bulk cubic phase gel.<sup>6</sup> The hydrotrope ethanol is included to dissolve the lipid monoolein and form an isotropic solution. After addition of water, nanoscale cubosomes form based on a homogeneous nucleation mechanism.



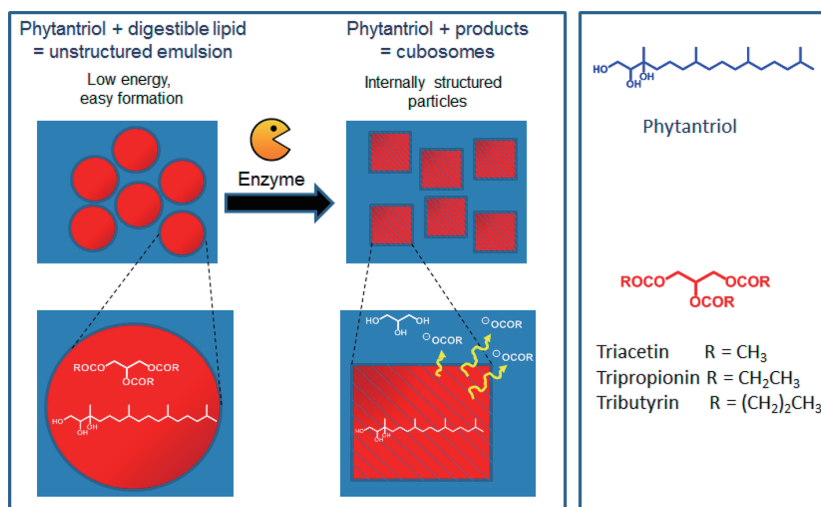
**Figure 1.11:** Ternary phase diagram for the monoolein-ethanol-water system. The system exhibits five single-phase regions, including four liquid crystalline phases, despite significant levels of ethanol hydrotrope. The large region of isotropic liquid provides broad flexibility for the formulation of precursors forming cubic gel and cubosome dispersions upon dilution.<sup>6</sup>

Figure 1.11 shows the phase diagram of monoolein-ethanol-water system, which is needed to design a formulation using a dilution approach. The line on the phase diagram is the dilution trajectory from the starting composition to a cubic phase-water miscibility gap. This process is versatile to accommodate different lipids and hydrotrope to produce cubosomes without using high-energy dispersion.<sup>63</sup>

Spray-drying of cubosome dispersions in aqueous solution, using starch as an encapsulant can produce powders of monoolein encapsulated in hollow starch shells. The shell can protect monoolein against powder cohesion. When rehydrated, powders form cubosomes again without shear, and starch act as a steric stabilizer. High shear dispersion can also be skipped in this method of cubosome production.<sup>64</sup>

Cubosomes have also been made from a low viscosity emulsion, containing both nondigestible lipid and digestible triglyceride, using enzymatic lipolysis. This process





**Figure 1.12:** Schematic illustration of lipolysis-induced transformation from a disordered emulsion to cubosomes.<sup>65</sup>

is illustrated in Figure 1.12: a precursor of disordered emulsion droplets undergoes phase transition to cubosomes after digestion of triglyceride and release of digestion products, leaving the non-digestible lipid to form cubosomes in excess aqueous solution.<sup>65,66</sup> Similarly, liquid crystalline particles are formed from fat droplets during the digestion of milk, and can act as a controlled release system for nutrients.<sup>67,68</sup> The digestion approach provides a "sideway" method to avoid problems in top-down and bottom-up methods of particle production.

Another bottom-up approach of evaporating hydrotrope has been developed according to the phase diagram in Figure 1.11. Microscale cubosomes and hexosomes with unique shapes are produced, and this method is described in Chapters 2-4.

### 1.2.4 Applications in drug delivery

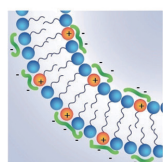
The three-dimensional lipid aggregates are significantly important in bioactive delivery, for example, loaded vesicles have been widely used in delivery systems. The internal structures in cubosomes and hexosomes give them advantages over vesicles

with higher membrane surface area as the cargo can be shielded from the surrounding environment.

#### Loading Biologically-Derived Active Compounds

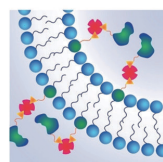
Post-formulation loading techniques

Charge-mediated:

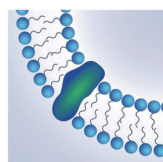


DNA and RNA charge interactions

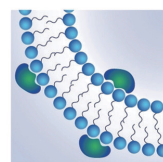
Protein-Loading Techniques:



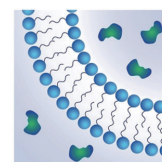
BT-Strep coupling to functionalized lipids



Integral membrane proteins



Peripheral membrane proteins



Hydrophilic proteins in aqueous channels

**Figure 1.13:** Key mechanisms for loading cubosome samples.<sup>69</sup>

A variety of molecules have been loaded in cubosomes, including proteins, DNA, antimicrobial peptides, and small molecule drugs.<sup>70–73</sup> The key mechanisms for loading are illustrated in Figure 1.13: cargo can be loaded within the lipid membrane, tethered to the lipid membrane, or localized within the water channels of the cubic phase according to the hydrophobicity and interaction with bilayers.<sup>69</sup>

The release kinetics of loaded molecules from liquid crystalline particles mainly depends on the molecular hydrophobicity. The exact mechanisms for release of hydrophobic molecules are still not understood well. Studies show that some poorly water-soluble drugs are released in a burst so that the majority of release occurs in a short time, while some drugs can be released in a controlled manner.<sup>74,75</sup> The release of hydrophilic molecules is assumed to be via diffusion and can be mediated by the size of loaded molecules and the water channel.<sup>76</sup>

The type of phase can also affect release. The hydrophilic drug release from nanostructured lipid systems has been studied and shows that the release follows first order diffusion kinetics, and bicontinuous cubosomes release 100% of the drug, while less than 5% release occurs from inverse micelles, hexosomes, and micellar cubic phase particles.<sup>22</sup> The big difference in release from different particles inspires design

of triggered release carriers. The change in external conditions like temperature and pH induces phase transition into bicontinuous cubosome, and as a consequence causes release.<sup>77</sup>

As liquid crystalline particles are formed under the driving force of non-covalent interactions, functional molecules can be added and incorporated with the lipids, making the particles possess more properties and functions. In cancer therapeutics, folic acid is added in monoolein cubosomes labeled for cancer cell targeting, resulting in an increased uptake and drug efficacy.<sup>78</sup>

### **1.3 Particle preparation with controlled shapes**

Complex shapes have been found in a wide range of substances, for example, some viruses have polyhedral protein shells for protecting the genetic molecules inside.<sup>79</sup> Particles with complex shapes have also been synthesized and applied in areas of acoustic metamaterials,<sup>80</sup> rheology control,<sup>81</sup> and drug delivery.<sup>81-83</sup> Shapes of inorganic nanocrystals can be controlled by regulating the growth rate of different facets, and changing the shape can profoundly alter the properties of material.<sup>31</sup> For soft particles, self-assembly of amphiphilic molecules into supermolecular aggregates is a common way of controlling shape.<sup>2,84</sup> Simulation can predict the assembly of simple shapes into complex structures, providing insight into the ordering of molecules, colloids, nanoparticles, proteins, and viruses.<sup>85</sup>

Besides the cubosomes and hexosomes with unique shapes discussed in Section 1.2.1, there are more works creating the non-spherical shapes based on droplet crystallization. Common liquid droplets are in the isotropic spherical shape which is limited by interfacial tension. When phase transition and crystallization occur inside a droplet, the internal elasticity increases and offsets the interfacial energy, breaking the original shape of droplet.<sup>87</sup> As shown in Figure 1.14, upon cooling, the

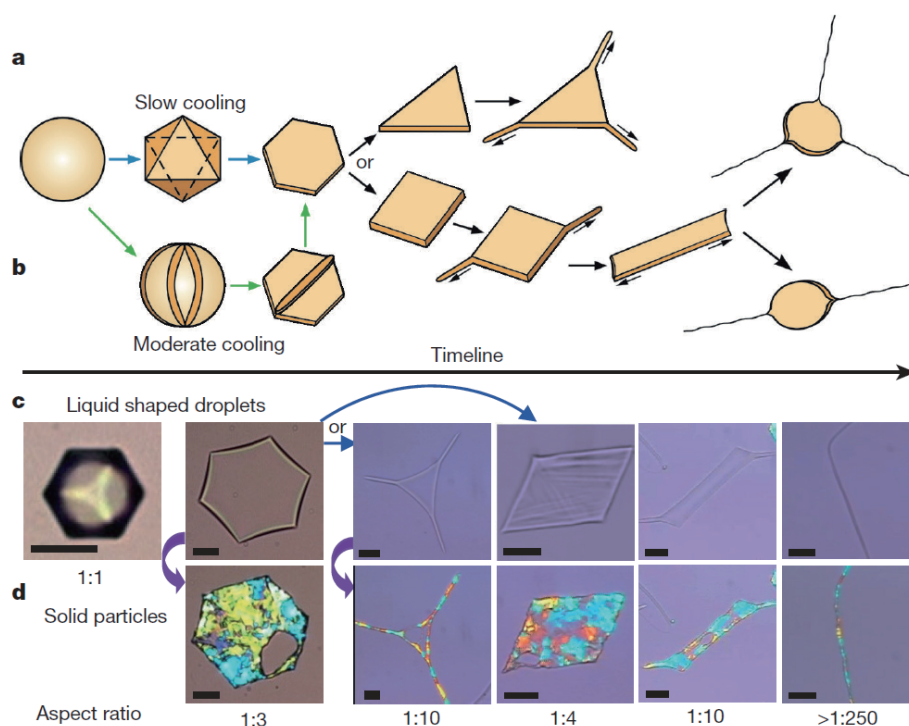


**Figure 1.14:** Schematic of the shape transformations observed during cooling of emulsion droplets of pure hydrocarbons in water.<sup>86</sup>

dispersed oil droplet spontaneously shifts into a series of geometric shapes.<sup>86</sup> The final shape of droplet can be controlled by composition, droplet size, and cooling rate. This self-shaping process is a simple but highly efficient bottom-up approach for making particles with complex shapes.<sup>88–90</sup>

## 1.4 Shape preservation from templates

Self-assembled aggregates can be used as templates to prepare various nanostructures. Ordered mesoporous silicas can be synthesized using surfactant solution as templates.<sup>91</sup> Figure 1.15 show a typical liquid-crystal templating approach. Inorganic precursors are a part of the template of liquid crystal, and the condensation of precursors occurs around surfactants, transforming the soft liquid crystal into a solid material. After reaction, the organic templates can be removed by calcina-

tion or extraction. The obtained inorganic materials preserve the microstructures, pore sizes, and symmetries from the liquid crystal templates. Materials with a large variety of microstructures have been synthesized, including hexagonal phase and bicontinuous cubic phase.<sup>92</sup>

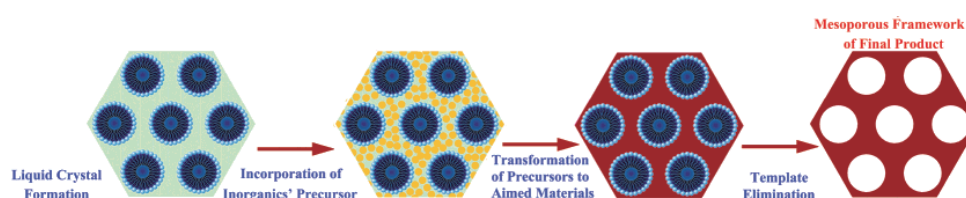


**Figure 1.15:** Synthetic strategies of mesoporous materials in a liquid-crystal templating process.<sup>91</sup>

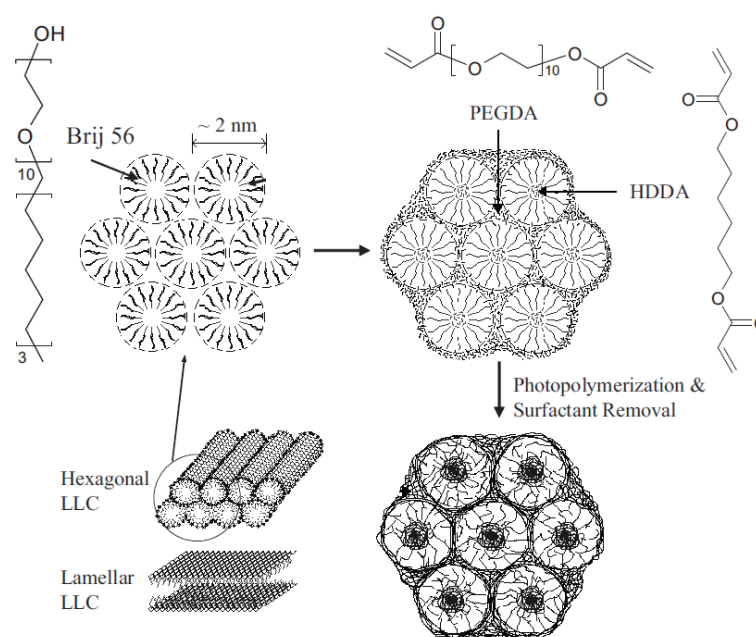


**Figure 1.16:** Schematic of the templating process with LLC mesophases.<sup>93</sup>

There are also numerous examples of polymeric materials formed in the templating approach, for example, capsules templated by spherical unilamellar vesicles,<sup>94,95</sup> and polymeric platelets made from anisotropic crystallized oil droplet templates.<sup>96</sup> Yang et al.<sup>97</sup> suggested cubosome nanoparticles could be polymerized, and cubic

and hexagonal liquid crystalline bulk phases have previously been used as templates for polymerization.<sup>93,98-100</sup> The templating process in molecular scale is shown in Figure 1.16, but no structures have been shown. Chapter 4 focuses on templating unique micron-scale geometric shapes from dispersed liquid crystalline phases, especially the recently developed novel polyhedra, which have not been observed in previous works.

### **1.5 Project aims and overview**

The literature review shows that the vast majority of cubosomes and hexosomes are nanoscale particles, but their small size makes observations difficult and limits the study of shape formation. Therefore liquid crystalline particles with larger length scales are needed, which can be observed directly using simple optical microscopy. The aim of this project is to produce microscale cubosomes and hexosomes, and link particle shapes with the bulk rheology and mesoscale structures. The better understanding of effects on soft particle shapes is helpful to design controlled processes and broaden applications for templated particle synthesis. The contents in each chapter are briefly summarized below.

In Chapter 2, microscale soft polyhedral particles of bicontinuous cubic phase are produced from a precursor emulsion by extracting solvent to grow facets on the droplets. Droplets containing water, ethanol, and the lipid glyceryl monoolein are suspended in a yield stress fluid, and transform into liquid crystals with solid-like rheology and controlled size and shape. SAXS confirms a bicontinuous cubic liquid crystalline phase forms from aqueous glycerol monoolein and is responsible for the particle faceting observed. Different polyhedra are produced by varying face growth rates through control of size, temperature, and addition of guest molecules. More exotic faceted shapes can be formed by applying asymmetric solvent removal

gradients and by deforming the precursor droplets into, for example, ellipsoids before crystallization. This method is a powerful means to produce soft polyhedra, using continuous microfluidic or other approaches, or to act as templates for hard polyhedral particle synthesis.

In Chapter 3, soft, rotationally symmetric particles of dispersed hexagonal liquid crystalline phase are produced using the method developed in Chapter 2. The technique forms hexosome particles via removal of ethanol from emulsion droplets containing monoolein, water, and hydrophobic molecules. The unique rotational symmetry of the particles is characterized by optical microscopy and SAXS to link particle phase, shape, and structure to composition. Rheology of the soft particles can be varied independently of shape, enabling control of transport, deformation, and biological response by controlling composition and molecular structure of the additives. The direct observations of formation, and the resultant hexosome shapes, link the particle-scale and mesoscale properties of these novel self-assembled particles and broaden their applications. The micron-scale hexosomes provide a route to understanding the effects of particle size, crystallization rate, and rheology on the production of soft particles with liquid crystalline structure and unique shape and symmetry.

Cubosomes and hexosomes produced in Chapters 2 and 3 are used as templates in Chapter 4 to polymerize various monomers to produce particles with unique micron-scale geometric shapes. The amphiphilicity of particles allows incorporation of various organic monomers. Photopolymerization of monomers in the lipid templates creates polymeric particles shaped like polyhedra based on cubic symmetry, as well as biconical cylinders based on hexagonal symmetry, and their shape is preserved after template removal. Particle shapes are controlled by varying the structures and hydrophobicity of the monomers. Monomer polarity determines whether

the template can exhibit hexagonal phase or cubic phase. Monomers also control the microstructure of the final particles produced, forming rigid shapes composed of linked polymer nanospheres when divinylbenzene or di(ethylene glycol) dimethacrylate is used, and soft hydrogel particles when N,N'-methylenebisacrylamide is used.

In the top-down method, production of nanoparticle hexosomes requires ultrasonication for complete dispersal due to the high elasticity of the materials. Although ultrasound is widely used to produce hexosomes, there are no direct studies of the process, the microscale flows occurring, and their effects on hexosome properties. In Chapter 5, we use high-speed microscopic imaging to directly observe bubble formation and degradation of bulk hexagonal phase, forming liquefied precursor materials that disperse and rapidly crystallize into hexosomes. Ultrasonic dispersal of the viscoelastic hexagonal phase is quantitatively related to the liquid crystal rheology, providing a process design basis as well as awareness of particle intermediate states that could affect short-time retention of solubilized active molecules.

Chapter 6 summarizes the work in this thesis and concludes key findings drawn from previous chapters, and provides some recommendations for future work.

## 1.6 References

- [1] J. Israelachvili, G. Adams, *II* **1976**, 72, 1525–1568.
- [2] C. Fong, T. Le, C. J. Drummond, *Chemical Society Reviews* **2012**, 41, 1297–1322.
- [3] Y. Huang, S. Gui, *RSC Advances* **2018**, 8, 6978–6987.
- [4] A. Yaghmur, O. Glatter, *Advances in colloid and interface science* **2009**, 147, 333–342.
- [5] S. Hyde, S. Andersson, K. Larsson, Z. Blum, T. Landh, S. Lidin, B. Ninham, *Chemistry and Biology. Elsevier Amsterdam* **1997**.
- [6] P. T. Spicer, K. L. Hayden, M. L. Lynch, A. Ofori-Boateng, J. L. Burns, *Langmuir* **2001**, 17, 5748–5756.



- 
- [7] D. Yang, B. Armitage, S. R. Marder, *Angewandte Chemie International Edition* **2004**, *43*, 4402–4409.
- [8] J. C. Shah, Y. Sadhale, D. M. Chilukuri, *Advanced drug delivery reviews* **2001**, *47*, 229–250.
- [9] P. T. Spicer, *Current Opinion in Colloid & Interface Science* **2005**, *10*, 274–279.
- [10] S. Radiman, C. Toprakcioglu, T. McLeish, *Langmuir* **1994**, *10*, 61–67.
- [11] T. Oka, N. Ohta, *Langmuir* **2016**, *32*, 7613–7620.
- [12] G. Shearman, O. Ces, R. Templer, J. Seddon, *Journal of Physics: Condensed Matter* **2006**, *18*, S1105.
- [13] F. Rosevear, *Journal of the American Oil Chemists' Society* **1954**, *31*, 628–639.
- [14] F. Livolant, Y. Bouligand, *Journal de Physique* **1986**, *47*, 1813–1827.
- [15] Y. Bouligand, *Journal de Physique* **1980**, *41*, 1297–1306.
- [16] J. M. Seddon, *Biochimica et Biophysica Acta (BBA)-Reviews on Biomembranes* **1990**, *1031*, 1–69.
- [17] M. Impéror-Clerc, P. Davidson, *The European Physical Journal B-Condensed Matter and Complex Systems* **1999**, *9*, 93–104.
- [18] P. Oswald, J.-C. Géminard, L. Lejcek, L. Sallen, *Journal de Physique II* **1996**, *6*, 281–303.
- [19] L. De Campo, A. Yagmur, L. Sagalowicz, M. E. Leser, H. Watzke, O. Glatter, *Langmuir* **2004**, *20*, 5254–5261.
- [20] A. Yagmur, L. De Campo, L. Sagalowicz, M. E. Leser, O. Glatter, *Langmuir* **2005**, *21*, 569–577.
- [21] Y.-D. Dong, I. Larson, T. Hanley, B. J. Boyd, *Langmuir* **2006**, *22*, 9512–9518.
- [22] S. Phan, W.-K. Fong, N. Kirby, T. Hanley, B. J. Boyd, *International journal of pharmaceuticals* **2011**, *421*, 176–182.
- [23] X. Gong, M. J. Moghaddam, S. M. Sagnella, C. E. Conn, S. J. Danon, L. J. Waddington, C. J. Drummond, *ACS applied materials & interfaces* **2011**, *3*, 1552–1561.
- [24] W.-K. Fong, T. L. Hanley, B. Thierry, A. Tilley, N. Kirby, L. J. Waddington, B. J. Boyd, *Physical Chemistry Chemical Physics* **2014**, *16*, 24936–24953.

## References

---

- [25] K. J. Tangso, H. Patel, S. Lindberg, P. G. Hartley, R. Knott, P. T. Spicer, B. J. Boyd, *ACS applied materials & interfaces* **2015**, 7, 24501–24509.
- [26] S. Salentinig, L. Sagalowicz, O. Glatter, *Langmuir* **2010**, 26, 11670–11679.
- [27] R. Mezzenga, C. Meyer, C. Servais, A. I. Romoscanu, L. Sagalowicz, R. C. Hayward, *Langmuir* **2005**, 21, 3322–3333.
- [28] S. Soni, G. Brotons, M. Bellour, T. Narayanan, A. Gibaud, *The Journal of Physical Chemistry B* **2006**, 110, 15157–15165.
- [29] V. Taillandier, PhD thesis, University of Leicester, **2014**.
- [30] J. Pal, T. Pal, *Nanoscale* **2015**, 7, 14159–14190.
- [31] Y. Xia, Y. Xiong, B. Lim, S. E. Skrabalak, *Angewandte Chemie International Edition* **2009**, 48, 60–103.
- [32] M. Caffrey, *Crystallizing membrane proteins for structure–function studies using lipidic mesophases*, **2011**.
- [33] J. Briggs, H. Chung, M. Caffrey, *Journal de Physique II* **1996**, 6, 723–751.
- [34] E. Lutton, *Journal of the American Oil Chemists Society* **1965**, 42, 1068–1070.
- [35] S. Hyde, S. Andersson, *Zeitschrift für Kristallographie-Crystalline Materials* **1984**, 168, 213–220.
- [36] M. Caffrey, F. Hing, *Biophysical journal* **1987**, 51, 37–46.
- [37] K. Larsson, *The Journal of Physical Chemistry* **1989**, 93, 7304–7314.
- [38] I. Martiel, L. Sagalowicz, S. Handschin, R. Mezzenga, *Langmuir* **2014**, 30, 14452–14459.
- [39] S. Rizwan, Y.-D. Dong, B. Boyd, T. Rades, S. Hook, *Micron* **2007**, 38, 478–485.
- [40] J. Gustafsson, H. Ljusberg-Wahren, M. Almgren, K. Larsson, *Langmuir* **1996**, 12, 4611–4613.
- [41] L. Sagalowicz, M. Michel, M. Adrian, P. Frossard, M. Rouvet, H. J. Watzke, A. Yagmur, L. De Campo, O. Glatter, M. E. Leser, *Journal of microscopy* **2006**, 221, 110–121.
- [42] J. Gustafsson, H. Ljusberg-Wahren, M. Almgren, K. Larsson, *Langmuir* **1997**, 13, 6964–6971.

- 
- [43] D. Demurtas, P. Guichard, I. Martiel, R. Mezzenga, C. Hébert, L. Sagalowicz, *Nature communications* **2015**, *6*, 8915.
- [44] L. Latypova, W. Gózdź, P. Pieranski, *The European Physical Journal E* **2013**, *36*, 88.
- [45] P. Pieranski, L. Sittler, P. Sotta, M. Imperor-Clerc, *The European Physical Journal E* **2001**, *5*, 317–328.
- [46] P. Pieranski, M. Bouchih, N. Ginestet, S. Popa-Nita, *The European Physical Journal E* **2003**, *12*, 239–254.
- [47] P. Pieranski, C. Even, D. Rohe, L. Sittler, M. Bouchih, N. Ginestet, S. Popa-Nita, T. Plötz-  
ing, J. Grenier, *Molecular Crystals and Liquid Crystals* **2005**, *434*, 235–563.
- [48] I. Amar-Yuli, E. Wachtel, E. B. Shoshan, D. Danino, A. Aserin, N. Garti, *Langmuir* **2007**, *23*, 3637–3645.
- [49] R. Mezzenga, P. Schurtenberger, A. Burbidge, M. Michel, *Nature materials* **2005**, *4*,  
729–740.
- [50] M. Johnsson, Y. Lam, J. Barauskas, F. Tiberg, *Langmuir* **2005**, *21*, 5159–5165.
- [51] L. Sagalowicz, S. Guillot, S. Acquistapace, B. Schmitt, M. Maurer, A. Yaghmur,  
L. De Campo, M. Rouvet, M. Leser, O. Glatter, *Langmuir* **2013**, *29*, 8222–8232.
- [52] B. J. Boyd, S. B. Rizwan, Y.-D. Dong, S. Hook, T. Rades, *Langmuir* **2007**, *23*, 12461–12464.
- [53] J. Jeong, Z. S. Davidson, P. J. Collings, T. C. Lubensky, A. Yodh, *Proceedings of the  
National Academy of Sciences* **2014**, *111*, 1742–1747.
- [54] C. Leal, N. F. Boussein, K. K. Ewert, C. R. Safinya, *Journal of the American Chemical  
Society* **2010**, *132*, 16841–16847.
- [55] A. Zabara, J. T. Y. Chong, I. Martiel, L. Stark, B. A. Cromer, C. Speziale, C. J. Drummond,  
R. Mezzenga, *Nature communications* **2018**, *9*, 544.
- [56] L. van't Hag, S. L. Gras, C. E. Conn, C. J. Drummond, *Chemical society reviews* **2017**, *46*,  
2705–2731.
- [57] M. Younus, R. N. Prentice, A. N. Clarkson, B. J. Boyd, S. B. Rizwan, *Langmuir* **2016**, *32*,  
8942–8950.

## References

---

- [58] L. S. Manni, S. Assenza, M. Duss, J. J. Vallooran, F. Juranyi, S. Jurt, O. Zerbe, E. M. Landau, R. Mezzenga, *Nature nanotechnology* **2019**, 1.
- [59] Z. Lin, S. Liu, W. Mao, H. Tian, N. Wang, N. Zhang, F. Tian, L. Han, X. Feng, Y. Mai, *Angewandte Chemie* **2017**, 129, 7241–7246.
- [60] Y. La, C. Park, T. J. Shin, S. H. Joo, S. Kang, K. T. Kim, *Nature chemistry* **2014**, 6, 534.
- [61] Y. La, T. H. An, T. J. Shin, C. Park, K. T. Kim, *Angewandte Chemie International Edition* **2015**, 54, 10483–10487.
- [62] T. H. An, Y. La, A. Cho, M. G. Jeong, T. J. Shin, C. Park, K. T. Kim, *ACS nano* **2015**, 9, 3084–3096.
- [63] P. Spicer, *Chemical Engineering Research and Design* **2005**, 83, 1283–1286.
- [64] P. T. Spicer, W. B. Small, M. L. Lynch, J. L. Burns, *Journal of Nanoparticle Research* **2002**, 4, 297–311.
- [65] W. K. Fong, S. Salentinig, C. A. Prestidge, R. Mezzenga, A. Hawley, B. J. Boyd, *Langmuir* **2014**, 30, 5373–5377.
- [66] L. Hong, S. Salentinig, A. Hawley, B. J. Boyd, *Langmuir* **2015**, 31, 6933–6941.
- [67] S. Salentinig, S. Phan, A. Hawley, B. J. Boyd, *Angewandte Chemie International Edition* **2015**, 54, 1600–1603.
- [68] A. J. Clulow, M. Salim, A. Hawley, B. J. Boyd, *Chemistry and physics of lipids* **2018**, 211, 107–116.
- [69] H. M. Barriga, M. N. Holme, M. M. Stevens, *Angewandte Chemie International Edition* **2019**, 58, 2958–2978.
- [70] E. Nazaruk, A. Majkowska-Pilip, R. Bilewicz, *ChemPlusChem* **2017**, 82, 570–575.
- [71] C. V. Kulkarni, V. K. Vishwapathi, A. Quarshie, Z. Moinuddin, J. Page, P. Kendrekar, S. S. Mashele, *Langmuir* **2017**, 33, 9907–9915.
- [72] T. G. Meikle, A. Zabara, L. J. Waddington, F. Separovic, C. J. Drummond, C. E. Conn, *Colloids and Surfaces B: Biointerfaces* **2017**, 152, 143–151.
- [73] L. Boge, A. Umerska, N. Matougui, H. Bysell, L. Ringstad, M. Davoudi, J. Eriksson, K. Edwards, M. Andersson, *International journal of pharmaceutics* **2017**, 526, 400–412.

- 
- [74] B. J. Boyd, *International journal of pharmaceutics* **2003**, *260*, 239–247.
- [75] T.-H. Nguyen, T. Hanley, C. J. Porter, I. Larson, B. J. Boyd, *Journal of pharmacy and pharmacology* **2010**, *62*, 844–855.
- [76] J. Clogston, M. Caffrey, *Journal of controlled release* **2005**, *107*, 97–111.
- [77] W.-K. Fong, T. Hanley, B. J. Boyd, *Journal of Controlled Release* **2009**, *135*, 218–226.
- [78] M. Nasr, M. K. Ghorab, A. Abdelazem, *Acta pharmaceutica sinica B* **2015**, *5*, 79–88.
- [79] W. Roos, R. Bruinsma, G. Wuite, *Nature physics* **2010**, *6*, 733.
- [80] S. A. Cummer, J. Christensen, A. Alù, *Nature Reviews Materials* **2016**, *1*, 16001.
- [81] J. R. Royer, G. L. Burton, D. L. Blair, S. D. Hudson, *Soft Matter* **2015**, *11*, 5656–5665.
- [82] E. Hinde, K. Thammairaphop, H. T. Duong, J. Yeow, B. Karagoz, C. Boyer, J. J. Gooding, K. Gaus, *Nature nanotechnology* **2017**, *12*, 81.
- [83] J. Park, J. E. Butler, *Macromolecules* **2010**, *43*, 2535–2543.
- [84] J. Guo, B. L. Tardy, A. J. Christofferson, Y. Dai, J. J. Richardson, W. Zhu, M. Hu, Y. Ju, J. Cui, R. R. Dagastine *et al.*, *Nature nanotechnology* **2016**, *11*, 1105.
- [85] P. F. Damasceno, M. Engel, S. C. Glotzer, *Science* **2012**, *337*, 453–457.
- [86] N. Denkov, S. Tcholakova, I. Lesov, D. Cholakova, S. K. Smoukov, *Nature* **2015**, *528*, 392.
- [87] P. A. Haas, R. E. Goldstein, S. K. Smoukov, D. Cholakova, N. Denkov, *Physical review letters* **2017**, *118*, 088001.
- [88] D. Cholakova, N. Denkov, S. Tcholakova, I. Lesov, S. K. Smoukov, *Advances in colloid and interface science* **2016**, *235*, 90–107.
- [89] N. Denkov, D. Cholakova, S. Tcholakova, S. K. Smoukov, *Langmuir* **2016**, *32*, 7985–7991.
- [90] S. Guttman, Z. Sapir, M. Schultz, A. V. Butenko, B. M. Ocko, M. Deutsch, E. Sloutskin, *Proceedings of the National Academy of Sciences* **2016**, *113*, 493–496.
- [91] Y. Wan, D. Zhao, *Chemical reviews* **2007**, *107*, 2821–2860.
- [92] C. Cui, L. Han, S. Che, *RSC Advances* **2019**, *9*, 6118–6124.
- [93] J. D. Clapper, C. A. Guymon, *Advanced Materials* **2006**, *18*, 1575–1580.
- [94] S. Dong, P. T. Spicer, F. P. Lucien, P. B. Zetterlund, *Soft matter* **2015**, *11*, 8613–8620.
- [95] J. D. Morgan, C. A. Johnson, E. W. Kaler, *Langmuir* **1997**, *13*, 6447–6451.

## References

---

- [96] I. Lesov, Z. Valkova, E. Vassileva, G. S. Georgiev, K. Ruseva, M. Simeonov, S. Tcholakova, N. D. Denkov, S. K. Smoukov, *Macromolecules* **2018**, *51*, 7456–7462.
- [97] D. Yang, D. F. O'Brien, S. R. Marder, *Journal of the American Chemical Society* **2002**, *124*, 13388–13389.
- [98] K. S. Worthington, C. Baguenard, B. S. Forney, C. A. Guymon, *Journal of Polymer Science Part B: Polymer Physics* **2017**, *55*, 471–489.
- [99] M. A. DePierro, C. A. Guymon, *Macromolecules* **2014**, *47*, 5728–5738.
- [100] D. L. Gin, W. Gu, B. A. Pindzola, W.-J. Zhou, *Accounts of chemical research* **2001**, *34*, 973–980.

## Chapter 2

# Soft polyhedral particles based on cubic liquid crystalline emulsion droplets

## 2.1 Introduction

Controlled formation of complex particle shapes has emerged as a powerful motivation for research in areas like acoustic metamaterials,<sup>1</sup> rheology control,<sup>2</sup> and drug delivery.<sup>3–8</sup> Just as biological cells vary widely in shapes depending on functions, synthetic particles can form a number of complex shapes via diverse methods.<sup>9</sup> Simple geometric shapes have been synthesized in a number of ways, but more complex shapes enable sophisticated hierarchical particle self-assembly. A crucial trait is particle faceting, as it tunes short-range interactions and directs dispersed particles to form preferred assemblies.<sup>10,11</sup> Simulations<sup>10</sup> can access any shape, as well as intermediates between shapes, but realisation of theoretical targets requires an experimental system as flexible as a simulation in its ability to produce and optimise complex particle shapes. For the ultimate flexibility, we need a system that can form many different shapes, retain different facet structures, and remain soft enough to allow more complex customisation than solids. An experimental toolkit of widely variable polyhedral particles is needed to achieve the ambitious vision set for faceted particle assemblies.<sup>10,12–15</sup>

---

This chapter originally published as Wang, H.; Zetterlund, P. B.; Boyer, C.; Boyd, B. J.; Prescott, S. W. & Spicer, P. T. “Soft polyhedral particles based on cubic liquid crystalline emulsion droplets” *Soft Matter*, **2017**, 13, 8492-8501

Excellent methods exist to synthesize solid particles with pre-designed shapes<sup>16,17</sup> or buckled forms,<sup>18</sup> but faceted particles can require crystallization<sup>13,19,20</sup> or specific molecular synthetic methods.<sup>21</sup> Softer materials like viscoelastic hydrogels have rheology that allows creation of faceted particles via molding<sup>22</sup> and buckling<sup>23</sup> but lose their fluid character in the process. Interfacial tension normally limits liquid droplet shapes to spheres, but is offset by interfacial<sup>24,25</sup> or internal elasticity<sup>26-28</sup> to form stable non-spherical shapes. Droplet faceting requires elasticity combined with an underlying structural order, as when interfacial crystallization on droplets<sup>29-31</sup> produces faceted solid capsules. A new approach is the use of liquid crystalline droplets, as they uniquely combine fluid-like rheology, crystalline faceting, and production simplicity.

Certain lyotropic liquid crystalline phases behave as a solid with an elastic modulus,  $G' \sim 10^5$  Pa<sup>32</sup> at stresses below their yield stress, while flowing like a viscous liquid above it.<sup>32,33</sup> Hexagonal and bicontinuous cubic phases form stable dispersed liquid crystalline nanoparticles, hexosomes and cubosomes, are useful as drug delivery vehicles<sup>34-38</sup> and form faceted shapes with length scales  $\sim 100$  nm,<sup>39-42</sup> though control of particle shape in these systems is not currently possible. Recent studies of complex facet formation in single large hemispherical droplets of smectic,<sup>43</sup> nematic,<sup>44</sup> and cubic lyotropic liquid crystalline phases<sup>45</sup> suggest an elegant way to produce beautifully complex faceted particles.<sup>46</sup> What is needed is a way to more flexibly control the shape of such particles, in three dimensions, via a robust, scalable process.

In this chapter we describe the production of soft, faceted, three-dimensionally symmetric particles using carefully tuned fluid rheology and adsorption to control particle size and shape. The method is designed to enable continuous flow produc-



tion of faceted particles in practical mixing systems, and is carried out using edible, safe materials and simple processes.

## 2.2 Materials and methods

Commercial grade monoolein, Dimodan MO90K, was obtained from DuPont Danisco (Botany, NSW, Australia). There are minor fractions of diglycerides, triglycerides and a monostearin glycol present, with free fatty acids present at a level of 0.5% (w/w).<sup>47</sup> The phase behavior of this system matches that of pure monoolein, in agreement with our earlier work<sup>40</sup> and consistent with more detailed studies.<sup>48</sup> The additives 99% ethanol and Pluronic F-127 were purchased from Sigma Aldrich (Castle Hill, NSW, Australia). Microfibrillated cellulose, MFC, was purchased from Wong Coco (Jakarta, Indonesia). Carbopol 846 was obtained from Lubrizol (Silverwater, NSW, Australia). All chemicals were used without further purification. Ultra-pure water with a resistivity of 18.25  $M\Omega$ -cm was obtained using a Sartorius Ultrapure water purifier.

Polyhedral particles were formed by combination of a precursor solution and a diluting solution, whose composition varies depending on the desired particle type. All precursor solutions contained 55 wt% monoolein, 25% ethanol, and 20% water, indicated by Point A in Figure 2.1. All experiments were conducted at 25 °C unless otherwise stated.

Initially, 0.02 – 0.2 mL of precursor was injected with a syringe into 3.5 mL of a diluting solution containing water, ethanol, and 0.1% w/w rheological modifier, MFC, that adds a yield stress to the fluid. A second yield stress fluid, aqueous Carbopol 846, was used as the continuous phase fluid when surface adsorption effects were needed. The ethanol concentration in the diluting solution was 25% v/v unless otherwise specified. Mixing the two solutions forms emulsion droplets that are

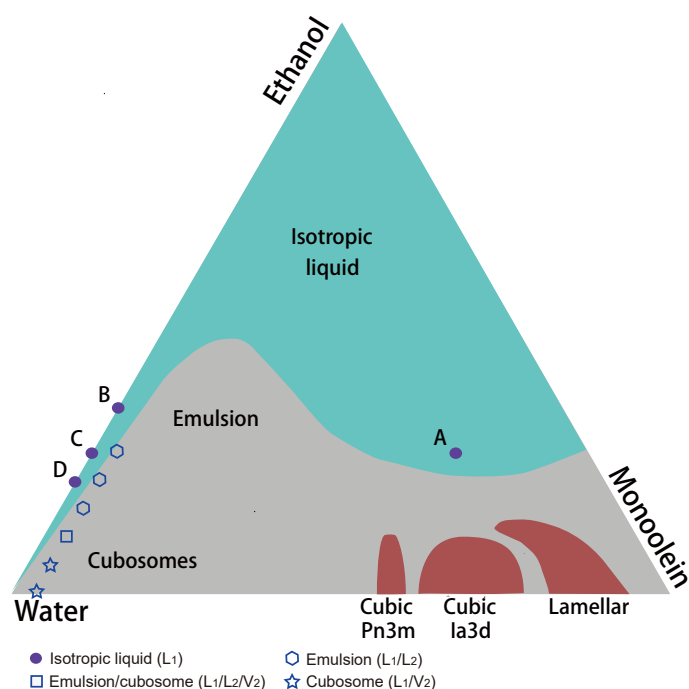


**Figure 2.1:** Pseudo-ternary phase diagram for the monoolein-ethanol-water system<sup>40</sup> used here to make polyhedra. Closed symbols indicate the compositions of the precursor solution, A, and a diluting solution with 33%, B, 25%, C, or 20%, D, ethanol. Open symbols show specific bulk results for multiple-phase regions relevant to the formation of particles.

then transformed into polyhedra by evaporation of ethanol from the suspension, as illustrated in Figure 2.2.

Some production of larger numbers of precursor droplets was performed using a simple millifluidic device made from coaxially aligned capillaries.<sup>49,50</sup> Precursor solution flows in the inner cylindrical capillary with an inner diameter of 100  $\mu\text{m}$ . Diluting solution flows in the outer cylindrical capillary with an inner diameter of 1.6 mm. Both liquids are injected using syringe pumps (WPI, 947-371-1003) using flow rates of 0.5  $\mu\text{L}/\text{min}$  and 1 mL/min for precursor and diluting solutions, respectively.

All particle formation experiments were carried out with samples in an open petri dish with a liquid height of 4 mm and a free surface area of 9.6  $\text{cm}^2$  to facilitate

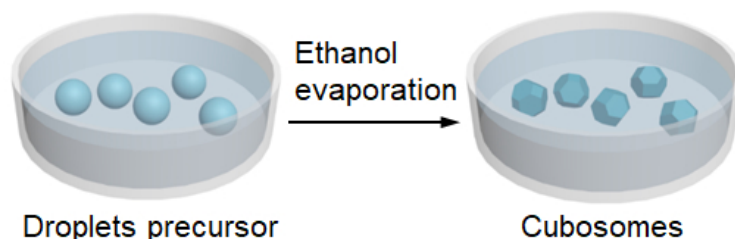


**Figure 2.2:** Schematic of formation of cubosomes from droplets precursor.

evaporation of ethanol and induce liquid crystal formation. The sample was held at constant  $T = 25^{\circ}\text{C}$  and Relative Humidity = 60% in a static environment during the transition process from droplets to particles. Adjusting the driving force of temperature or ethanol concentration, for example, can change the solvent evaporation rate, if desired. Measurements of mass loss with time were carried out using a Shimadzu TW423L balance in a controlled temperature and humidity environment. All time-dependent microscopic and SAXS measurements were performed by sampling from the petri dish containing the suspension. Once the desired shapes were formed, the suspending yield stress matrix was diluted for easy particle recovery.

Microscope observations were conducted on a Leica DM2500M optical microscope and all images were recorded using a Moticam 10MP digital camera. Micrographs shown here portray shapes representative of dispersions of more than 100 particles in a sample. Synchrotron small-angle X-ray scattering, SAXS, was used to identify the liquid crystalline structures responsible for larger-scale symmetry and faceting of all particles produced here. Samples were sealed into flat quartz cells mounted vertically on a remotely operated X-Y-Z translation stage at the Australian Synchrotron SAXS/WAXS beamline<sup>51</sup> and exposed to an X-ray beam with a wavelength of  $1.12\text{\AA}$ , energy 11 keV, with a sample-to-detector distance of 1034 mm. This setup provides a  $q$  range from  $0.018 < q < 1.02\text{\AA}^{-1}$ , where  $q$  is the magnitude of the scattering vector, defined as  $q = 4\pi/\lambda \sin(\theta/2)$ ,  $\lambda$  is the radiation wavelength,

and  $\theta$  the scattering angle. Two-dimensional spatial-resolved SAXS patterns were collected using 100  $\mu\text{m}$  steps on the translation stage, with 1 s acquisition at each position. A Pilatus 1M detector with an active area of  $169 \times 179 \text{ mm}^2$  and a pixel size of 172  $\mu\text{m}$  was used for acquisition. The two-dimensional SAXS patterns were then integrated into a one-dimensional scattering function  $I(q)$  using ScatterBrain Analysis software.<sup>52</sup> Cubic space groups were determined by the relative positions of the Bragg peaks in the scattering curves, which correspond to the reflections on planes defined by their Miller indices ( $hkl$ ). The ratio of  $\sqrt{2} : \sqrt{3} : \sqrt{4}$  corresponds to bicontinuous  $Pn3m$  phase, and the ratio of  $\sqrt{2} : \sqrt{4} : \sqrt{6}$  is the characteristic for  $Im3m$  phase.<sup>53</sup>

## 2.3 Results and discussion

### 2.3.1 Transition from droplets to cubosomes

The phase diagram in Figure 2.1 maps the pseudo-ternary monoolein-ethanol-water system used here. A large single phase region of isotropic liquid,  $L_1$ , is mapped in Figure 2.1 as a turquoise region, and is the basis for a precursor solution to form particles. The system contains three liquid crystalline phases, in red regions, two of which are inverse bicontinuous cubic phases,  $V_2$ , and one lamellar phase,  $L_\alpha$ .<sup>40</sup> Past work showed that nanoparticle cubosomes can be formed directly by homogeneous nucleation during dilution of the isotropic phase,  $L_1$ , into the water-rich region of the system,<sup>40</sup> marked “cubosomes” in Figure 2.1. The process is simple, and avoids the need for high-energy dispersion of viscous bulk cubic phase, but produces a broad particle size distribution spanning nanometers to microns.

Here we altered the bottom-up process to pass through an emulsion intermediate to better control particle size and carefully study facet formation. Instead of diluting

with water alone,<sup>40</sup> we diluted with a mixture of ethanol and water. The production of particles occurs in two stages: emulsion formation followed by evaporation of ethanol from the droplets to form liquid crystal particles. In the first stage, emulsion droplets of concentrated isotropic  $L_2$  phase form in a continuous phase of dilute  $L_1$  isotropic phase when the two precursor solutions are combined, in the area labeled “emulsion” in Figure 2.1. The two-phase region is located on the dilution trajectory connecting the precursor composition marked A and one of three diluting solutions marked B, C, and D. Formation of polyhedral particles then requires moving from the two-phase emulsion to the two-phase cubic  $Pn3m-L_1$  system by evaporative removal of ethanol. Phase equilibria require a change in the number of phases during such a transition, meaning the system passes through a three-phase intermediate state: the  $L_2-Pn3m-L_1$  system.<sup>46</sup> Relative locations of these states are shown in the phase diagram in Figure 2.1 using representative bulk measurements with known composition, including the final state of the samples once all ethanol is evaporated. The exact trajectory of the individual droplet compositions during evaporation is not known, and will vary with time throughout the suspension volume, but microscopic observations of the number of phases present at intermediate times are consistent with the bulk phase data in Figure 2.1. The transformation time scale is broadly adjustable from minutes to hours by varying the ethanol removal rate, enabling *in situ* study.

Figure 2.3a shows the change of a spherical droplet into a polyhedron over time, just as the droplet liquid phase has begun to form liquid crystalline facets. As ethanol diffuses out of the droplet and water diffuses in, surface facets stabilize and grow to form a symmetric, truncated octahedron. The liquid crystalline phase grows within the droplet,<sup>46</sup> increasing droplet elasticity and dominating the droplet’s interfacial tension to preserve a non-spherical faceted shape. The last image in Figure 2.3a indi-

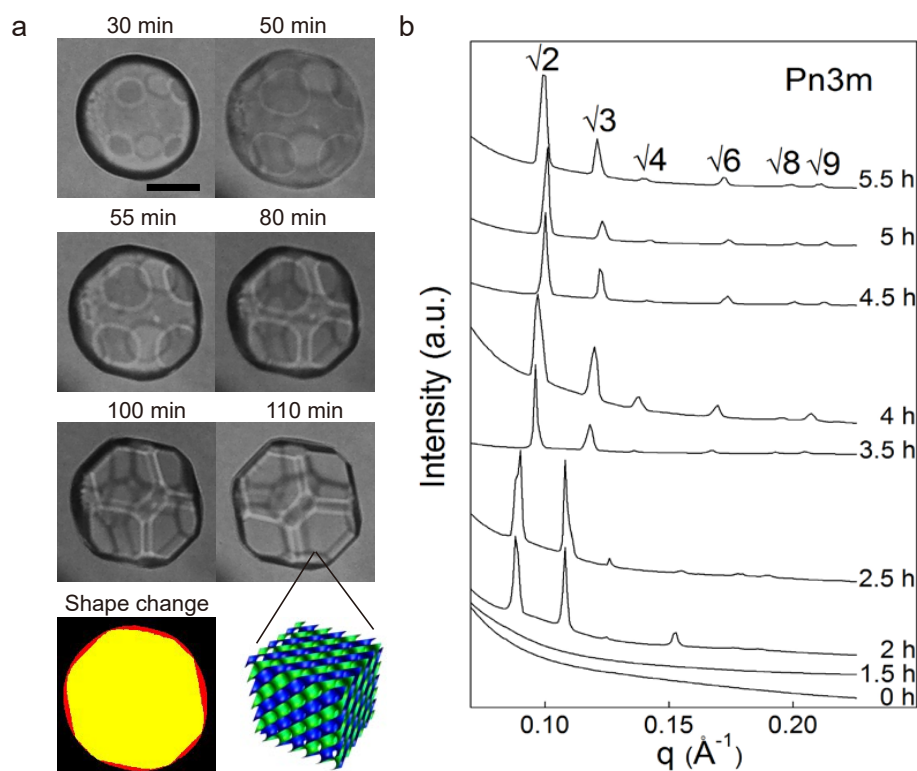


**Figure 2.3:** (a) Evolution of a precursor droplet into a faceted polyhedral particle as ethanol is removed. A rendering of the bicontinuous phase structure is shown as inset to the last particle micrograph. The composition of the precursor solution is 55% w/w monoolein, 25% ethanol, and 20% water. (b) Evolution of the molecular structure of identical droplets measured by SAXS. The drops transform into bicontinuous cubic liquid crystalline structures on a time scale similar to the droplet in (a), though slower because of mass transport limitations. In each experiment, the aqueous MFC continuous phase contains 25% v/v ethanol. Scale bar is 50  $\mu\text{m}$ .

cates that the final particle size, yellow area, reflects the initial droplet size, red area. Only a small amount of shrinkage occurs as the liquid crystal particle forms, enabling control of particle size in, for example, a microfluidic process. The micrographs in Figure 2.3a indicate the particles are three-dimensionally symmetric, as facets are visible on the far side of the transparent polyhedron. Formation in a low-viscosity continuous phase fluid with a yield stress,  $\sigma_y \sim 0.5 \text{ Pa}$ ,<sup>54</sup> immobilizes the particle, allowing three-dimensional growth, without altering its symmetry. The process is thus distinct from isotropic drop growth in a liquid crystalline phase<sup>55,56</sup> as well as

crystal growth in solid-like gels.<sup>57</sup> Suspension in the dilute yield stress fluid enables growth of faceted shapes without a need for a solid substrate<sup>43,58</sup> or close-packing of droplets.<sup>22</sup> Such a matrix is flexible enough to allow continuous production of droplets<sup>49</sup> while preserving the growing crystal symmetry. An additional benefit of the yield stress matrix is its immobilization of the droplet for further analytical interrogation with techniques such as SAXS.

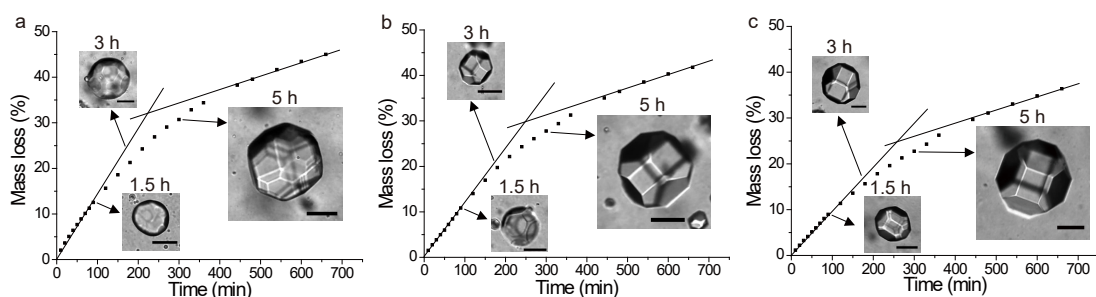


**Figure 2.4:** Relative mass loss as a function of time during the transition process from droplets to particles for diluting solutions with ethanol content of (a) 33 wt.%, (b) 25 wt.% and (c) 20 wt.%, corresponding to diluting solution compositions marked B, C, and D on Figure 2.1. Best-fit lines are drawn for the initial and final linear regions. Inset microscopy images show particles at various stages of crystallization. Scale bar is 50 μm.

Although we do not have a way of determining the composition of the individual droplets, we can document the rate at which mass is lost during the evaporation process. Such measurements establish the effect of the different evaporation driving forces used as well as allowing others to duplicate the process and tune the kinetics of the particle phase transition. We plot in Figure 2.4 measurements of the mass loss as a function of time during static evaporation of ethanol from the suspensions. Three stages are observed: an initial linear stage, a transitional stage, and a final linear stage, identical to similar studies of solvent evaporation from a pre-hexagonal phase emulsion.<sup>59</sup> The initial linear part of the curve corresponds to the evaporation of both ethanol and water, and the slope decreases with time as the ethanol is depleted. The final stage is also linear with a smaller slope, as evaporation of ethanol

has finished and only water evaporates at this stage. The intersection of the two linear regions provides an estimate of the characteristic time for completion of the particulate phase transition.<sup>59</sup> Three samples are plotted in Figure 2.4 for different ethanol levels in the diluting fluid that alter the evaporation rate and allow tuning of the kinetics of the transition. In Figure 2.4a, a diluting fluid with 33 wt.% ethanol has the highest volatility and the highest initial evaporation rate, obtained from a best-fit line to be 2.7 mg/min. The systems with lower ethanol levels have lower initial evaporation rates of 2.3 mg/min for a fluid containing 25 wt.% ethanol, Figure 2.4b, and 1.9 mg/min for a fluid with 20 wt.% ethanol, Figure 2.4c. Micrographs of representative particles are included as insets in Figure 2.4 to emphasize the stage of formation of faceted structures as evaporation proceeds. The three systems form particles with essentially the same shape, a truncated octahedron, although diluting with a 33 wt.% ethanol system causes a number of additional small facets to form because of the faster evaporation, and thus phase transition, rate. All other experiments used a diluting fluid containing 25 wt.% ethanol and evaporation occurred at the same rate as the sample in Figure 2.4b.

The reason for the formation of droplet facets in Figure 2.3a is the underlying mesophase structure's cubic liquid crystalline symmetry. We verify structural contributions to particle shape using SAXS data for a precursor emulsion slowly evolving into faceted particles via evaporative ethanol removal from the sample cell. Figure 2.3b shows the evolution of the dispersion's scattering peaks for the dispersion, indicating transformation into the highly ordered double-diamond bicontinuous cubic phase,  $V_2$ ,  $Pn3m$ . Structural classification is made based on the six peaks at  $q$  ratios of  $\sqrt{2}$ ,  $\sqrt{3}$ ,  $\sqrt{4}$ ,  $\sqrt{6}$ ,  $\sqrt{8}$ , and  $\sqrt{9}$ . The lattice parameter, calculated according to the  $q$  values, decreases significantly from 10.0 nm at 2 h to 8.9 nm at 4.5 h. The smaller size of the unit cells indicates a more condensed structure and is a key indicator



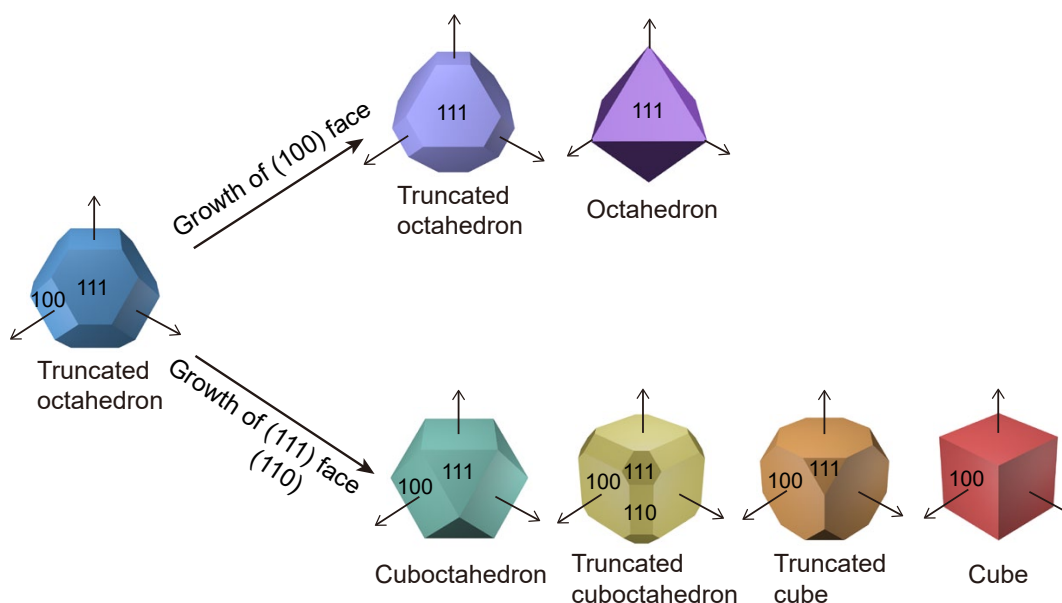


**Figure 2.5:** Different polyhedra shapes can be produced by control of selective face growth from a single cubic liquid crystalline  $Pn3m$  symmetry. (Polyhedra shapes are drawn with Autodesk 3ds Max)

of the growth-by-redistribution process.<sup>46</sup> Analogous to solid structures, the soft polyhedra exhibit shapes consistent with their underlying self-assembly, specifically the symmetry onto which the formed bilayer intrinsically folds to form the bicontinuous inverse cubic phase. Here, solid-like rheology preserves the shape-structure relationship of traditional solid crystal formation in a more flexible, tunable liquid crystalline matrix. The rate of polyhedron formation is set by the rate of phase transformation and can be controlled by adjusting the rate of solvent removal. Using the current setup, the transformation of droplets into cubosomes could occur at different rates in the same sample, due to variations in particle size and different evaporation rates of ethanol between the surface and inside liquid. The droplet in Figure 2.3a transformed faster than the majority of droplets, as it was located near the surface where ethanol evaporates faster. But for the SAXS pattern, the Bragg peaks appear when the facets are seen on most of droplets in the sample.

Control of shape is central to the development of faceted particles for a specific application, or to create a particular structure via self-assembly. The single, underlying symmetry of the cubic liquid crystals studied here can produce a wide range of polyhedral particles depending on the relative growth rates of different facets. For convenience, we refer to specific crystal faces using the Miller index,  $(hkl)$ , indicating three indices that are the inverse intercepts of a face's location with three-dimensional spatial axes.<sup>60</sup> Different facets have different associated energy states, partially dictating their stability and ease of formation. Figure 2.5 shows the pathway to produce at least six distinct shapes, depending on the kinetics of individual face growth, as regulated by experimental conditions. Starting from a truncated octahedron, the most energetically stable form of an fcc liquid crystal,<sup>19</sup> growth of the (100) face moves the shape increasingly toward a true octahedron, Figure 2.5 top path. The energy is the smallest for (111) facets and the largest for (110) facets in a cubic liquid crystal with  $Pn3m$  symmetry.<sup>41</sup> The highest energy facets tend to grow fastest in their perpendicular direction, often eliminating high-energy facets and maximizing surface area of low-energy facets, although liquid crystals can defy these expectations.<sup>45,61</sup> Similarly, growth of the (111) and then (110) faces moves the truncated octahedron through increasingly cubic shapes, to a cuboctahedron, a truncated cube, then a true cube, as we see in Figure 2.5's bottom path. Synthesizing each of these shapes as soft particles is then a matter of determining the conditions that drive formation of the desired form.

In order to demonstrate the flexibility of this method for forming soft polyhedra, the following results demonstrate control of particle shape using several experimental variables: precursor droplet size, solubilized and adsorbed additives, and anisotropic composition and deformation.

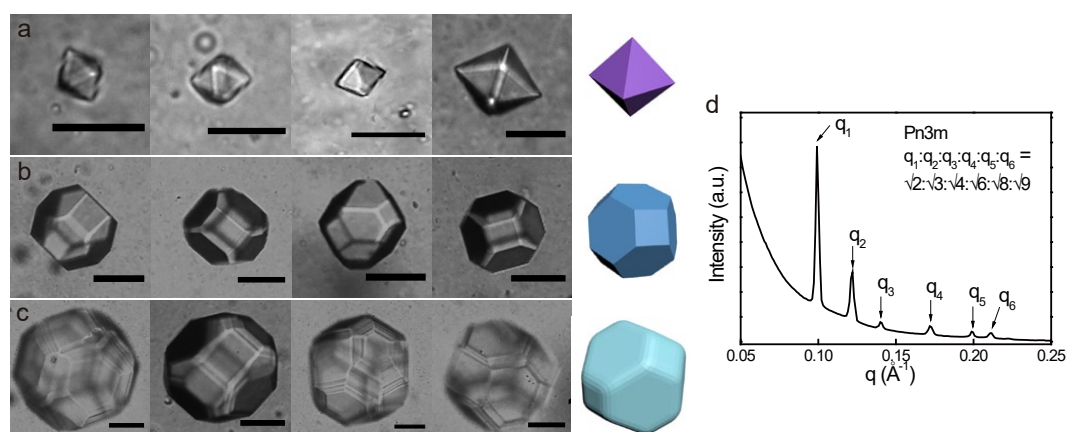


**Figure 2.6:** Particles with different shapes based on the size of the precursor emulsion droplet. Each row shows four different examples of: (a) octahedra, smaller than  $50\ \mu\text{m}$ , scale bar is  $50\ \mu\text{m}$ ; (b) truncated octahedra, smaller than  $100\ \mu\text{m}$ , scale bar is  $50\ \mu\text{m}$ ; (c) truncated octahedra with visible minor facets, larger than  $100\ \mu\text{m}$ , scale bar is  $30\ \mu\text{m}$ . (d) SAXS results indicate that all the shapes have the same cubic liquid crystalline structure, Pn3m symmetry. The composition of precursor droplets and the ethanol content of the diluting solution match the conditions in Figure 2.3.

### 2.3.2 Effects of precursor droplet size

A number of polyhedra are shown in Figure 2.6 that exhibit a distinct difference in shape, depending on precursor droplet size, in a single experiment. Octahedra form from precursor droplets smaller than  $50\ \mu\text{m}$ , as we see in Figure 2.6a. Truncated octahedra, Figure 2.6b, form from larger droplets in the size range  $50\ \mu\text{m} - 100\ \mu\text{m}$ . Even larger droplets,  $> 100\ \mu\text{m}$ , produce truncated octahedra as well, Figure 2.6c, but many more minor facets are visible. A similar stepped growth phenomenon at the surface of hemispherical droplets was reported by Pieranski and coworkers.<sup>45,58</sup> The highly elastic cubic phase is uniquely able to stabilize many major and minor facets because its surface energy-to-elasticity ratio is about five times the phase's lattice spacing.<sup>44</sup> As a result, elastic energy is spent to gain surface energy and the minor facets are more stable than in harder crystal systems. Unlike conventional solution

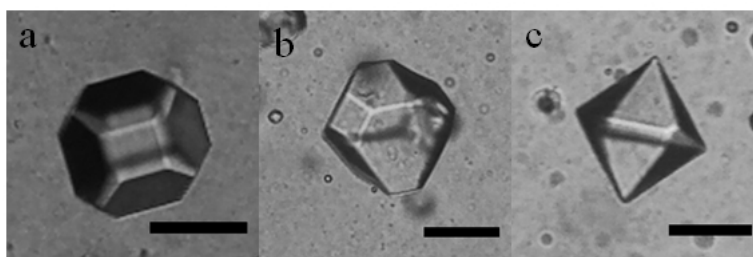


**Figure 2.7:** *Particles formed under different temperatures: (a) 25 °C; (b) 35 °C; (c) 45 °C. Precursor ingredients are in the same proportions as before. Scale bar is 50  $\mu\text{m}$ . The diluting solution contains 0.1% w/w MFC.*

crystallization, that obtains monocrystals from the bulk solution, these particles draw on just their internal liquid volume to form a liquid crystalline polyhedron: growth-by-redistribution.<sup>45,58</sup> The starting volume will then limit the extent of face growth: smaller droplets with higher curvature will require a smaller amount of growth for the (100) face to disappear completely and produce an octahedron. We see octahedra forming below a size of 50  $\mu\text{m}$  in Figure 2.6a. The shape of the particles is thus linked to precursor droplet size as a result of face growth kinetics, meaning processes like microfluidics can control the size and shape produced. Nanoparticles will have the fastest transport rates of solvent into or out of the particle, allowing growth of (111) face to completely dominate. As a result, we would expect nanodroplets in this system to transform into octahedra but we have not studied this length scale in detail.

Increasing temperature at a fixed size produces an analogous result to varying droplet size, as shown in Figure 2.7. Most particles formed at 25 °C are truncated octahedra. At 35 °C, the particles more closely resemble octahedra, with larger (111) and smaller (100) faces, while at 45 °C true octahedra form. Higher temperatures promote faster diffusion and increase face growth rates, more rapidly eliminating the high-energy (100) face.

Altering the ethanol concentration in the diluting solution, while keeping the precursor unchanged, also affects the final shape formed. For example, by increasing the level of ethanol, the shape of the resulting polyhedra is not changed significantly but the amount of small minor facets increases, reducing overall facet quality, as in Figure 2.6c. Starting from a higher ethanol level in the phase diagram coincides with a change in the slope of the relevant phase coexistence line in the phase diagram,<sup>46</sup> allowing more face growth to occur as the ethanol is removed. A volume ratio of 20% v/v ethanol turns precursor droplets into sharply-faceted truncated octahedra, consistent with the effect of larger starting droplets seen in Figure 2.6b. If the ethanol concentration in diluting liquid is too small, < 17% v/v, the system moves immediately from the emulsion region of Figure 2.1 to the cubosome region, producing only irregular chunks of cubic phase without shape control. Particles with polyhedral shapes form best when the diluting solution has an ethanol content > 17% v/v and < 33% v/v. Additional shapes can be produced using other methods to control the face growth dynamics.

### 2.3.3 Additive effects on surface and molecular packing

Cubic liquid crystalline molecular structure is altered<sup>62</sup> by added solutes,<sup>63,64</sup> salts,<sup>65</sup> changes in pH in the presence of ionizable additives<sup>66</sup> and temperature.<sup>67,68</sup> Molecules solubilized into the liquid crystal can impact the molecular packing of the phase, producing relatively minor changes in lattice spacing or more major phase transitions. Additives are often used, for example, to effect changes in solute release rates,<sup>69</sup> or to make very viscous phases easier to process.<sup>40</sup> We apply this concept here to broaden the range of polyhedral shapes of cubic liquid crystalline microparticles by changing the dominant faces in the underlying cubic symmetry. Pluronic F127 is an amphiphilic triblock co-polymer,  $PEO_{99} - PPO_{67} - PEO_{99}$ , that is known to insert

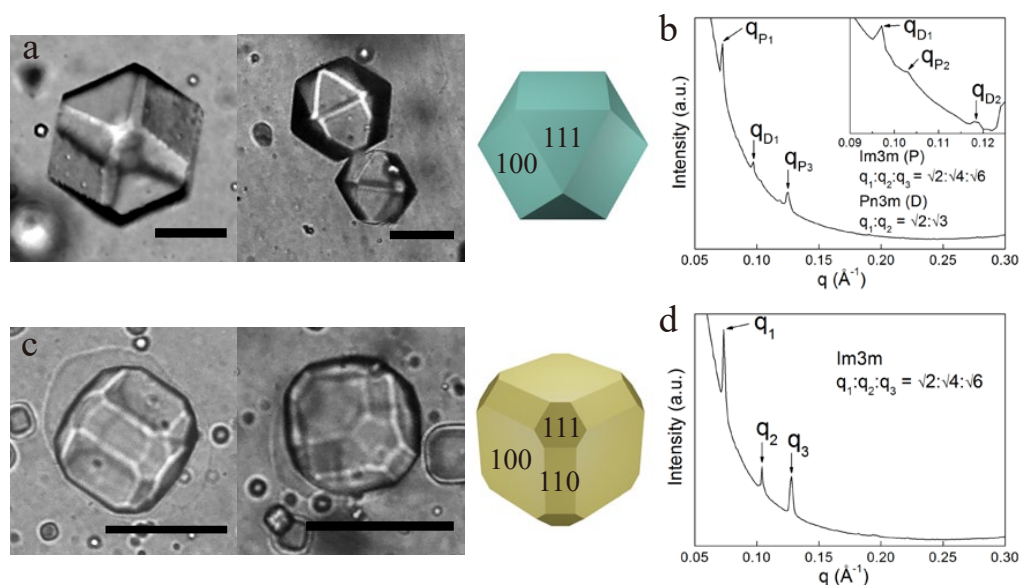


**Figure 2.8:** Microscope images, 3D model, and SAXS peaks for particles with added Pluronic F127 polymer. The F127 is present at 1% w/w in (a) and (b) and at 2% w/w in (c) and (d), while all other precursor ingredients are in the same proportions as before. Scale bar is 50  $\mu\text{m}$ . The diluting solution contains 0.1% w/w MFC.

into the monoolein bilayer and cause a molecular structural transition from  $Pn3m$  to  $Im3m$  symmetry in bulk cubic phases.<sup>41,63,70</sup>

We see such a transition here for our dispersed microparticles formed from precursor solution with small amounts of F127 added. The diluting solution in all cases contained water with 25% v/v ethanol and 0.1% w/w MFC. Figures 2.8a and c show polyhedra formed at 1% and 2% w/w F127 of the precursor solution while Figures 2.8b and d show the SAXS data for the corresponding dispersions. At 1% w/w F127, cuboctahedra form in contrast to the regular and truncated octahedral shapes in Figure 2.6 without added F127. The molecular structure reflects two-phase coexistence between  $Pn3m$  and  $Im3m$  cubic phases based on the indexed scattering visible for each phase, with the reflections attributable to the  $Im3m$  structure dominating those of the  $Pn3m$  phase in Figure 2.8b. The cubic lattice parameters  $a_P = 12.29$  nm,

$a_D = 9.14$  nm, and the calculated Bonnet ratio ( $a_P : a_D$ ) is approximately 1.34. The Bonnet ratio gives the predicted ratio of lattice parameters of two cubic phases with infinite periodic minimal surface under equilibrium conditions,<sup>71,72</sup> and the theoretical value is 1.279. The calculated and theoretical Bonnet ratios are close, but the difference is possibly because particles haven't reached equilibrium when measured.<sup>71,73</sup> When F127 was increased to 2% w/w in the precursor solution, the SAXS profile showed three peaks indicating  $Im\bar{3}m$  symmetry with a lattice parameter  $a_P = 12.17$  nm, demonstrating that the self-assembled structure had fully formed a single cubic phase at these F127 levels. When the  $Im\bar{3}m$  phase dominates, the particles are truncated cuboctahedra with added (110) faces besides the (100) and (111) faces formed in other shapes. Droplets on a substrate form an additional (211) face<sup>46</sup> but we did not observe such structures here. Interestingly, F127 is known to form and stabilize lamellar phase vesicles in similar systems<sup>40</sup> and the particles in Figure 2.8c show apparent vesicular membrane "halos" surrounding the largest particles. Vesicles are not seen in other samples, and do not seem to detract from the ability to form polyhedral shapes here. Solubilization of F127 into the liquid crystal clearly provides additional control over dominant face growth and final polyhedral shape by transformation of the cubic phase space group. This may be why cubes are mostly observed when nanoparticle cubosomes,  $\sim 50 - 200$  nm, are formed by fragmentation of bulk cubic phase in the presence of F127.<sup>40,74</sup> Given the surface nature of the initial facet formation, we might also expect effects by adsorbed additives.

Crosslinked polyacrylic acid particles are known to swell in water, when neutralized, to form microgels varying in size from 800 – 1200 nm. The microgels can interact with nonionic surfactants via adsorption or partitioning of some surfactants into the microgels.<sup>75</sup> Here we exploit this property by growing polyhedral particles in aqueous polyacrylate microgels, with or without MFC, in order to understand the

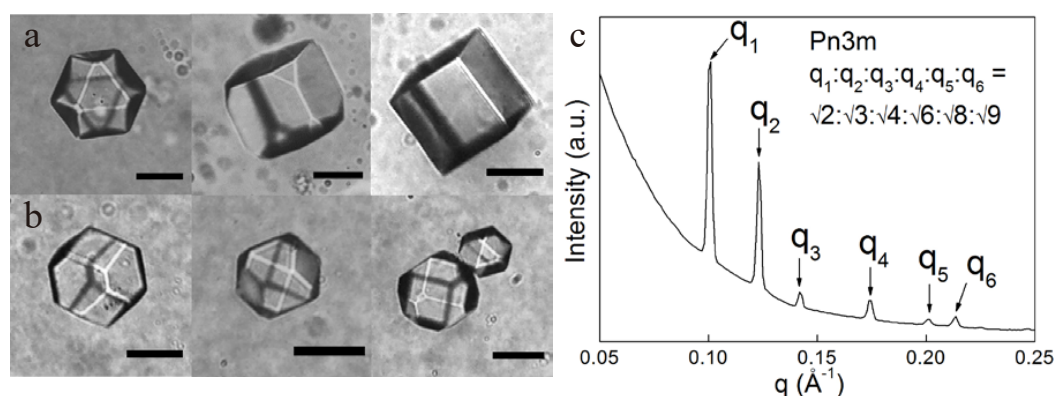


**Figure 2.9:** (a) Different shapes formed in aqueous 0.08% polyacrylate microgel suspensions and (b) 0.03% w/w aqueous microgels mixed with 0.05% MFC in the diluting solution. (c) SAXS result of particles formed in (a). Each row shows multiple examples. Scale bar is 50  $\mu\text{m}$ .

effects on particle shape. Figure 2.9a shows particles grown in 0.08% w/w microgels while Figure 2.9b shows particles formed in 0.03% w/w microgels mixed with 0.05% w/w MFC. The particles formed cuboctahedra, truncated cubes, and cubes in the same time scale as in Figure 2.3, distinct from the octahedra and truncated octahedra formed in MFC, Figure 2.6. Microgels likely adsorb at (100) faces, slowing their growth and causing (111) faces to disappear. In Figure 2.9c, the SAXS data for the particles in Figure 2.9a indicate that the phase of the liquid crystal is not changed. Appreciable solubilization of the polymer is therefore unlikely and the effects on polyhedron shape are more likely due to adsorption effects. Adding precursor solution to a mixture of microgels and MFC containing 25% v/v ethanol forms particles, Figure 2.9b, with a mixture of shapes like those in Figure 2.9a and Figure 2.6, indicating smaller effects of adsorption at lower microgel concentrations.

We see in Figures 2.6-2.9 that polyhedral shapes can be distinctly altered as they grow from spherical precursor droplets by favoring growth or disappearance of certain crystal faces. Such behavior is in good agreement with the overall pathways in Figure 2.5. The range of shapes produced from a simple system using common



techniques like size control, and small amounts of additives, is surprisingly broad. If the remarkable isotropic symmetry of the shapes in Figures 2.6-2.9 results from isotropic precursor shapes and environmental compositions, we hypothesize that more anisotropic initial conditions may provide additional degrees of shape control as the crystals grow. Polyhedral particles with broken symmetry could enable validation of theoretical structures predicted to form from Voronoi particles,<sup>15</sup> and provide more diverse building blocks of larger hierarchical structures.

### 2.3.4 Anisotropy in composition and deformation

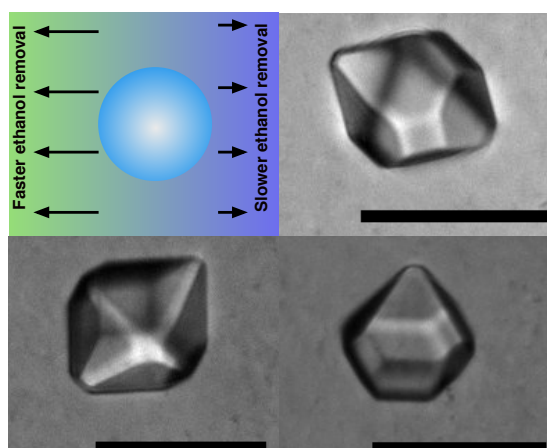


**Figure 2.10:** Polyhedral particles with shapes intermediate between more regular forms, formed using controlled, but anisotropic, growth rates. Scale bar is 50  $\mu\text{m}$ .

A simple means of varying the growth of crystals in precursor emulsion droplets is to arrange a gradient in driving force across the droplets. An example is at the air-liquid interface of an emulsion where removal rates are faster from the top than the bottom. Figure 2.10 shows several examples of anisotropic polyhedra formed with a shape that varies from one side to the other, in some cases octahedra morphing into what more resembles a truncated octahedron. Such shapes are not controlled or reproducible to any degree at this stage, but indicate the continuity of shape possible in this system even with non-uniform driving forces. An analogous effect was demon-

strated for cubic liquid crystals in another lyotropic system using a temperature gradient.<sup>76</sup>

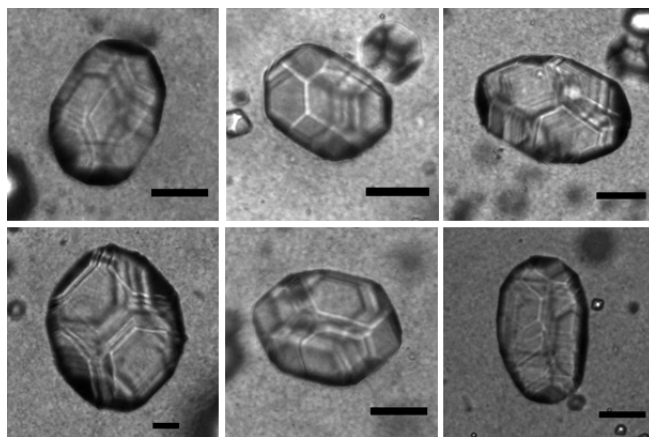


**Figure 2.11:** Particles grown from droplets elongated into ellipsoids by deformation of the diluting solution yield stress fluid. Scale bar is 50  $\mu\text{m}$ .

A second anisotropic constraint on final polyhedral shape is the starting shape of the precursor droplet. Precursor droplets can be deformed into ellipsoids by extensional deformation of the surrounding fluid if the continuous phase fluid has a yield stress on the order of  $\sigma_y \sim 10 - 50$  Pa and can offset interfacial forces<sup>77</sup> trying to return the droplets to a spherical shape. Such effects have been used to mold nematic droplets<sup>26</sup> and to arrest the relaxation of Pickering emulsion droplets.<sup>25</sup> When the ethanol is removed from the deformed droplets, we see growth of polyhedral shapes as in the spherical case, Figure 2.3, but now the symmetry of the facets is superimposed on the ellipsoidal form in the same time scale, Figure 2.11. Several modes of shape adaptation are seen for the polyhedra grown on ellipsoids. Facets are sometimes stretched along the ellipsoid long axis. Additional small minor facets are also common, as well as some blending of different shapes like the particles in Figure 2.10. It is fascinating to see the increased aspect ratios of the normally isotropic polyhedra in Figure 2.11. Initial deformation of the precursor droplet offers another

way to tailor the dimension and relative orientation of facets while retaining their apparent surface uniformity.

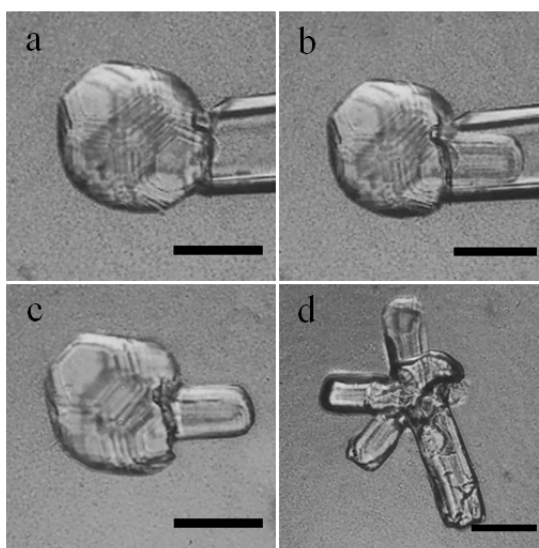


**Figure 2.12:** Polyhedral particle aspirated by a microcapillary to demonstrate the permanent deformation that occurs as a result of flow of the cubic phase at high stresses. Movie S2 shows the process. Scale bar is 50  $\mu\text{m}$ .

It is worth emphasizing that, though appearing quite solid in their faceted, polyhedral form, these particles are still liquid crystals with a moderate deformability. Figure 2.12 demonstrates this via a sequence of microscopy images showing a polyhedral particle, Figure 2.12a, being aspirated by a microcapillary. The particle deforms to the dimensions of the capillary, Figure 2.12b, but can be seen to retain some of the faceting that had already formed. Once released from the capillary, Figure 2.12c, the particle's significant yield stress ensures that it retains all of its original shape except where it was aspirated and molded into a cylindrical appendage. Further deformation can then be carried out as well, vastly reshaping and destroying the original symmetry of the polyhedron, Figure 2.12d. Although a crude example, Figure 2.12 demonstrates the potential for another type of shape constraint on the underlying molecular structure providing polyhedral symmetry and faceting. The

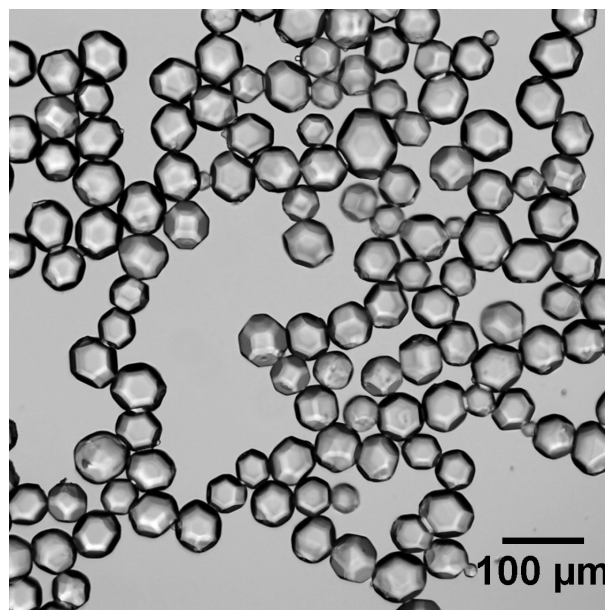


**Figure 2.13:** Micrograph of multiple soft truncated octahedral particles formed using this process.

enhanced flexibility of forming faceted particles via liquid crystalline growth adds new possibilities to the shapes normally achieved by solid crystal growth processes via an emulsion precursor.

Because the particles are easily produced from a readily prepared emulsion by simple evaporation, numerous polyhedra can be formed at once. Figure 2.13 shows an image of about 125 truncated octahedra whose size variability reflects that of their precursor emulsion. Preliminary production of such particles using millifluidic flow yields a size distribution with some variability as a result of the low interfacial tension between the two equilibrating liquid phases. Image analysis of the particles in Figure 2.13 gives a mean size of  $52.2\ \mu\text{m}$  with a standard deviation of  $9.6\ \mu\text{m}$ . We are still studying ways to produce truly monodisperse suspensions using this process, for example the enzymatic method using digestible triglycerides as a solute.<sup>42</sup>

## 2.4 Conclusions

We have demonstrated the flexible creation of soft polyhedral particles with a range of shapes based on variations of the cubic symmetry group and different modes of face growth within the groups. Precursor emulsion droplets of lipid and solvent are the basis for growth, via solvent removal, into faceted, highly elastic, soft three-dimensional shapes in a yield stress fluid. The rate of face growth can be varied using straightforward variables like droplet size, temperature, and solubilized and adsorbed additives, to control shape. Time scales of particle growth vary from minutes to hours depending on the driving force for mass transport. Arrest of the system in a desired shape is possible by halting solvent removal, and we are pursuing the templating and polymerization of these shapes to produce solid particles.

The polyhedra created here are unique in that they possess solid-like faceting and shape but also have a biologically-compatible liquid bicontinuous nanostructure that can encapsulate a wide range of solutes for delivery, reaction, and uptake functions. As a result, the particles can apply shape and structural properties over length scales from the molecular to the millimetric in one particle. The technique of soft polyhedra production has potential for new application areas like additive manufacturing and the creation of metamaterials, especially given the unique acoustic properties of the cubic phases.<sup>32</sup> The method may also provide a way to study other links between internal, molecular-scale structure and packing and the overall microscopic shape of particles. Far more complex faceting patterns could likely be produced on these particles by applying the insights of past single crystal phase mapping work,<sup>46</sup> as well as the anisotropic methods explored here. Microfluidic processes are currently being developed to produce these particles in a more continuous fashion so that their self-assembly behavior can be explored. We also plan to investigate the shape-

changing abilities of these particles, given their elasticity and responsiveness, as this is another promising approach to complex self-assembly.<sup>78</sup>

## 2.5 References

- [1] S. A. Cummer, J. Christensen, A. Alù, *Nat. Rev. Mater.* **2016**, *1*, 16001.
- [2] J. R. Royer, G. L. Burton, D. L. Blair, S. D. Hudson, *Soft Matter* **2015**, *11*, 5656–5665.
- [3] J. Champion, S. Mitragotri, *Proc. Nat. Acad. Sci.* **2006**, *103*, 4930.
- [4] P. Decuzzi, R. Pasqualini, W. Arap, M. Ferrari, *Pharm. Res.* **2009**, *26*, 235–243.
- [5] E. Gavze, M. Shapiro, *Int. J. Multiph. Flow* **1997**, *23*, 155–182.
- [6] J. Park, J. E. Butler, *Macromolecules* **2010**, *43*, 2535–2543.
- [7] B. R. Smith, P. Kempen, D. Bouley, A. Xu, Z. Liu, N. Melosh, H. Dai, R. Sinclair, S. S. Gambhir, *Nano Lett.* **2012**, *12*, 3369–3377.
- [8] R. Toy, P. M. Peiris, K. B. Ghaghada, E. Karathanasis, *Nanomed.* **2014**, *9*, 121–134.
- [9] S. Glotzer, M. J. Solomon, *Nat. Mat.* **2007**, *6*, 557–562.
- [10] P. F. Damasceno, M. Engel, S. C. Glotzer, *Science* **2012**, *337*, 453–457.
- [11] J. A. Millan, D. Ortiz, S. C. Glotzer, *Soft Matter* **2015**, *1*, 1386–1396.
- [12] G. van Anders, N. K. Ahmed, R. Smith, M. Engel, S. C. Glotzer, *ACS Nano* **2013**, *8*, 931–940.
- [13] K. L. Young, M. L. Personick, M. Engel, P. F. Damasceno, S. N. Barnaby, R. Bleher, T. Li, S. C. Glotzer, B. Lee, C. A. Mirkin, *Angew. Chem. Int. Ed.* **2013**, *52*, 13980–13984.
- [14] J. A. Millan, D. Ortiz, G. van Anders, S. C. Glotzer, *ACS Nano* **2014**, *8*, 2918–2928.
- [15] B. A. Schultz, P. F. Damasceno, M. Engel, S. C. Glotzer, *ACS Nano* **2015**, *9*, 2336–2344.
- [16] D. Dendukuri, S. Gu, D. Pregibon, T. Hatton, P. Doyle, *Lab Chip* **2007**, *7*, 818–828.
- [17] T. Merkel, K. Herlihy, J. Nunes, R. Orgel, J. Rolland, J. DeSimone, *Langmuir* **2009**, 557.
- [18] G. Vernizzi, M. O. de la Cruz, *Proc. Natl. Acad. Sci.* **2007**, *104*, 18382–18386.
- [19] Y. Xia, Y. Xiong, B. Lim, S. E. Skrabalak, *Ang. Chem. Int. Ed.* **2009**, *48*, 60–103.
- [20] M. L. Personick, C. A. Mirkin, *J. Am. Chem. Soc.* **2013**, *135*, 18238–18247.

- 
- [21] R. A. Brady, N. J. Brooks, P. Cicuta, L. Di Michele, *Nano Letters* **2017**, acs.nanolett.7b00980.
- [22] J. Fan, S.-H. Kim, Z. Chen, S. Zhou, E. Amstad, T. Lin, D. A. Weitz, *Small* **2017**, 1701256.
- [23] J. J. Crassous, A. M. Mihut, L. K. Månsson, P. Schurtenberger, *Nanoscale* **2015**, 7, 15971–15982.
- [24] A. Pawar, M. Caggioni, R. Ergun, R. Hartel, P. Spicer, *Soft Matter* **2011**, 7, 7710.
- [25] C. J. Burke, B. L. Mbang, Z. Wei, P. T. Spicer, T. J. Atherton, *Soft Matter* **2015**, 11, 5872–5882.
- [26] E. Pairam, A. Fernandez-Nieves, *Phys. Rev. Lett.* **2009**, 102, 234501–234501.
- [27] A. Pawar, M. Caggioni, R. Hartel, P. Spicer, *Faraday Disc.* **2012**, 158, 341–350.
- [28] E. Pairam, J. Vallamkondu, V. Koning, B. C. van Zuiden, P. W. Ellis, M. A. Bates, V. Vitelli, A. Fernandez-Nieves, *Proc Nat. Acad. Sci. USA* **2013**, 110, 9295–9300.
- [29] D. Lootens, C. Vautrin, T. Zemb, *Matls. Comm.* **2003**, 13, 2072–2074.
- [30] N. Denkov, S. Tcholakova, I. Lesov, D. Cholakova, *Nature* **2015**, 528, 392–396.
- [31] S. Guttman, Z. Sapir, M. Schultz, A. V. Butenko, B. M. Ocko, M. Deutsch, E. Sloutskin, *Proc. Nat. Acad. Sci. USA* **2016**, 113, 493–496.
- [32] J. L. Jones, T. C. B. McLeish, *Langmuir* **1995**, 11, 785–792.
- [33] S. Radiman, C. Toprakcioglu, T. McLeish, *Langmuir* **1994**, 10, 61–67.
- [34] C. Drummond, *Curr. Op. Colloid Int. Sci.* **2000**, 4, 449–456.
- [35] B. J. Boyd, D. V. Whittaker, S.-M. Khoo, G. Davey, *Int. J. Pharm.* **2006**, 309, 218–226.
- [36] B. Boyd, S.-M. Khoo, D. V. Whittaker, G. Davey, C. J. H. Porter, *Int. J. Pharm.* **2007**, 340, 52–60.
- [37] C. Fong, T. Le, C. J. Drummond, *Chem. Soc. Rev.* **2012**, 41, 1297–1322.
- [38] X. Mulet, B. J. Boyd, C. J. Drummond, *J. Colloid Int. Sci.* **2013**, 393, 1–20.
- [39] J. Gustafsson, H. Ljusberg-Wahren, M. Almgren, K. Larsson, *Langmuir* **1996**, 12, 4611–4613.
- [40] P. Spicer, K. Hayden, M. Lynch, A. Ofori-Boateng, J. Burns, *Langmuir* **2001**, 17, 5748–5756.

## References

---

- [41] M. Nakano, T. Teshigawara, A. Sugita, W. Leesajakul, A. Taniguchi, T. Kamo, H. Matsuoka, T. Handa, *Langmuir* **2002**, *18*, 9283–9288.
- [42] W. K. Fong, S. Salentinig, C. A. Prestidge, R. Mezzenga, A. Hawley, B. J. Boyd, *Langmuir* **2014**, *30*, 5373–5377.
- [43] J. Bechhoefer, L. Lejcek, P. Oswald, *J. de Phys. II* **1992**, *2*, 27–44.
- [44] P. Nozieres, F. Pistolesi, S. Balibar, *Eur. Phys. J. B* **2001**, *24*, 387–394.
- [45] P. Pieranski, P. Sotta, D. Rohe, M. Imperor-Clerc, *Phys. Rev. Lett.* **2000**, *84*, 2409–2412.
- [46] L. Latypova, W. Gózdź, P. Pieranski, *Eur. Phys. J. E* **2013**, *36*, 88–24.
- [47] P. T. Spicer, W. B. Small, M. L. Lynch, *J. Nanopart. Res.* **2002**, *4*, 297–311.
- [48] Y. D. Dong, A. J. Tilley, I. Larson, M. J. Lawrence, H. Amenitsch, M. Rappolt, T. Hanley, B. J. Boyd, *Langmuir* **2010**, *26*, 9000–9010.
- [49] R. Shah, H. Shum, A. Rowat, D. Lee, J. Agresti, A. Utada, L. Chu, J. Kim, A. Fernandez-Nieves, C. Martinez, D. Weitz, *Matls. Today* **2008**, *11*, 18–27.
- [50] C. Ohm, C. Serra, R. Zentel, *Adv. Mat.* **2009**, *21*, 4859–4862.
- [51] N. M. Kirby, S. T. Mudie, A. M. Hawley, D. J. Cookson, H. D. Mertens, N. Cowieson, V. Samardzic-Boban, *J. Appl. Cryst.* **2013**, *46*, 1670–1680.
- [52] S. Mudie, *Scatterbrain software*, [www.synchrotron.org.au](http://www.synchrotron.org.au), **2017**.
- [53] S. T. Hyde *et al.*, *Handbook of applied surface and colloid chemistry* **2001**, *2*, 299–332.
- [54] H. Emady, M. Caggioni, P. Spicer, *J. Rheo.* **2013**, *57*, 1761.
- [55] P. Sotta, *J. de Phys. II* **1991**, *1*, 763–772.
- [56] M. Lynch, K. Kochvar, J. Burns, R. Laughlin, *Langmuir* **2000**, *16*, 3537–3542.
- [57] M. Robert, F. Lefauchaux, *J. Crys. Growth* **1988**, *90*, 358–367.
- [58] P. Pieranski, L. Sittler, P. Sotta, M. Imperor-Clerc, *Eur. Phys. J. E* **2001**, *5*, 317–328.
- [59] I. Martiel, L. Sagalowicz, S. Handschin, R. Mezzenga, *Langmuir* **2014**, *30*, 14452–14459.
- [60] N. H. Hartshorne, A. Stuart, *Practical optical crystallography*, Elsevier, **1969**.
- [61] P. Pieranski, M. Bouchih, N. Ginestet, S. Popa-Nita, *Eur. Phys. J. E* **2003**, *12*, 239–254.
- [62] A. Yagmur, O. Glatter, *Adv. Colloid Int. Sci.* **2009**, *147-148*, 333–342.
- [63] Y.-D. Dong, I. Larson, T. Hanley, B. J. Boyd, *Langmuir* **2006**, *22*, 9512–9518.



- 
- [64] J. Zhai, L. Waddington, T. J. Wooster, M.-I. Aguilar, B. J. Boyd, *Langmuir* **2011**, *27*, 14757–14766.
- [65] Q. Liu, Y.-D. Dong, T. L. Hanley, B. J. Boyd, *Langmuir* **2013**, *29*, 14265–14273.
- [66] R. Negrini, R. Mezzenga, *Langmuir* **2011**, *27*, 5296–5303.
- [67] W.-K. Fong, T. Hanley, B. J. Boyd, *J. Controlled Rel.* **2009**, *135*, 218–226.
- [68] X. Mulet, X. Gong, L. J. Waddington, C. J. Drummond, *ACS Nano* **2009**, *3*, 2789–2797.
- [69] S. Phan, W.-K. Fong, N. Kirby, T. Hanley, B. J. Boyd, *Int. J. Pharm.* **2011**, *421*, 176–182.
- [70] T. Landh, *J. Phys. Chem* **1994**, *98*, 8453–8467.
- [71] C. Nilsson, B. Barrios-Lopez, A. Kallinen, P. Laurinmäki, S. J. Butcher, M. Raki, J. Weisell, K. Bergström, S. W. Larsen, J. Østergaard *et al.*, *Biomaterials* **2013**, *34*, 8491–8503.
- [72] C. E. Conn, C. Darmanin, X. Mulet, S. Le Cann, N. Kirby, C. J. Drummond, *Soft Matter* **2012**, *8*, 2310–2321.
- [73] S. T. Hyde, *Current Opinion in Solid State and Materials Science* **1996**, *1*, 653–662.
- [74] S. B. Rizwan, Y.-D. Dong, B. J. Boyd, T. Rades, S. Hook, *Micron* **2007**, *38*, 478–485.
- [75] R. Barreiro-Iglesias, C. Alvarez-Lorenzo, A. Concheiro, *J. Controlled Rel.* **2001**, *77*, 59–75.
- [76] P. Pieranski, *Liquid Crystals* **2009**, *36*, 1049–1069.
- [77] M. Caggioni, A. V. Bayles, J. Lenis, E. M. Furst, P. T. Spicer, *Soft Matter* **2014**, *10*, 7647–7652.
- [78] T. Nguyen, E. Jankowski, S. Glotzer, *ACS Nano* **2011**, *5*, 8892–8903.



## Chapter 3

# Large hexosomes from emulsion droplets: Particle shape and mesostructure control

### 3.1 Introduction

Molecular self-assembly by amphiphilic materials like block copolymers,<sup>1</sup> surfactants,<sup>2</sup> peptides,<sup>3,4</sup> and lipids is a broadly applicable technology that enables active delivery<sup>5</sup> as well as the creation of hierarchical structures<sup>6</sup> and advanced materials.<sup>7</sup> Liquid crystalline phases, for example, form spontaneously at moderate and high concentrations of amphiphiles in water and other polar solvents,<sup>8</sup> and their underlying crystalline symmetry and mesostructure creates a unique viscoelastic matrix<sup>9</sup> that can solubilize hydrophobic, hydrophilic, and amphiphilic molecules to significant levels.<sup>10</sup>

Although bulk liquid crystalline materials are of interest for many applications, some uses require the self-assembled structures be in a particulate form. Fortunately, a number of amphiphile-water systems that form liquid crystals also have a low water solubility. The resultant two-phase coexistence that occurs at high dilutions<sup>11</sup> enables formation of dispersed nanostructured particles of liquid crystal<sup>12</sup> that can be sterically stabilized for wide use.<sup>13,14</sup> Examples include dispersed lamellar

---

This chapter originally published as Wang, H.; Zetterlund, P. B.; Boyer, C.; Boyd, B. J.; Atherton, T. J. & Spicer, P. T. "Large Hexosomes from Emulsion Droplets: Particle Shape and Mesostructure Control" *Langmuir*, **2018**, 34, 13662-13671

phases, or liposomes,<sup>15</sup> fragmented bicontinuous cubic phases, or cubosomes,<sup>12</sup> and particles of hexagonal liquid crystalline phase, known as hexosomes.<sup>16</sup>

Nanostructured particles have biocompatible structures that are a key step in biological mechanisms like digestion and nutrient delivery,<sup>17</sup> holding much promise for controlled delivery of therapeutic molecules.<sup>18</sup> Recent work on nanomedicine delivery<sup>19</sup> and phagocytosis of particles<sup>20</sup> has highlighted the importance of nanoparticle and microparticle shape to the specificity and robustness of particle-based delivery methods. We seek to combine the benefits of particle shape with the enhanced performance of nanostructured materials, but the control of particle shape in liquid crystalline systems has not been studied in great detail. One reason for the lack of activity is the difficulty in direct observation of liquid crystalline nanoparticles, as the observation of these objects requires cryo-transmission electron microscopy, Cryo-TEM, studies that require expensive infrastructure and are inherently limited in the number of particles that can be studied. One solution is to increase the length scale of liquid crystalline particles, allowing study via simple optical microscopy methods and greatly increasing the versatility for observation.<sup>21</sup>

In Chapter 2 we showed the ability of micron-scale cubosomes to form a wide range of faceted soft particles, depending on crystallization rate and the properties of solvent and additives<sup>21</sup>. The ability to form such particles, using a simple emulsion precursor process,<sup>22</sup> holds promise for controlled production of liquid crystalline particles with complex shapes, for example via microfluidics. The same approach should be feasible to study hexosome particles, provided the phase transition from cubic to hexagonal liquid crystalline phase can be incorporated into such a process. Hexosomes and hexagonal phase have been shown to be superior to bicontinuous cubic phase at inhibiting release of solubilized drugs,<sup>23</sup> and their inherent rotational symmetry offers a unique approach to form particle and colloid shapes with advan-

tages in surface deposition and active matter.<sup>24</sup> Increased study and ease of use will be instrumental in expanding such applications.

Phase transition from cubic to hexagonal phase can be triggered by increasing temperature,<sup>2,25–27</sup> adding hydrophobic molecules,<sup>28–30</sup> and changing pH.<sup>31,32</sup> These conditions increase the effective volume of the hydrocarbon of the amphiphile, increasing the critical packing parameter, and transforming the contorted bicontinuous amphiphile bilayers to hexagonally packed cylinders,<sup>25</sup> as shown in the schematic in Figure 3.1a. As a result, hexosomes can be made using the same mechanism that causes such phase transitions in bulk liquid crystals.

Hexosomes made in previous work were all nanoparticles,<sup>28,33–35</sup> requiring specialized microscopy techniques for direct observation. Two-dimensional cryo-TEM<sup>36</sup> and AFM<sup>37</sup> images suggest that hexosomes mainly form as either flat disk-like hexagonal prisms (Figure 3.1b), or spherical shapes, but three-dimensional characterization is limited with such techniques.<sup>38</sup> Cryo-SEM imaging<sup>39</sup> showed that some hexosomes can adopt a shape resembling a spinning top, a short cylinder capped at both ends by a cone, as shown in Figure 3.1c. Related biconical shapes with a central raised spine structure were also noted,<sup>39</sup> and are shown as a schematic in Figure 3.1d, but multiple mesostructures have been proposed to explain the different shapes of particles with an underlying hexagonal symmetry.

Amphiphilic lipid hexosomes forming flat prisms were thought to form from hexagonally packed cylindrical micelles aligned perpendicular to the largest face.<sup>36</sup> Monoolein spinning top shapes were explained as cylinders aligned along their long axis,<sup>39</sup> similar to the proposed structure of unit cells in biconical single crystals of precipitated silicate.<sup>40</sup> Chromonic liquid crystal particles can also exhibit biconical shapes, despite having different rheology and building blocks from hexosomes, but were proposed to result from hexagonal columns curled around the central symme-

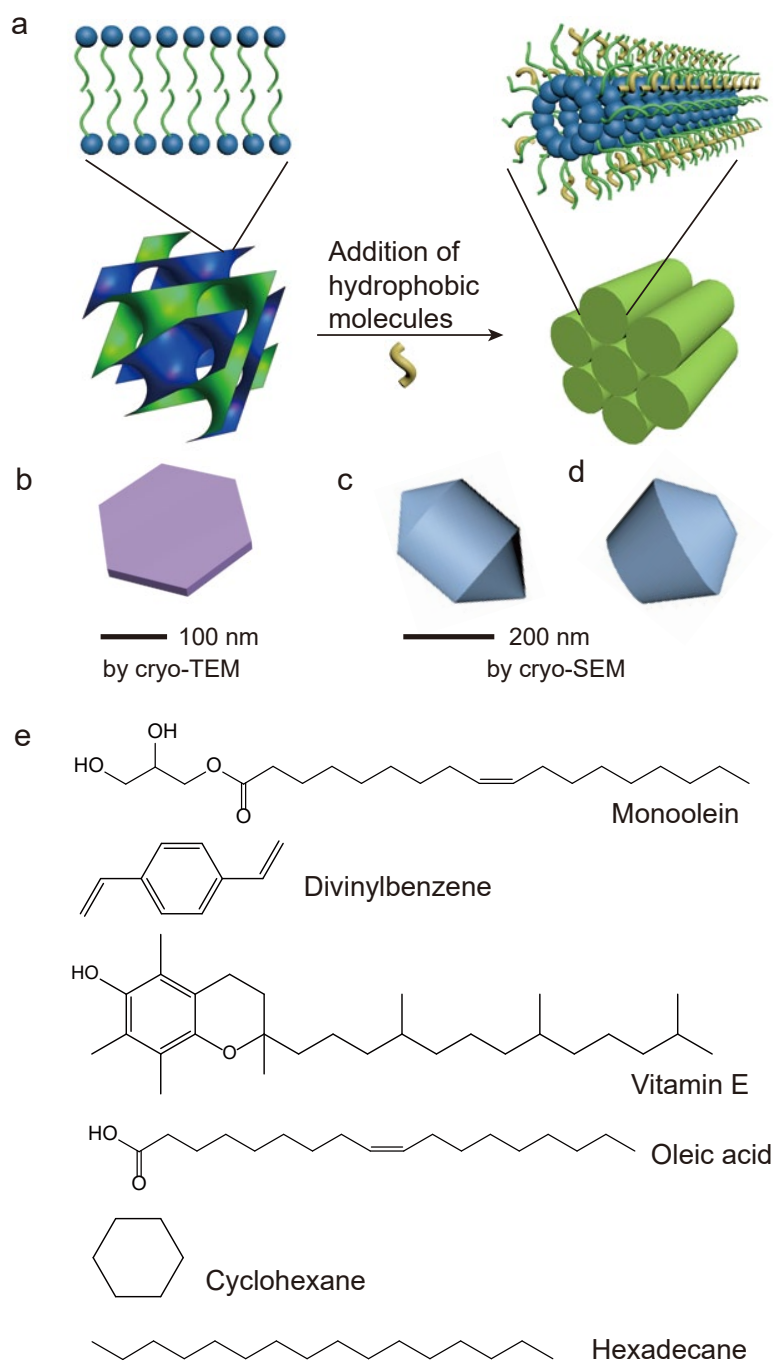


**Figure 3.1:** (a) Schematic of change in microstructure during transition from cubic to hexagonal phase; (b) Hexosome shape and length scale observed by cryo-TEM;<sup>36</sup> (c) Spinning top and (d) Biconical shapes observed by cryo-SEM;<sup>39</sup> (e) Molecular structure of the amphiphile and additive chemicals used in the formation of hexosomes.

try axis.<sup>41</sup> Similar structures were directly observed in biconical block copolymer particles, with SEM images showing hexagonally packed cylinders wrapped around the central symmetry axis.<sup>42</sup> Bulk hexagonal phase insights also help explain the ordering in hexosome particles. The radial confinement length scale,  $r$ , of hexagonal phase structures in cylindrical capillaries was recently found to affect the transition between cylindrical micelles aligned with the mesostructure long axis, for  $r > 0.2$  mm, and cylindrical micelles bent around the long axis, for  $r < 0.2$  mm.<sup>43</sup>

We are interested in more closely studying hexosome production above micron length scales to better understand how to control their shape and broaden applications. Larger hexosomes may also improve reservoir and controlled release properties, as the liquid crystalline phase diffusivity is too high for good performance of particles with nanoscale dimensions.<sup>44</sup> One promising route to using hexosomes as delivery vehicles is via enzymatic degradation of precursor emulsion droplets,<sup>26,45</sup> so developing improved physical models of shape control will enable improvement and optimization of such applications.

In this chapter emulsion droplet precursors, containing ethanol and monoolein are created, with varying amounts of either vitamin E, hexadecane, oleic acid, cyclohexane, or divinylbenzene (DVB) guest molecules<sup>46</sup> and dispersed into an aqueous continuous phase. The droplets transform into hexosomes following removal of ethanol,<sup>21</sup> as confirmed by small-angle X-ray scattering (SAXS). The micron-scale hexosome particles tend to have underlying hexagonal symmetry,<sup>39</sup> though can exhibit significant variations in overall shape and proportions. Optical study indicates particle mesostructures are the cause of the shape variations and can be controlled by, for example, emulsion droplet size and levels of hydrophobic additives. The direct observations of formation, and the resultant hexosome shapes, link the particle-scale and mesoscale properties of these novel self-assembled particles. Given the potential

for soft particles to enable unique control of self-assembly and biological interactions, we are particularly motivated to understand the mechanisms by which the shapes and mechanical properties<sup>47-49</sup> of such particles can be controlled in simple, scalable flow<sup>21</sup> and mixing processes<sup>22</sup>.

## 3.2 Materials and Methods

Commercial grade monoolein, Dimodan MO90K, was obtained from DuPont Danisco (Botany NSW, Australia). Ethanol (99%) and cyclohexane (99%) were purchased from Chem-Supply (Australia). Vitamin E ( $\alpha$ -tocopherol, 96%), divinylbenzene (80%), hexadecane (99%) and oleic acid (90%, in the acid form at the pH of all hexosome samples) were purchased from Sigma Aldrich (Castle Hill, NSW, Australia). Commercial vitamin E (Blackmores, Australia) was also used and contains structural isomers, unsaturated tocotrienols, and  $\alpha$ -tocopherol.<sup>50</sup> Microfibrillated cellulose, MFC, was purchased from Wong Coco (Jakarta, Indonesia). All chemicals were used without further purification. Ultrapure water with a resistivity of 18.25  $M\Omega$ -cm was obtained using a Sartorius ultrapure water purifier.

Hexosomes were formed by combination of a precursor solution and a diluting solution. All precursor solutions contained monoolein and ethanol with a weight ratio 1:1, and a desired amount of additives. The amount of additive is reported as a mass ratio of additive to monoolein. All experiments were carried out at 25 °C.

Initially, 0.02 – 0.2 mL of precursor was injected with a syringe into 3.5 mL of a diluting solution containing water, ethanol, and 0.1% w/w rheological modifier, MFC, that adds a yield stress to the fluid and allows three-dimensionally symmetric particle formation from droplets. The MFC is used only to immobilize the droplets and resultant particles, preventing coalescence and aggregation and enhancing microscopy accuracy. The cellulose fibers are much larger size than the hexosome mesostructure,



with fibers typically 5 – 10  $\mu\text{m}$  in length. As the pure cellulose material is insoluble in water, we see no effect on the phase behaviour during control experiments, in agreement with our previous work that found no structural changes caused by MFC during cubosome formation.<sup>21</sup> The ethanol concentration in the diluting solution was 25% v/v. Mixing the two solutions forms emulsion droplets that are then transformed into hexosomes by evaporation of ethanol from the suspension with an ethanol evaporation rate of 2.3 mg/min. These concentrations provided both the necessary driving force magnitude and a sufficiently slow rate to produce well-formed particles, as we found in our previous work on cubosome formation.<sup>21</sup>

All particle formation experiments were carried out with samples in an open petri dish with a liquid height of 4 mm and a free surface area of 9.6 cm<sup>2</sup> to facilitate evaporation of ethanol and induce liquid crystal formation. The sample was held at constant  $T = 25^\circ\text{C}$  and Relative Humidity = 60% in a static environment during the transition process from droplets to particles. Time-dependent microscopic observations were performed by sampling from the petri dish containing the suspension. Once the desired shapes were formed, the suspending yield stress matrix was diluted to allow easy particle recovery.

Microscope observations were conducted on a Leica DM2500M optical microscope with a Leica N PLAN 10X EPI objective lens 10/0.25, and all images were recorded using a Moticam 10MP digital camera. Micrographs shown here portray shapes representative of dispersions of more than 100 particles in a sample and all image analysis of shape was performed using ImageJ.<sup>51</sup> Polarizing microscopy texture analysis is a primary tool for studying liquid crystalline phases that are optically anisotropic and birefringent. The liquid crystals can split an incoming light beam into two components, one of which can pass through an analyzer that is crossed relative to the polarizer, making the sample appear bright. Transmitted light intensity

changes with sample orientation relative to the polarizer, and the colorful patterns indicate interference of the split light.<sup>52</sup> In hexagonal phase, specific birefringence textures indicate certain molecular packing and defects of microstructure.<sup>53,54</sup>

Synchrotron small-angle X-ray scattering, SAXS, was used to identify the liquid crystalline structures responsible for larger-scale symmetry and faceting of all particles produced here. Samples were sealed into flat quartz cells mounted vertically on a remotely operated X-Y-Z translation stage at a temperature of about 25 °C at the Australian Synchrotron SAXS/WAXS beamline<sup>55</sup> and exposed to an X-ray beam with a wavelength of 1.12 Å, energy 11 keV, with a sample-to-detector distance of 1034 mm. The setup provides a  $q$  range from  $0.018 < q < 1.02 \text{ \AA}^{-1}$ , where  $q$  is the magnitude of the scattering vector, defined as  $q = 4\pi/\lambda \sin(\theta/2)$ ,  $\lambda$  is the radiation wavelength, and  $\theta$  the scattering angle. Two-dimensional spatially-resolved SAXS patterns were collected using 100  $\mu\text{m}$  steps on the translation stage, with a 1 s acquisition at each position. A Pilatus 1M detector with an active area of  $169 \times 179 \text{ mm}^2$ , and a pixel size of 172  $\mu\text{m}$ , was used for acquisition. The two-dimensional SAXS patterns were then integrated into a one-dimensional scattering function  $I(q)$  using ScatterBrain Analysis software.<sup>56</sup> The phase type is identified by correlating  $q$  values of the peaks with Miller indices ( $hkl$ ) for known liquid crystalline phases, and the ratio  $\sqrt{1} : \sqrt{3} : \sqrt{4}$  corresponds to hexagonal phase ( $p6mm$ ). Lattice parameters,  $a$ , the repeat distance of the microstructure, are calculated using the equation  $a = 4\pi\sqrt{h^2 + k^2 + hk}/\sqrt{3}q_{hk}$ .<sup>57</sup>

Rheological characterization of bulk liquid crystalline phases was performed using a DHR-1 rheometer from TA Instruments using an oscillatory stress sweep at a constant frequency of 1 Hz. A cone and plate geometry was used for all measurements and a solvent trap was used to avoid evaporative losses. Elastic modulus

is measured as the plateau value attained at low stresses in the linear viscoelastic regime.

### 3.3 Results and discussion

#### 3.3.1 Formation of microscale hexosomes from droplets

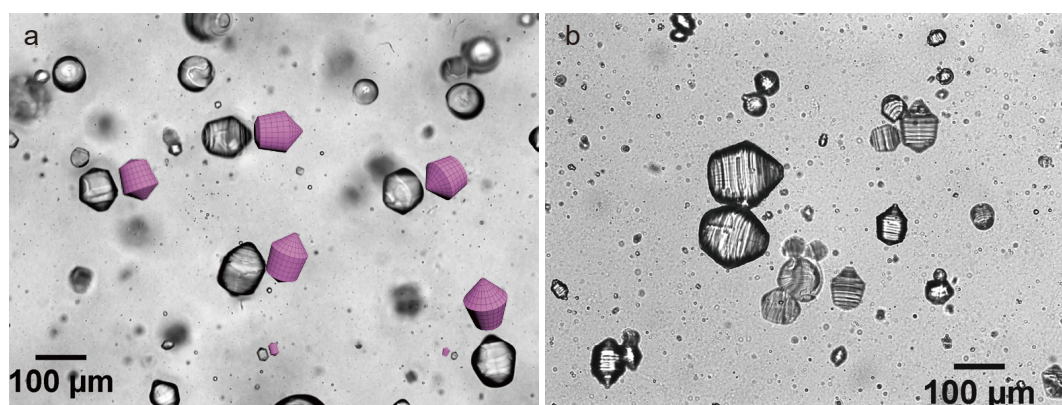


**Figure 3.2:** (a) Optical micrograph of multiple hexosomes formed using the droplet precursor method along with drawn three-dimensional representations of the particle shapes. (b) Details of the circular ridges formed on some hexosomes are visible here, aiding in visualizing their three-dimensional forms.

Micron-scale hexosomes were made using a previously-developed droplet precursor method,<sup>21</sup> with the addition of various hydrophobic additives, vitamin E, divinylbenzene (DVB), hexadecane, and oleic acid (Figure 3.1e), that ensure formation of inverse hexagonal liquid crystalline phase. Emulsion droplets are formed by dispersion of the precursor solution into an aqueous yield stress continuous phase, trapping the droplets and enabling their three-dimensional transformation into liquid crystalline particles. Figure 3.2a and b show optical microscopy images of polydisperse hexosomes formed by this method. The particles have a wide size range that is set by the starting precursor emulsion droplet size distribution, allowing hexosomes to be produced with diameters from at least 1 – 100 μm. Three-dimensional

drawings are also included in Figure 3.2a, indicating the types of shapes formed during the droplet phase transition. In all of our experiments, we typically see a mixture of both spinning top and bicone shapes. The evolution of these shapes as ethanol is removed is the result of the phase transition from isotropic droplets to hexagonal liquid crystalline phase.

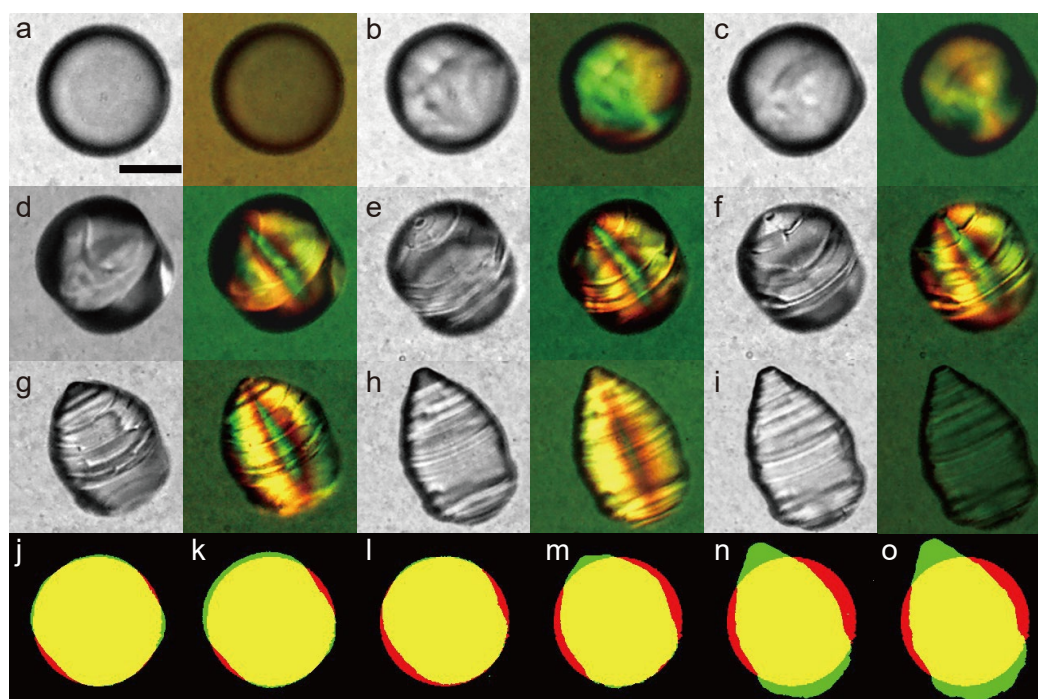


**Figure 3.3:** Transition process from droplet to hexosome for an initial weight ratio of DVB to monoolein  $\mu_{\text{DVB}} = 0.6$ : (a) 36 min, (b) 63 min, (c) 66 min, (d) 76 min, (e) 138 min, (f) 186 min, (g) 263 min, (h) 381 min, (i) 520 min, the left image is under bright field and the right is under polarized light; comparison of droplet precursor with particles formed at (j) 66 min, (k) 76 min, (l) 186 min, (m) 263 min, (n) 381 min, and (o) 520 min from left to right, particles are shown in green, droplet precursor is in red, and the overlapping part is in yellow. Hydrophobic molecule is DVB. Scale bar is  $50 \mu\text{m}$

The transition process from droplet to hexosome is shown in Figure 3.3, with adjacent brightfield and polarized light images indicating, respectively, shape and structural change. The initial emulsion droplet is spherical and isotropic under polarized light, as it is unstructured and interfacial tension dominates droplet rheology

in determination of shape. In Figure 3.3b, 63 min after the droplet precursor is made, the appearance of birefringence indicates that hexagonal phase starts to form, and the shape shows a small change to a more anisotropic form. As ethanol continues to evaporate, vertices grow and become sharper with time, and birefringence becomes more intense, indicating an increasingly ordered microstructure is crystallizing.<sup>58</sup> After about 3 h elapsed time, the shape now has striking rotational symmetry about a clearly visible central axis core, as shown in Figure 3.3a-f. As growth continues, the surface becomes more non-uniform as the particle rheology becomes increasingly elastic, but the circular ridges visible indicate the particle maintains rotational symmetry. The hexosomes in Figure 3.3 are not entirely consistent with past observations of nanoscale hexosomes, which are flat disk-like hexagonal prisms, Figure 3.1b, or spherical shapes, but are similar to the spinning top shape with a spine observed via cryo-SEM (Figure 3.1c and d).<sup>39</sup> The larger-scale hexosomes made here are more easily observed from different orientations via optical microscopy because of their larger size, providing additional information to electron microscopy studies.

After forming their initial shape from the precursor droplets, the hexosomes continue to change shape but their longer axis is still smaller than the diameter of the initial precursors, as shown in the comparison in Figure 3.3j-l. The droplet volume decreases as ethanol diffuses from the droplet to the continuous phase, and the volume of droplet as a function of time is calculated from the microscope images in Figure 3.3 and plotted in Figure A.1. During the first 76 min, the decrease in volume is small, so it is not obvious in Figure 3.3j-l. After that, the volume decreases more significantly. At longer times, Figure 3.3g-i, the particle grows longer along the symmetry axis, increasing particle aspect ratio with time and decreasing the angle at the conical apex. Comparing shapes at longer times in Figure 3.3m-o with the droplet precursor, the hexosome grows outside the initial precursor boundary

at both ends of the central axis, while the diameter perpendicular to the long axis decreases. Figure A.1 shows a decrease in the volume of particle from about 5 h.

Shape evolution of the hexosomes can continue if the hydrophobic additive molecules are permitted to diffuse out of the particles along with the ethanol. In Figure 3.3, DVB is more soluble in the surrounding aqueous environment and more volatile than the monoolein, enabling it to leave the particle and eventually evaporate, consistent with past work on loss of volatile solubilized additives from liquid crystals.<sup>59</sup> At long times, most of the DVB is lost, as is the initial liquid crystalline phase of the hexosomes, indicated by the disappearance of the particle birefringence in the polarized light images in Figure 3.3g-i. In Figure 3.3i, the particle has transformed into a bicontinuous cubic phase after significant loss of the hydrophobic molecule additive to attain or fall below the phase boundary at  $\mu_{\text{DVB}} = 0.04$ . The increased volume may be the result of water entering the particle and further swelling the phase, Figure A.1. The conical morphology doesn't change during the transition from hexosome to cubosome, because the high viscoelasticity can keep the shape unchanged. With longer time, the shape may change, but cannot transform to polyhedron as in Chapter 2, as the growth-by-redistribution process becomes difficult in the highly viscous phase. Growth of large hexosomes from droplets is a way to create particles with unique shapes, and a central aspect of the process is particle mesostructure and its control by additive levels.

### 3.3.2 Shape and phase transition by hydrophobic additives

Figure 3.4a-c examines the shape, using microscopy images, and structure, using SAXS, of hexosomes formed at different initial weight ratios of DVB to monoolein,  $\mu_{\text{DVB}}$ . All particles possess a partial or complete hexagonal liquid crystalline structure, as seen in Figures 3.4a-c. Additional microscope images of particles with the same

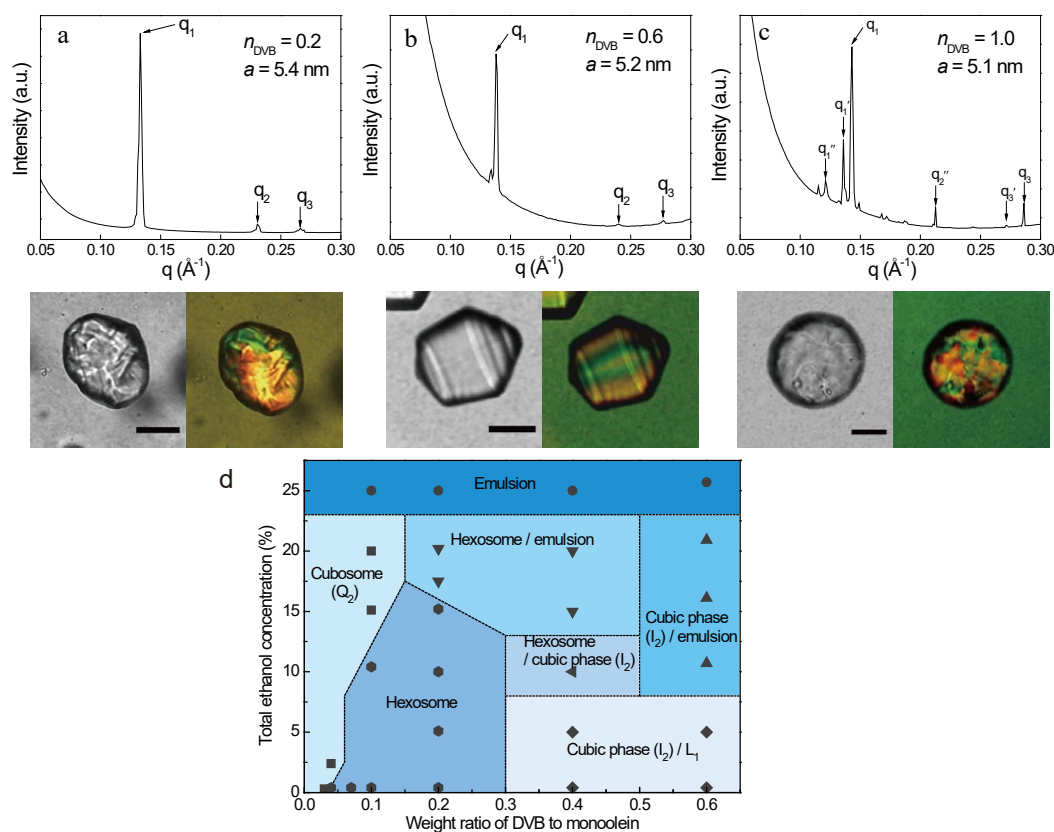


**Figure 3.4:** SAXS and microscope images of hexosomes with different levels of DVB additive, taken 5 hours after initial droplet formation. The precursor solutions contain  $\mu_{\text{DVB}} = 0.2$  (a), 0.6 (b), and 1 (c). The left image is under bright field and the right is under polarized light. Scale bar is 50  $\mu\text{m}$ . (d) Partial phase diagram of DVB-monoolein-ethanol-water system with different weight ratios of DVB to monoolein, and varying concentrations of ethanol.

$\mu_{\text{DVB}}$  are shown in Figure A.2. For the two extreme DVB levels, the birefringence is markedly different to the ordered middle example, indicating that although the system is mostly hexagonal and anisotropic, the hexagonal regions are somewhat disordered or multi-domain. In contrast, the middle example is highly symmetric in its color arrangement and likely an example of a monodomain of hexagonal phase. When  $\mu_{\text{DVB}} = 0.2$ , Figure 3.4a, microscopy indicates the particles are non-spherical, with rounded corners and wrinkles at their surfaces, indicative of a biconical shape but without the distinct rotational symmetry seen in Figure 3.3e-h. However, the

birefringence shown by the particle, and the SAXS result in Figure 3.4a, both indicate the formation of hexagonal phase at this composition.

A partial phase diagram of DVB-monoolein with different weight ratios of water and ethanol, which is based on the birefringence patterns observed in polarizing microscope, is shown in Figure 3.4d, mapping the range of compositions over which the hexosome particles can stably form. Although we focus here on the formation of particles by a kinetic process of solvent removal, the particles shown are often not the final, long-time state of the system. Simulations have shown, however, that the full equilibrium sequence of phase transitions is observed in such processes, so we expect the phase diagrams to be of use in describing the process.<sup>60</sup> During the transition from emulsion droplets to hexosomes, the process is represented by a path from the point of initial concentration to the hexosome region, moving toward the lower left of the phase diagram, as ethanol and DVB both leave the system and their concentrations decrease. At a low  $\mu_{\text{DVB}}$  of 0.2, ethanol can change the system from hexagonal ( $H_2$ ) to cubic phase ( $Q_2$ ). When  $\mu_{\text{DVB}} = 0.2$ , in the transition from emulsion droplets to particles, the composition passes through a cubic phase region, and then goes down to hexagonal phase. The trajectory in phase diagram starts from the emulsion region, and goes down to the left. So cubosomes may form at an early stage of the transition, and then transform to hexosomes. These cubosomes are unnoticed during our observations, possibly because they are not birefringent and only exist for a short time. However, as cubosomes are in a different symmetry and have higher elasticity, their formation can affect the final particle shape, influencing formation of the hexosomes with disordered shapes in Figure 3.4a. At ratios of DVB higher than 0.5, the phase changes from hexagonal to micellar cubic phase ( $I_2$ ). For a starting ratio of  $\mu_{\text{DVB}} = 1.0$ , the trajectory is speculated to pass through the micellar cubic phase region in the phase diagram of Figure 3.4d at an early stage of transition.



The formation of cubic phase in the process also results in the disordered shape in Figure 3.4c. For the initial ratio of  $\mu_{\text{DVB}} = 0.6$ , no other liquid crystal phase forms before hexagonal phase, and the particle shape in Figure 3.4b shows clear hexagonal phase symmetry.

Another possible reason for the irregular shape in Figure 3.4a is that the microstructure of cylindrical micelles cannot pack in an orderly fashion over distances greater than several tens of microns, which is important for the formation of ordered particle shapes.<sup>41</sup> The addition of hydrophobic additives can induce the formation of inverse hexagonal phase by lowering the packing frustration energy of the amphiphile hydrocarbon chains. At a small concentration of hydrophobic additive, e.g.,  $\mu_{\text{DVB}} = 0.2$ , hexagonally-packed cylindrical micelles can have void space between them, requiring hydrocarbon chains to stretch or compress to avoid the empty space, especially at large lattice parameters.<sup>61</sup> More disordered domain arrangements, and greater numbers of defects can then result, as seen in the polarized light image in Figure 3.4a, despite the overall uniformity of hexagonal phase formation. Additional hydrophobic molecules can further decrease the packing frustration energy by filling the void space between cylinders and increasing the hydrophobic moiety.<sup>61</sup> The inverse interfacial curvature is also increased, reducing the lattice parameter, as we see moving from Figure 3.4a to Figure 3.4c in the SAXS data.

Hexosome particles formed at a larger  $\mu_{\text{DVB}} = 0.6$ , Figure 3.4b, exhibit clear spinning top shapes, with a strongly symmetric birefringence pattern that the SAXS result in Figure 3.4b confirms is due to formation of hexagonal phase. When  $\mu_{\text{DVB}} = 0.6$ , particle shapes are rotationally symmetric with a clear order to the birefringent color arrangements in the polarized light image. The improved shape and structure result from increased flexibility of the cylindrical micelles in the mesostructure, allowing

them to bend and form the rotationally symmetric structures with a lower energetic penalty.

When  $\mu_{\text{DVB}}$  increases to 1, the particle shapes lose their symmetry, becoming more spherical, but remain birefringent, Figure 3.4c. The SAXS data in Figure 3.4c show mixed hexagonal phases with different lattice parameters, and weak peaks that may indicate the presence of an micellar cubic phase  $I_2$ . The  $I_2$  phase can form above certain levels of hydrophobic additives in hexagonal phase,<sup>23</sup> indicating a less-ordered polycrystalline microstructure that preferentially forms a spherical particle shape. Other hydrophobic additive molecules can also be accommodated in particles and form hexosomes, broadening applications from synthetic polymeric materials, for example, to food and pharmaceutical components.

The hydrophobic molecule vitamin E acetate was found to form bulk hexagonal phase and nanoparticle hexosomes in previous studies,<sup>30</sup> and we use vitamin E in a similar way here to induce hexosome formation in microscale monoolein emulsions. Figure 3.5a-c shows microscopy images of particles containing different amounts of vitamin E in bright field and polarized light, and the corresponding SAXS data indicate the packing of the lipid domains of the particles. More microscope images of particles with the same  $\mu_{\text{VitE}}$  are shown in Figure A.3. When the weight ratio of vitamin E to monoolein is  $\mu_{\text{VitE}} = 0.05$ , biphasic cubosome-hexosome structures form, Figure 3.5a, with isotropic and birefringent regions like the nanoscale “Janus” particles observed by others using cryo-TEM.<sup>62</sup> Scattering peaks of hexagonal phase, indicated by peak spacing ratios of 1,  $\sqrt{3}$ , and 2, and  $Pn3m$  cubic phase, with peak spacing ratios of  $\sqrt{2}$ ,  $\sqrt{3}$ , and 2, are both found, identified as q and q' in Figure 3.5a respectively.

When more vitamin E is added ( $\mu_{\text{VitE}} = 0.2$ ), biconical hexosomes with strong birefringence form, as shown in Figure 3.5b. The shape is similar to the spinning

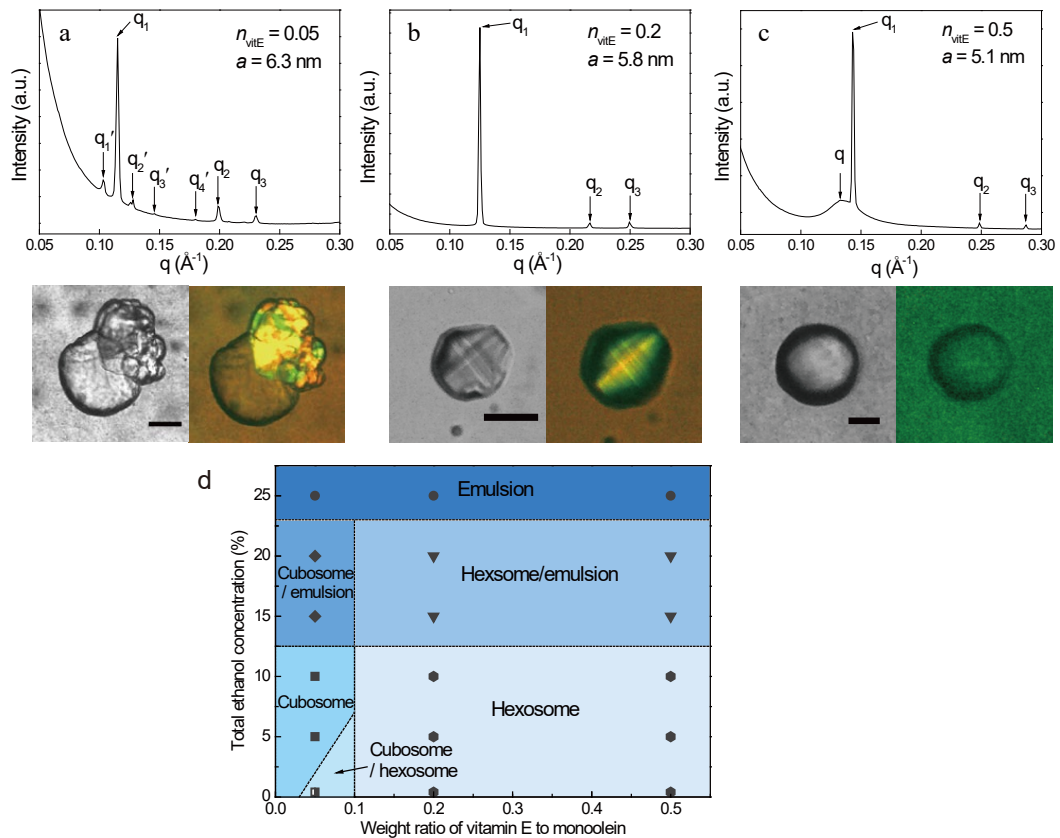


**Figure 3.5:** SAXS and microscope images of hexosomes with addition of vitamin E. The weight ratio of vitamin E to monoolein is  $\mu_{\text{VitE}} =$  (a) 0.05, (b) 0.2, and (c) 0.5, the left image is under bright field and the right is under polarized light. Scale bar is 50  $\mu\text{m}$ . (d) Partial phase diagram of vitamin E-monoolein-ethanol-water system with different weight ratios of vitamin E to monoolein, and varying concentrations of ethanol in excess solvent.

top structure with a raised spine observed by cryo-SEM.<sup>39</sup> SAXS results display the three peaks of hexagonal phase, Figure 3.5b, demonstrating again the ability of the hexagonal phase to form particles with unique rotational symmetry. Upon increasing  $\mu_{\text{VitE}}$  to 0.5, particles lose their non-spherical shape and the birefringence becomes weak, Figure 3.5c, and the SAXS result shows mixed phases are present. In Figure 3.5c, a wide peak  $q$  is visible along with a hexagonal phase, peaks  $q_1$ ,  $q_2$ , and  $q_3$ , which indicates an isotropic phase that dominates the particle behavior.<sup>28,29</sup> The lattice parameter of hexagonal phase,  $a$ , calculated from SAXS data shows that it decreases with  $\mu_{\text{VitE}}$  from 6.3 nm when  $\mu_{\text{VitE}}$  is 0.05, to 5.8 nm when  $\mu_{\text{VitE}}$  is 0.2, and to 5.1 nm when  $\mu_{\text{VitE}}$  is 0.5. Vitamin E has a different type of effect from DVB on the molecular packing in the liquid crystal phase, as its hydroxyl group allows it to be partially hydrated and reduce the level of monoolein hydration.<sup>63</sup> Besides additive levels and phase behavior, kinetic aspects of particle formation can also be used to control hexosome shape, similar to other crystallization processes.

A phase diagram is plotted for the Vitamin E system in Figure 3.5d. Particle formation from the initial droplets occurs by movement from the initial composition straight down vertically, as the ratio  $\mu_{\text{VitE}}$  is unchanged with loss of ethanol. Similar to the DVB system, cubic phases are present at low ratios of Vitamin E to monoolein, below  $\mu_{\text{VitE}} = 0.05$ , which causes "Janus" particle formation. When  $\mu_{\text{VitE}}$  increases to 0.2 and 0.5, the phase and particle shapes are consistent, and the particle formation trajectory has no effect on the resulting shapes.

### 3.3.3 Elasticity of hexosomes

Figure 3.6 shows a summary of the plateau elastic modulus of several different hexagonal phase liquid crystals along with a microscopy image of a typical hexosome formed at that composition. When hexosomes form, similar to bulk hexagonal

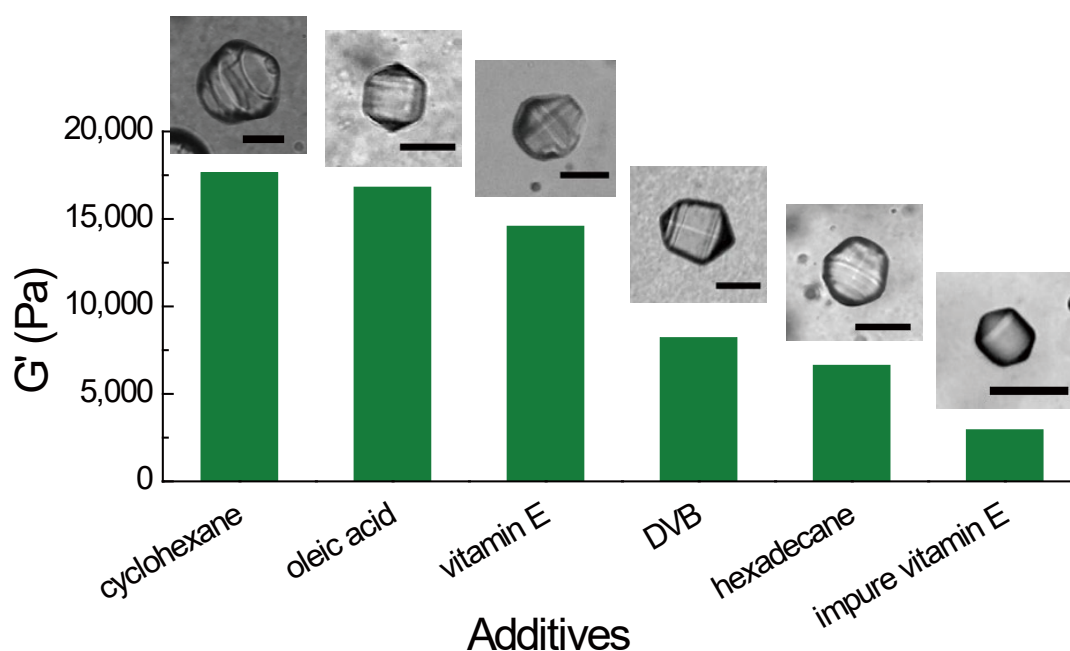
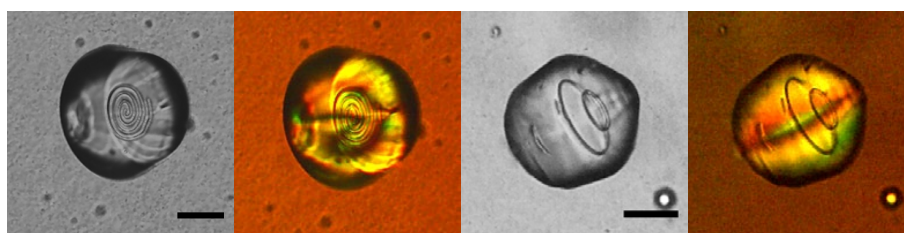


**Figure 3.6:** Plot of the plateau elastic modulus of bulk hexagonal phase for several hydrophobic additives with the same ratio to monoolein,  $\mu_{\text{additive}} = 0.2$ . Microscope images are hexosomes with the same composition as bulk phase. Modulus varies by more than one order of magnitude, but the rotationally symmetric shape remains stable for all cases. Scale bar is 50  $\mu\text{m}$ .

phase,<sup>64</sup> their rheology can vary dramatically. All, however, have sufficient elasticity to resist interfacial tension and maintain a non-spherical shape.<sup>65,66</sup> The values of elastic modulus in Figure 3.6 show that the bulk hexagonal phase ranges from  $10^3 - 10^4$  Pa with a yield stress between 100 – 600 Pa. The Laplace pressure, which drives less solid-like structures back into a spherical shape, is estimated to range from 2 – 200 Pa for particles on the order of 100  $\mu\text{m}$  and an interfacial tension in the range of 0.1 – 10 mN/m.<sup>67,68</sup> An important result of Figure 3.6 is that the elasticity of hexagonal phase can be varied by more than an order of magnitude by including different additive molecules, but it has no effect on the rotationally symmetric shape of hexosomes. It is therefore more likely that the packing of the mesostructure is the crucial determining factor in the shape of a micron-scale hexosome. Besides

preserving a non-spherical shape, the elasticity of the hexosome particles is also useful for preserving a record of the growth process. We can infer possible details about the growth of the liquid crystal-isotropic phase boundary by observing the tracks of growth recorded inside the hexosomes.

### 3.3.4 Ordered microstructure in hexosomes



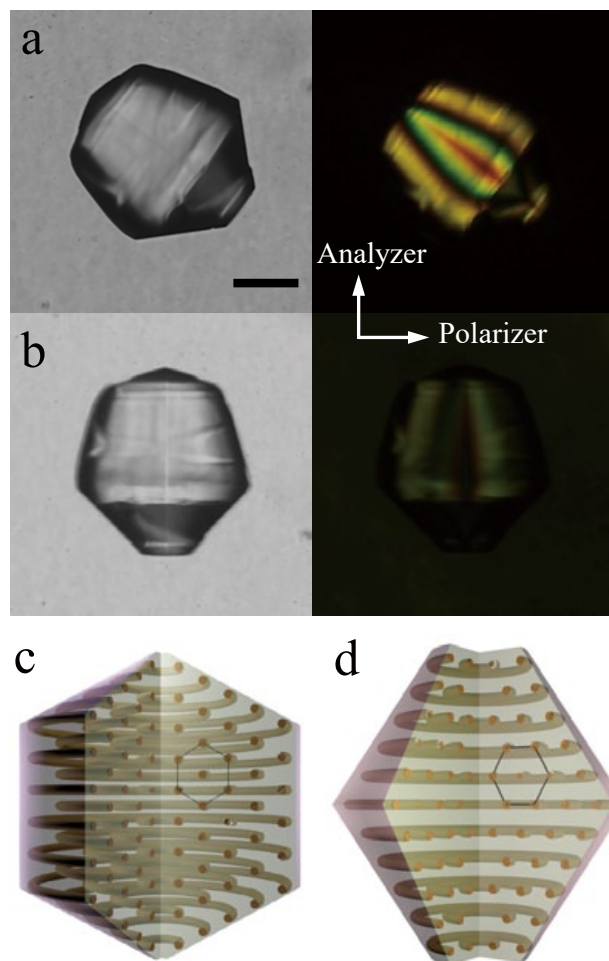
**Figure 3.7:** Microscope image of hexosomes formed at  $\mu_{\text{VitE}} = 0.3$ , with a spiral  $L_1$  phase inclusion inside. Scale bar is 50  $\mu\text{m}$ .

Figure 3.7 shows close-up optical microscopy images of a hexosome formed from vitamin E at a weight ratio of  $\mu_{\text{VitE}} = 0.3$ , where a clear spiral structure is visible at the particle center. Based on past observations in viscoelastic liquid crystalline phases,<sup>21,69</sup> we speculate that the structure is a region of isotropic micellar phase liquid,  $L_1$  enclosed within the hexagonal phase. A similar effect was seen for polyhedral particles of cubic phase, though the  $L_1$  phase inclusions in  $Pn3m$  crystals are faceted shapes inside the larger polyhedral shapes of the overall particle,<sup>21</sup> and can be induced by controlling the crystallization rate.<sup>70,71</sup> Spiral defects are also observed in biomolecular and inorganic solid crystals, indicating the arrangement of repeating units.<sup>72,73</sup> The  $L_1$  inclusion forms because phase separation occurs during the transition process from isotropic emulsion droplets to hexosomes. Some of the water and ethanol accumulates inside the particle and forms  $L_1$  phase, and is more likely to form in larger particles because of slower diffusion. The  $L_1$  inclusion demonstrates that the hexosomes are mostly full of elastic liquid crystal phase and are not

hollow or liquid-filled. Additionally, the spiral  $L_1$  inclusion, as well as the circular lines visible at the surface of hexosomes, Figure 3.4, indicates the rotational trajectory of droplet crystallization, which is helpful to understand how the microstructure and cylindrical micelle packing evolves with time.

Past work indicates the bulk hexagonal phase can form two configurations, straight and ringed cylinders, depending on the length scale of confinement, with ringed cylinders forming at length scale  $r < 200 \mu\text{m}$ .<sup>43</sup> At larger characteristic length scales, straight cylinders can form that are parallel to the capillary axis.<sup>43</sup> The reason for the size effect is that undulation occurs in straight and parallel cylindrical micelles as a result of thermomechanical instability.<sup>74,75</sup> Therefore, a hexagonal phase confined to a length scale smaller than the undulation range interferes with the stability of straight cylinder packing. Deformations are common in single phase domains, and bending of cylinders is the easiest one that occurs in hexagonal phase as the resulting increase in elastic strain energy is lower than for other deformations, such as splay or twist. Curved hexagonally packed cylindrical micelles are frequently observed in inverse hexagonal phase domains<sup>67</sup> and it is likely here that a closed rotating cylinder configuration is the most stable packing for some range of the length scales examined in our droplet studies. When larger than a size of about  $200 \mu\text{m}$ , all the particles possess irregular shapes, as there is no driving force for the rotationally oriented packing to form. Instead, multi-domain hexagonal phases form and can yield disordered particle shapes.

At much smaller length scales, on the order of nanometers, another critical size appears for the concentric and rotating configuration.<sup>76</sup> At such high curvatures, the high bending energy of rotating cylinders prevents their formation, so parallel straight cylinders dominate due to the higher stability. This likely explains why a defect core line forms in the middle of a hexosome, as visible in Figure 3.3e and f,



**Figure 3.8:** Microscopy image of hexosome particle in brightfield (left) and polarized (right) light, when the orientations of a polarizer and an analyzer are perpendicular to each other: (a) the particle locates at a  $45^\circ$  angle to the direction of polarized light from the polarizer; (b) the particle is parallel to the direction of polarized light from the polarizer. Scale bar is  $50\ \mu\text{m}$ . Schematic of two types of hexosome microstructures: (c) and (d). The yellow cylinders indicate the cylindrical micelles. The black hexagons depict the 2D hexagonal ordering of cylinders in the cross section.



and Figure 3.8a and b, and is also observed in other works.<sup>41,43,76</sup> The limited optical resolution of our observations indicates the diameter of the core lines seen here is smaller than 1  $\mu\text{m}$ , and is a function of the stiffness of cylindrical micelles and their crystallization rate. The core size measured for confined bulk phases<sup>43</sup> is much larger than the core we see here, indicating that droplet formation of hexosomes is advantageous for creating different length scale particle structures with clear hexagonal monodomains.

Hexosomes made in this work match the birefringence patterns of bulk hexagonal phase arranged as cylinders wrapped around a central long axis.<sup>43</sup> As Figure 3.8a shows, when the symmetry axis of a hexosome is oriented  $45^\circ$  to the polarizer, a bright, colorful, and symmetric pattern is observed, indicating symmetric arrangement of the cylindrical micelles around the central axis.<sup>43</sup> Also consistent with bulk ringed cylinder results, when the particle is rotated parallel to the polarizer orientation, Figure 3.8b shows that the intensity weakens significantly, indicating these hexosomes have a structure represented by the schematics in Figure 3.8c and d. Different orientations of the hexagonally packed cylinders can lead to further complexity, as the experimentally observed hexosomes often show imperfect shapes versus the shapes drawn in Figure 3.8c and b, and we commonly observe cases where asymmetric cone angles appear. This is likely due to different rates of ordering and formation during transition within the droplets, as well as other defects that can form in bulk hexagonal phases.<sup>67,77</sup> We speculate that nanoparticle hexosomes also have a rotational packing when forming a spinning top shape, like the larger ones we produce here, in agreement with EM studies of block copolymer systems,<sup>42</sup> but more work is needed. Of the other shapes formed in nanoparticle studies, we do not observe formation of flat hexagonal prisms, although it might be possible to produce more two-dimensional shapes using, for example, thin film forms of precursor

droplets. As nanoscale hexosomes are made by the “top-down” method, in which particles form via fragmentation of bulk hexagonal phase, multiple conditions could affect shapes and microstructures, like energy input and temperature. More studies are needed to explain the variations in microstructures and improve control over packing and particle shape.

### 3.4 Conclusions

The work in this chapter demonstrates a new method to produce hexosome particles, using a simple emulsion precursor process, that enables careful study of structure and shape development during liquid crystal formation. Similar to the earlier work on cubic liquid crystalline phases in Chapter 2,<sup>21</sup> this system forms hexagonal phase by removal of solvent from isotropic droplets suspended in a low-viscosity yield stress fluid that allows formation of soft particles without external surface or interfacial effects. The micron-scale hexosomes predominantly form shapes with rotational symmetry, evoking one of several shapes formed by nanoparticle hexosomes. Study of the larger hexosomes indicates a significant degree of control over final particle shape could be attained using experimental variables like droplet size, crystallization rate, and surfactant packing parameter. The findings of work in this chapter can be used, to some extent, to explain past work on nanoparticle shape formation, though the lower boundaries of length scale found here match the upper extremes of nanoparticle hexosome sizes previously studied. More work in Chapter 4 includes using these soft particles as templates for hard particle synthesis in order to explore hierarchical self-assembly<sup>78</sup> by the unique symmetries.

### 3.5 References

- [1] Y. Mai, A. Eisenberg, *Chemical Society Reviews* **2012**, *41*, 5969–5985.

- 
- [2] X. Gong, M. J. Moghaddam, S. M. Sagnella, C. E. Conn, S. J. Danon, L. J. Waddington, C. J. Drummond, *ACS applied materials & interfaces* **2011**, *3*, 1552–1561.
- [3] E. De Santis, M. G. Ryadnov, *Chemical Society Reviews* **2015**, *44*, 8288–8300.
- [4] D. Mandal, A. Nasrolahi Shirazi, K. Parang, *Organic and Biomolecular Chemistry* **2014**, *12*, 3544–3561.
- [5] S. B. Rizwan, B. J. Boyd, T. Rades, S. Hook, *Expert Opinion on Drug Delivery* **2010**, *7*, 1133–1144.
- [6] N. J. Carroll, S. B. Rathod, E. Derbins, S. Mendez, D. A. Weitz, D. N. Petsev, *Langmuir* **2008**, *24*, 658–661.
- [7] C. T. Kresge, M. E. Leonowicz, W. J. Roth, J. C. Vartuli, J. S. Beck, *Nature* **1992**, *359*, 710–712.
- [8] R. G. Laughlin, *The Aqueous Phase Behavior of Surfactants*, Academic Press, London, **1995**, p. 200.
- [9] R. Mezzenga, C. Meyer, C. Servais, A. I. Romoscanu, L. Sagalowicz, R. C. Hayward, *Langmuir* **2005**, *21*, 3322–3333.
- [10] C. J. Drummond, C. Fong, *Current Opinion in Colloid & Interface Science* **2000**, *4*, 449–456.
- [11] P. Spicer in *Encyclopedia of Nanoscience and Nanotechnology*, Marcel Dekker, New York, **2004**, pp. 881–892.
- [12] J. Gustafsson, H. Ljusberg-Wahren, M. Almgren, K. Larsson, *Langmuir* **1996**, *12*, 4611–4613.
- [13] J. Y. T. Chong, X. Mulet, L. J. Waddington, B. J. Boyd, C. J. Drummond, *Langmuir* **2012**, *28*, 9223–9232.
- [14] J. Y. T. Chong, X. Mulet, D. J. Keddie, L. Waddington, S. T. Mudie, B. J. Boyd, C. J. Drummond, *Langmuir* **2014**, 140808144722007.
- [15] M. Almgren, K. Edwards, G. Karlsson, *Colloids and Surfaces A* **2000**, *174*, 3–21.
- [16] K. Larsson, *Current Opinion in Colloid & Interface Science* **2000**, *5*, 64–69.

## References

---

- [17] W.-K. Fong, S. Salentinig, C. A. Prestidge, R. Mezzenga, A. Hawley, B. J. Boyd, *Langmuir* **2014**, *30*, 5373–5377.
- [18] S. Phan, S. Salentinig, C. A. Prestidge, B. J. Boyd, *Drug Delivery and Translational Research* **2013**.
- [19] E. Hinde, K. Thammasiraphop, H. T. T. Duong, J. Yeow, B. Karagoz, C. Boyer, J. J. Gooding, K. Gaus, *Nat. Nanotech.* **2016**, 1–11.
- [20] J. A. Champion, S. Mitragotri, *Proc. Nat. Acad. Sci. USA* **2006**, *103*, 4930.
- [21] H. Wang, P. B. Zetterlund, C. Boyer, B. Boyd, S. W. Prescott, P. T. Spicer, *Soft Matter* **2017**, *13*, 8492–8501.
- [22] P. T. Spicer, K. L. Hayden, M. L. Lynch, A. Ofori-Boateng, J. L. Burns, *Langmuir* **2001**, *17*, 5748–5756.
- [23] S. Phan, W.-K. Fong, N. Kirby, T. Hanley, B. J. Boyd, *International Journal of Pharmaceutics* **2011**, *421*, 176–182.
- [24] R. Wittkowski, H. Löwen, *Phys. Rev. E* **2012**, *85*, 1–12.
- [25] L. De Campo, A. Yaghmur, L. Sagalowicz, M. E. Leser, H. Watzke, O. Glatter, *Langmuir* **2004**, *20*, 5254–5261.
- [26] W.-K. Fong, T. Hanley, B. J. Boyd, *Journal of Controlled Release* **2009**, *135*, 218–226.
- [27] W.-K. Fong, T. L. Hanley, B. Thierry, A. Tilley, N. Kirby, L. J. Waddington, B. J. Boyd, *Physical Chemistry Chemical Physics* **2014**, *16*, 24936–24953.
- [28] A. Yaghmur, L. De Campo, L. Sagalowicz, M. E. Leser, O. Glatter, *Langmuir* **2005**, *21*, 569–577.
- [29] A. Yaghmur, L. De Campo, S. Salentinig, L. Sagalowicz, M. E. Leser, O. Glatter, *Langmuir* **2006**, *22*, 517–521.
- [30] Y.-D. Dong, I. Larson, T. Hanley, B. J. Boyd, *Langmuir* **2006**, *22*, 9512–9518.
- [31] K. J. Tangso, H. Patel, S. Lindberg, P. G. Hartley, R. Knott, P. T. Spicer, B. J. Boyd, *ACS applied materials & interfaces* **2015**, *7*, 24501–24509.
- [32] S. Salentinig, L. Sagalowicz, O. Glatter, *Langmuir* **2010**, *26*, 11670–11679.

- 
- [33] I. Amar-Yuli, E. Wachtel, E. B. Shoshan, D. Danino, A. Aserin, N. Garti, *Langmuir* **2007**, *23*, 3637–3645.
- [34] R. Mezzenga, P. Schurtenberger, A. Burbidge, M. Michel, *Nature materials* **2005**, *4*, 729–740.
- [35] M. Rosa, M. Rosa Infante, M. d. G. Miguel, B. Lindman, *Langmuir* **2006**, *22*, 5588–5596.
- [36] M. Johnsson, Y. Lam, J. Barauskas, F. Tiberg, *Langmuir* **2005**, *21*, 5159–5165.
- [37] C. Neto, G. Aloisi, K. Larsson, *J. Phys. Chem. B* **1999**, *103*, 3896–3899.
- [38] M. Almgren, K. Edwards, G. Karlsson, *Colloids and Surfaces A: Physicochemical and Engineering Aspects* **2000**, *174*, 3–21.
- [39] B. J. Boyd, S. B. Rizwan, Y.-D. Dong, S. Hook, T. Rades, *Langmuir* **2007**, *23*, 12461–12464.
- [40] J. Qi, H. Nan, D. Xu, Q. Cai, *Crystal Growth & Design* **2011**, *11*, 910–915.
- [41] J. Jeong, Z. S. Davidson, P. J. Collings, T. C. Lubensky, A. Yodh, *Proceedings of the National Academy of Sciences* **2014**, *111*, 1742–1747.
- [42] Z. Lin, S. Liu, W. Mao, H. Tian, N. Wang, N. Zhang, F. Tian, L. Han, X. Feng, Y. Mai, *Angewandte Chemie International Edition* **2017**, *56*, 7135–7140.
- [43] T. Oka, N. Ohta, *Langmuir* **2016**, *32*, 7613–7620.
- [44] B. J. Boyd, *Int. J. Pharmaceutics* **2003**, *260*, 239–247.
- [45] L. Hong, S. Salentinig, A. Hawley, B. J. Boyd, *Langmuir* **2015**, *31*, 6933–6941.
- [46] X. Mulet, B. J. Boyd, C. J. Drummond, *Journal of colloid and interface science* **2013**, *393*, 1–20.
- [47] X. Banquy, F. Suarez, A. Argaw, J.-M. Rabanel, P. Grutter, J.-F. Bouchard, P. Hildgen, S. Giasson, *Soft Matter* **2009**, *5*, 3984.
- [48] F. R. Kersey, T. J. Merkel, J. L. Perry, M. E. Napier, J. M. DeSimone, *Langmuir* **2012**, *28*, 8773–8781.
- [49] T. J. Merkel, S. W. Jones, K. P. Herlihy, F. R. Kersey, A. R. Shields, M. Napier, J. C. Luft, H. Wu, W. C. Zamboni, A. Z. Wang, J. E. Bear, J. M. DeSimone **2011**, *108*, 586–591.
- [50] P. Salo-Väänänen, V. Ollilainen, P. Mattila, K. Lehikoinen, E. Salmela-Mölsä, V. Piironen, *Food Chemistry* **2000**, *71*, 535–543.

## References

---

- [51] C. A. Schneider, W. S. Rasband, K. W. Eliceiri, *Nature Methods* **2012**, *9*, 671–675.
- [52] I. Dierking, *Textures of liquid crystals*, John Wiley & Sons, **2003**.
- [53] F. Rosevear, *Journal of the American Oil Chemists' Society* **1954**, *31*, 628–639.
- [54] F. Livolant, Y. Bouligand, *Journal de Physique* **1986**, *47*, 1813–1827.
- [55] N. M. Kirby, S. T. Mudie, A. M. Hawley, D. J. Cookson, H. D. Mertens, N. Cowieson, V. Samardzic-Boban, *J. Appl. Cryst.* **2013**, *46*, 1670–1680.
- [56] S. Mudie, *Scatterbrain software*, [www.synchrotron.org.au](http://www.synchrotron.org.au), **2017**.
- [57] S. Soni, G. Brotons, M. Bellour, T. Narayanan, A. Gibaud, *The Journal of Physical Chemistry B* **2006**, *110*, 15157–15165.
- [58] E. A. Wood, *Crystals and light: an introduction to optical crystallography*, Courier Corporation, **1977**.
- [59] I. Martiel, L. Sagalowicz, S. Handschin, R. Mezzenga, *Langmuir* **2014**, *30*, 14452–14459.
- [60] P. Warren, P. Prinsen, M. Michels, *Philosophical Transactions of the Royal Society of London A: Mathematical Physical and Engineering Sciences* **2003**, *361*, 665–676.
- [61] G. Shearman, O. Ces, R. Templer, J. Seddon, *Journal of Physics: Condensed Matter* **2006**, *18*, S1105.
- [62] N. Tran, X. Mulet, A. M. Hawley, C. E. Conn, J. Zhai, L. J. Waddington, C. J. Drummond, *Nano letters* **2015**, *15*, 4229–4233.
- [63] L. Sagalowicz, S. Guillot, S. Acquistapace, B. Schmitt, M. Maurer, A. Yaghmur, L. De Campo, M. Rouvet, M. Leser, O. Glatter, *Langmuir* **2013**, *29*, 8222–8232.
- [64] I. Amar-Yuli, E. Wachtel, D. E. Shalev, A. Aserin, N. Garti, *Journal of Physical Chemistry B* **2008**, *112*, 3971–3982.
- [65] A. Pawar, M. Caggioni, R. Hartel, P. Spicer, *Faraday Discussions* **2012**, *158*, 341–350.
- [66] M. Caggioni, A. Bayles, J. Lenis, E. Furst, P. Spicer, *Soft Matter* **2014**, *10*, 7647–7652.
- [67] J. M. Seddon, *Biochimica et Biophysica Acta (BBA)-Reviews on Biomembranes* **1990**, *1031*, 1–69.
- [68] S. Guttman, Z. Sapir, B. M. Ocko, M. Deutsch, E. Sloutskin, *Langmuir* **2017**, *33*, 1305–1314.

- 
- [69] M. L. Lynch, K. A. Kochvar, J. L. Burns, R. G. Laughlin, *Langmuir* **2000**, *16*, 3537–3542.
- [70] P. Pieranski, M. Bouchih, N. Ginestet, S. Popa-Nita, *The European Physical Journal E* **2003**, *12*, 239–254.
- [71] L. Latypova, W. Gózdź, P. Pieranski, *The European Physical Journal E* **2013**, *36*, 88.
- [72] A. Malkin, Y. G. Kuznetsov, A. McPherson, *Journal of crystal growth* **1999**, *196*, 471–488.
- [73] J. N. Clark, J. Ihli, A. S. Schenk, Y.-Y. Kim, A. N. Kulak, J. M. Campbell, G. Nisbet, F. C. Meldrum, I. K. Robinson, *Nature materials* **2015**, *14*, 780–784.
- [74] M. Impérator-Clerc, P. Davidson, *The European Physical Journal B-Condensed Matter and Complex Systems* **1999**, *9*, 93–104.
- [75] P. Oswald, J.-C. Géminard, L. Lejcek, L. Sallen, *Journal de Physique II* **1996**, *6*, 281–303.
- [76] R. Zhang, X. Zeng, B. Kim, R. J. Bushby, K. Shin, P. J. Baker, V. Percec, P. Leowanawat, G. Ungar, *ACS nano* **2015**, *9*, 1759–1766.
- [77] M. Kleman, *Journal de Physique* **1980**, *41*, 737–745.
- [78] P. F. Damasceno, M. Engel, S. C. Glotzer, *Science* **2012**, *337*, 453–457.





## Chapter 4

# Polymerization of cubosome and hexosome templates to produce complex microparticle shapes

### 4.1 Introduction

Self-assembly of aqueous amphiphilic molecules is a powerful route to control of structure and morphology at multiple useful length scales. A commonly-studied material is glycerol monoolein, a non-ionic amphiphilic monoglyceride that forms cubic,<sup>1</sup> lamellar, and hexagonal<sup>2</sup> liquid crystalline phases in water. Most concentrated surfactant liquid crystalline phases have valuable structures with high porosity and surface area, but lose their structure at high dilutions, forming micelles.<sup>3</sup> The unique low solubility of monoolein, however, drives two-phase liquid crystalline-water phase behavior even at high dilutions. As a result, dispersed particles of cubic or hexagonal liquid crystalline phase, known as cubosomes and hexosomes, respectively,<sup>4,5</sup> can be produced and are often studied as reservoirs for solubilized biomolecules.<sup>6,7</sup> Nanoparticle cubosomes and hexosomes are often shaped, respectively, as cubes<sup>8</sup> and flat hexagonal prisms,<sup>9</sup> while microparticle examples have recently been shown to exhibit a much wider range of shapes with multifaceted polyhedral<sup>10</sup> and cylindrical symmetries<sup>11</sup> depending on their microstructure and formation kinetics (Chapters 2 and 3). Although nanoscale structures in liquid crys-

---

This chapter originally published as Wang, H.; Zetterlund, P. B.; Boyer, C.; & Spicer, P. T. "Polymerization of cubosome and hexosome templates to produce complex microparticle shapes" *Journal of Colloid and Interface Science*, **2019**, 546, 240-250

talline phases have value in catalysis and energy storage,<sup>12</sup> extensive simulations of colloidal self-assembly indicate larger-scale facets<sup>10</sup> and novel symmetries<sup>11</sup> could enable production of dynamic photonic and composite advanced materials.<sup>13,14</sup> A key next step is then the robust and flexible production of such complex solid particle shapes from variable templates.

Self-assembled liquid crystalline particles can serve as templates for production of solid non-spherical particles with complex shape and microstructure. Cubic and hexagonal liquid crystals are broadly useful templates, as their elasticity allows them to be deformed, molded, and otherwise adapted without destroying the underlying crystallinity that can impart order, high surface area, and porosity.<sup>15,16</sup> Past work templating liquid crystalline materials by silica precipitation has focused on the production of bulk inorganic catalytic monoliths,<sup>17</sup> randomly varying nanoparticle shapes,<sup>18</sup> and spherical micron-scale particles with nanometer-scale pore structures.<sup>19,20</sup> Mesoporous carbon particles with ordered polyhedral shapes were produced using a similar precipitation process with block copolymers as templates, with some control of the size and shape of particles.<sup>21,22</sup> There are also numerous examples of polymeric materials formed using other templates, for example, capsules templated by spherical unilamellar vesicles,<sup>23-25</sup> and polymeric platelets made from anisotropic crystallized oil droplet templates.<sup>26</sup> Yang et al.<sup>27</sup> suggested cubosome nanoparticles could be polymerized, and cubic and hexagonal liquid crystalline bulk phases have previously been used as templates for polymerization,<sup>28-32</sup> but no resulting structures have been shown. We know of no previous work focusing on templating unique micron-scale geometric shapes from dispersed liquid crystalline phases, especially the novel polyhedra recently developed.<sup>10,11</sup>

Given the potential applications of complex-shaped colloids, key priorities for study include the degree of structure preservation during templating and the con-

trolled production of faceted symmetric shapes. The mechanical properties of the resulting particles are also increasingly important,<sup>33–35</sup> as deformability enhances biological circulation times and accumulation<sup>36</sup> affects cell uptake and cell trafficking of particles.<sup>37</sup>

In this chapter we study the photopolymerization of micron-scale cubosomes and hexosomes which are made as in Chapter 2 and 3,<sup>10,11</sup> producing polymeric particles with controlled complex shape and elasticity. Photopolymerization transforms the self-assembled structures into strongly bonded networks that preserve unique precursor shapes, even after removal of the lipid template. Varying precursor template and composition controls particle size and shape, and elasticity is tuned by monomer choice. The exploration of template stability and particle shapes produced in various monomer systems is intended to broaden the applications of shaped polymeric particles as advanced material components and novel carriers for active compounds. For example, the polymerized particles can mimic red blood cells, viruses, and organelles, which are also elastic and in anisotropic shapes, and the flexibility of particles may change circulation time and lead to accumulation in specific organs. When flowing in fluid, particles with different elasticity, size, and shape can behave in different ways, which enables them to be models in particle separation.

## 4.2 Materials and methods

Commercial grade monoolein, Dimodan MO90K, was obtained from DuPont Danisco (Botany, NSW, Australia). The phase behavior of this system matches that of pure monoolein, in agreement with our earlier work and consistent with more detailed studies.<sup>38,39</sup> The additives 99% ethanol and Pluronic F-127 were purchased from Sigma Aldrich (Castle Hill, NSW, Australia). Carbopol 846 was obtained from Lubrizol

(Silverwater, NSW, Australia). Microfibrillated cellulose, MFC, was purchased from Wong Coco (Jakarta, Indonesia). Monomers divinylbenzene (DVB), 1,6-hexanediol diacrylate (HDDA), di(ethylene glycol) dimethacrylate (DEGDMA), ethylene glycol dimethacrylate (EGDMA), N,N'-methylenebisacrylamide (MBAm) and the photoinitiator (PI) RGACURE 819 were purchased from Sigma Aldrich. All chemicals were used without further purification. Ultra-pure water with a resistivity of 18.25 M $\Omega$ -cm was obtained using a Sartorius Ultrapure water purifier.

Template particles were prepared by the method in Chapters 2 and 3 of combination of 0.02 – 0.2 mL precursor solution and 3.5 mL of a diluting solution, both compositions vary depending on the desired particle type.<sup>10,11</sup> Precursor solutions contained a 1:1 weight ratio of monoolein:ethanol and desired weight percentage of monomers and photoinitiator, PI. Diluting solutions contained water, ethanol, and a yield stress fluid, 0.1% w/w MFC or aqueous Carbopol 846 to stabilize the resulting particles. The ethanol concentration in the diluting solution was 25% v/v. Water insoluble monomers, DVB, HDDA, DEGDMA, and EGDMA, were dissolved in precursor solution, while water soluble monomer, MBAm, was dissolved in the dilution solution. Mixing the two solutions, by injecting precursor into the dilution solution with a syringe, forms emulsion droplets that can be controllably transformed into template particles of polyhedral cubosomes<sup>10</sup> or spinning-top hexosomes<sup>11</sup> by evaporation of ethanol from the suspension.

The emulsion was placed in an open Petri dish with a liquid height of 4 mm and a free surface area of 9.6 cm<sup>2</sup> to facilitate evaporation of ethanol. The sample was held at constant T = 25 °C and relative humidity = 60% in a static environment during the transition process from droplets to particles. The initial evaporation rate was about 2.3 mg/min measured in Chapter 2.<sup>10</sup> All experiments were conducted at 25 °C, and template particle formation experiments were carried out in dark conditions. The

degree and rate of evaporation can be used to control initial particle shape,<sup>10,11</sup> while subsequent polymerization can then lock in the shape for longer-term applications.

Once the desired shapes were formed after 5 h of ethanol evaporation, particles were transferred to a closed vial in a Rayonet reactor (Model RPR-200) equipped with 16 RPR-3000A lamps ( $\lambda = 300$  nm), and irradiated by UV light for the desired reaction time. After polymerization, the resulting particles were washed with water to remove any yield stress fluid, and then washed with ethanol to remove templates and unreacted monomers. Particles were centrifuged and collected after washing.

Particle observations were conducted on a Leica DM2500M optical microscope and images recorded using a Moticam 10MP digital camera. Micrographs shown here portray shapes representative of dispersions with more than 100 particles in a sample.

SEM observations were conducted on a FEI Nova NanoSEM 450 FE-SEM microscope at an accelerating voltage of 5 kV.

## 4.3 Results and discussion

### 4.3.1 Template synthesis

Liquid crystalline cubosomes and hexosomes were produced from controlled-size emulsion droplet precursors by removing solvent to crystallize a desired shape.<sup>10,11</sup> Suspension of the precursor droplets in a weak yield stress fluid ensures stability against aggregation and allows microscopic study of the shapes produced (Figure 4.1a and b). The liquid crystalline structure of template particles can solubilize certain levels of additives, like monomers, without changing particle shape and microstructure, though varying monomer hydrophobicity can determine whether cubosomes or hexosomes form. Polymer particles with well-templated shapes form if

the interactions of amphiphile, monomer, and initiator during photopolymerization do not disrupt the initial shapes, Figure 4.1c.

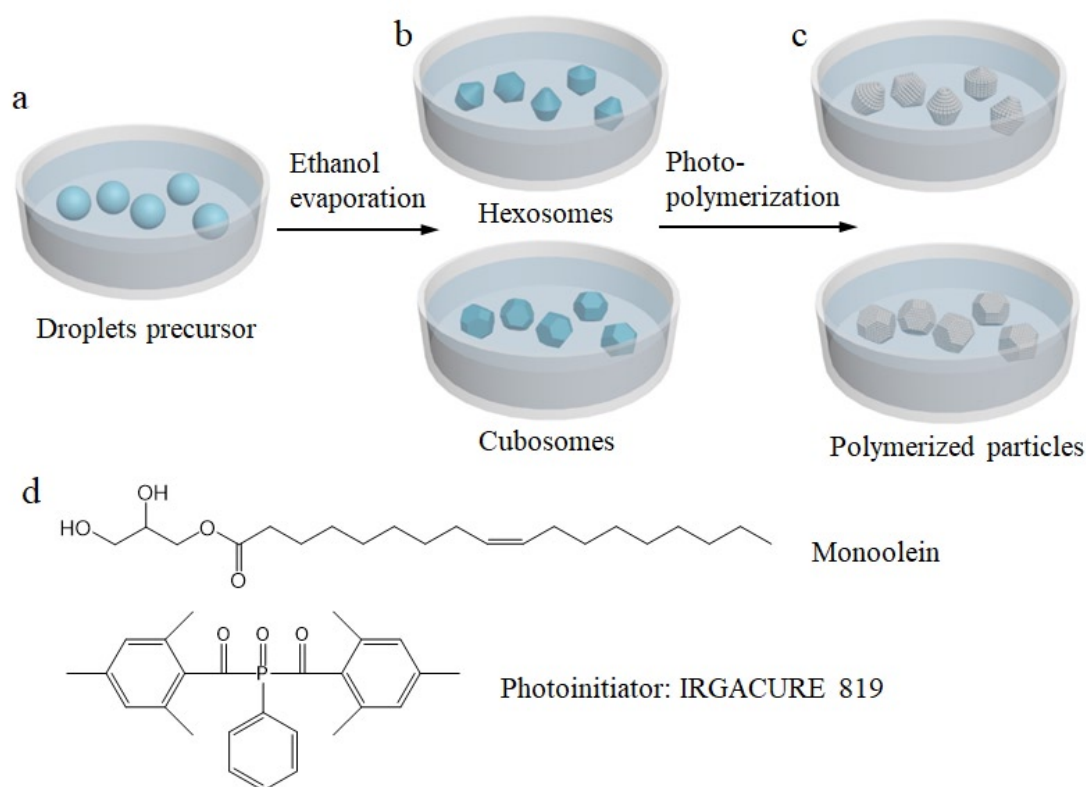


**Figure 4.1:** Schematic of formation of liquid crystalline particles (a, b), polymerization for shape preservation (c), and molecular structures of the amphiphile monoolein and photoinitiator used in all particle production (d).

### 4.3.2 Polymerization of hexosomes by hydrophobic monomers

Hydrophobic additives alter the molecular packing of self-assembled monoolein, transforming cubosomes into hexosomes,<sup>11</sup> so we first explore the polymerization of divinylbenzene (DVB) monomer to produce cylindrical crosslinked particles with hexagonal symmetry. Figure 4.2 shows microscopy images of hexosomes containing DVB before polymerization at initial weight ratios of DVB:monoolein,  $\mu_{\text{DVB}}$ , ranging from 0.4 to 0.8. The particles have rotational symmetry and spinning-top shapes<sup>40,41</sup> as well as birefringence under polarized light (Figure 4.2a, d, and e). Particles remain

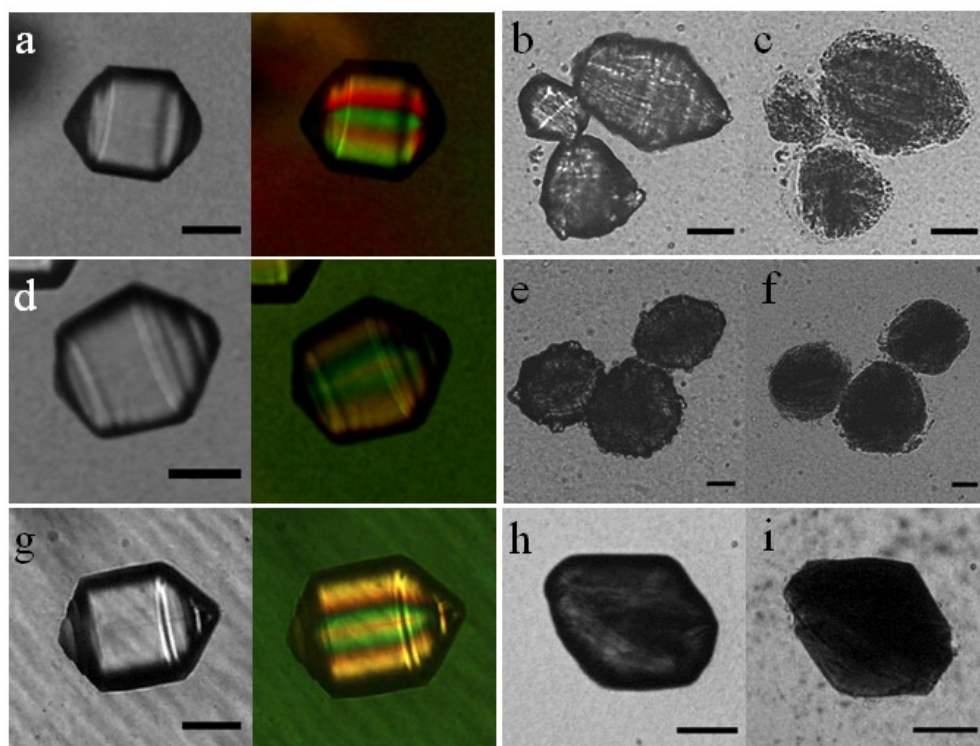


**Figure 4.2:** Hexosomes before and after polymerization with  $\mu_{\text{DVB}} = 0.4$  (a-c), 0.6 (d-f), and 0.8 (g-i). For a, d, and g, the left images are under bright field, and the right are under polarized light. Polymerized particles are before (b, e, and h) and after (c, f, and i) removing monoolein. The mass ratio of DVB to PI  $m_{\text{DVB}} : m_{\text{PI}} = 20 : 1$ . Scale bar is 50  $\mu\text{m}$ .

in the hexagonal phase and retain their shapes for  $\mu_{\text{DVB}} = 0.4 - 0.8$ , but lose their structure when  $\mu_{\text{DVB}} < 0.2$ , or form mixed phases when  $\mu_{\text{DVB}} > 1.0$ .<sup>11</sup> Both DVB and ethanol can diffuse out of the particle over time, but the ethanol diffusion rate is presumed to be faster based on molecular polarity and solubility, ensuring transition to hexosome shapes that contain sufficient monomer for subsequent polymerization. Small-angle X-ray scattering (SAXS) confirms the hexagonal phase structure of the hexosome precursors, indicated by spacing ratios of 1,  $\sqrt{3}$ , and 2 (Figure B.1a).

Photopolymerization under UV light was conducted at room temperature for 30 min to create a crosslinked polymer network in the liquid crystalline particles and fix the shape of the hexosome template. SAXS measurement of the particles after

polymerization, but before removal of the monoolein templates, reveals peaks of hexagonal phase (Figure B.1b). After polymerization, the particles appear darker when observed via optical microscopy as a result of increased density and opacity (Figure 4.2b, e, and h), with higher concentrations of DVB producing darker, denser particles. Importantly, after polymerization the particles have the same spinning-top hexosome shapes as the precursors, and subsequent dissolution of monoolein does not significantly change the solid form (Figure 4.2c, f, and i). Similarly, no significant change in particle appearance is observed for polymerization times from 30 min to 6 h. An increase in the amount of DVB leads to improved preservation of the original particle shape (Figures 4.2c, f, and i) – as anticipated, there is clearly a minimum amount of polymer and crosslinking needed to preserve the structural integrity of these shapes during template polymerization.

Particles formed using higher levels of photoinitiator have similar morphology (Figure B.2), demonstrating some flexibility in the amount of photoinitiator that can be used. Polymerized particles with a size larger than 100  $\mu\text{m}$  collapse after removal of the lipid template (Figure 4.3d and e), presumably due to limited penetration depth of UV light during polymerization that results in insufficient internal polymerization and poor, or non-uniform, mechanical integrity.

The SEM images in Figure 4.3 show the three-dimensional structure of the polymerized hexosomes in Figure 4.2 following template removal. The particles in Figure 4.3a-c exhibit the same spinning-top shape as the hexosome templates in Figure 4.2, displaying curved faces as well as sharp vertices and edges. More images of particles are shown in Figure B.3. Close-up observation reveals that the structure is composed of fused nano-scale polymer spheres (Figure 4.3f). Clearly the templating of these shapes occurs by selectively localized formation of the polymer spheres. For  $\mu_{\text{DVB}} = 0.6 - 0.8$ , the overall particles are similar in microstructure after polymer-



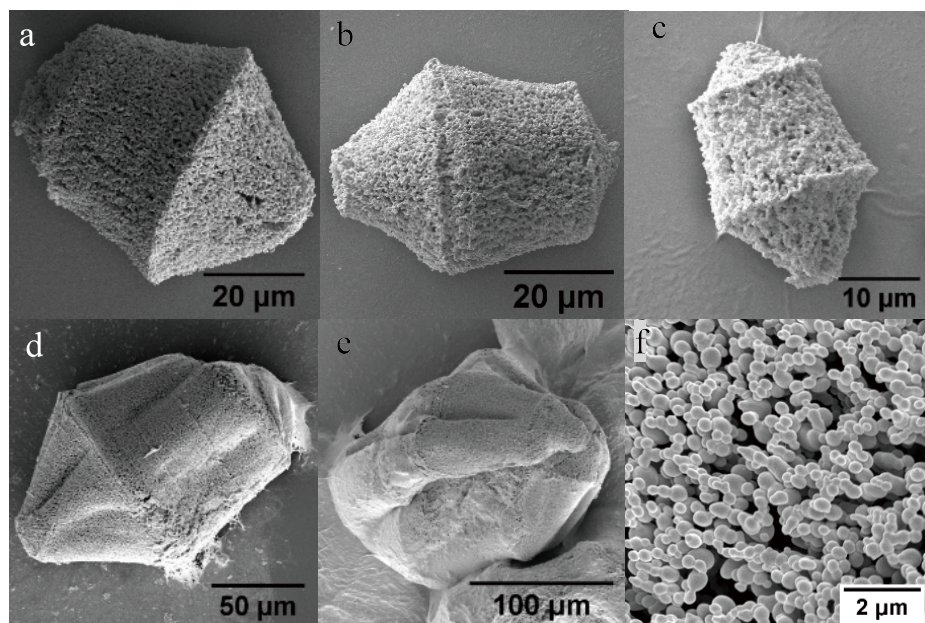


**Figure 4.3:** SEM micrographs of polymerized hexosomes (a-e), and a zoom-in image of nano polymer spheres (f), mass ratios  $m_{\text{monoolein}} : m_{\text{DVB}} : m_{\text{PI}} = 1 : 0.8 : 0.08$  (a-c, f),  $1 : 0.6 : 0.03$  (d and e).

ization, with the primary polymer spheres ranging in size from 200 – 500 nm. The similar microstructure with different DVB ratios is probably due to the interaction between polymer chains in the domains formed by the self-assembled monoolein.<sup>28</sup>

The repeating unit of the hexagonal phase is approximately 5 nm, calculated from the SAXS results in Figure B.1.<sup>11</sup> However, the polymer spheres formed within the particles are one hundred times larger than the lattice parameters of the liquid crystal. For the DVB polymerization, we conclude that only the microscale structure and shape is preserved during templating because the smaller scale structures are below the “resolution” of this process. When larger size hexosomes are templated, as in Figure 4.3d and e, the final structures tend to exhibit some folding or wrinkling. The additional changes in shape may occur during the removal of the liquid crystalline template, or during SEM sample preparation.

The interior microstructure of the polymerized particle was observed after milling by focused ion beam (FIB) treatment (Figure B.4). The interior is quite porous – study via SEM of an FIB-drilled hole with a depth of about 30  $\mu\text{m}$  demonstrates that the particle is not hollow.

In order to determine the effect of the liquid crystalline mesostructure on the polymerization templating process, unstructured spherical precursor emulsion droplets were also polymerized using the same process as above (Figure B.5a). Before evaporation of ethanol, emulsion droplets were spherical rather than exhibiting ordered shapes, as the isotropic solution has not transformed into hexagonal phase. The spherical shape of the droplets was preserved during polymerization, and the particles possess a microstructure of nanoparticle spheres (Figure B.5b) identical to the hexosome forms in Figure 4.3f. Homogeneous precursor solution was also polymerized directly without being dispersed into droplets and produces the same length scale nanoparticle spheres (Figure B.5c). The polymeric nanoparticles of dimensions 200 – 500 nm presumably originate from a polymerization process similar to a precipitation/dispersion polymerization.<sup>42,43</sup> Initially, the monomer DVB is soluble within the large microparticles. As initiation occurs, chains form and grow in length until they become insoluble at the so-called critical degree of polymerization, which leads to particle formation. The fact that similar nanoparticles are formed with or without the liquid crystalline mesostructure as template is consistent with this basic rationale. The above process thus offers a means of templating micron-scale structures and shapes but is not useful for preserving finer-scale features of the templates.

Other hydrophobic monomers produced similar results. 1,6-Hexanediol diacrylate (HDDA) allowed formation of biconical hexosome templates from emulsion droplets (Figures B.6a and b). The resulting polymerized particles also exhibited biconical shapes, as observed by microscopy and SEM imaging (Figure B.6c-f).

### 4.3.3 Polymerization of cubosomes by hydrophobic monomers

Although polymerization of hexosome structures allows production of particles with a controlled cylindrical symmetry, other shapes are also desirable to broaden our ability to form hierarchical mesoscale structures.<sup>13,14</sup> The polymerization approach used for hexosome particle templates is also applicable to the six different polyhedral shapes that micron-scale cubic liquid crystalline particles can form.<sup>10</sup> Formation of cubic liquid crystalline microparticle templates requires tuning the system phase behavior to a lower interfacial curvature than required to form hexagonal phase.<sup>44</sup> A more polar monomer than DVB and HDDA, di(ethylene glycol) dimethacrylate (DEGDMA), allows formation of a cubic instead of hexagonal phase. We find DEGDMA is also desirable in that it does not prevent formation of the polyhedral cubosome shapes we previously produced without monomer present.<sup>10</sup> Figure 4.4a and b show faceted particles with a truncated octahedron shape are formed, consistent with our previous work where we verified these shapes only form when SAXS data show cubic phase is present.<sup>10</sup> More data are needed to verify the properties of the cubic phase that forms when the DEGDMA monomer is present.

The polyhedral shapes of the particles were retained upon photopolymerization (Figure 4.4c-h). Similar to the hexosome results in Figure 4.2, the polymerized cubosomes in Figure 4.4c-f become darker after polymerization as the solid polymer forms and density increases. The solid form of the particle is somewhat porous, allowing sufficient transmission of light to make visible the facets on its opposite side, confirming the three-dimensional polyhedral form in Figure 4.4c and d. After removal of the monoolein template by dissolution, the resulting polymeric particles retained the original shapes of the templates (Figure 4.4e and f), just as we saw earlier for the hexosomes (Figure 4.2). The quality of shape retention increased

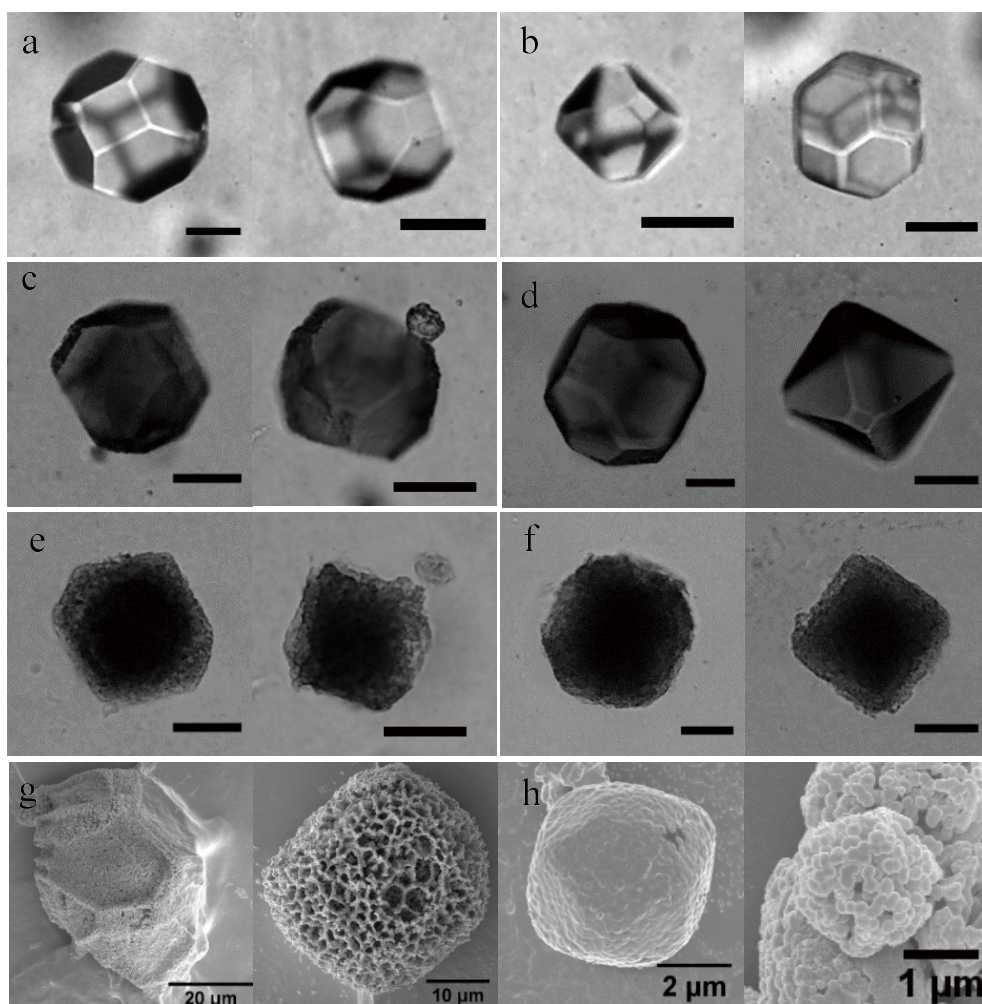


**Figure 4.4:** Polyhedral particles incorporating DEGDMA monomer before polymerization. Initial mass ratios  $m_{\text{monoolein}} : m_{\text{DEGDMA}} = 1 : 0.6$  (a), and  $1 : 1.0$  (b). Polymerized particles are before (c, d) and after (e, f) removing the template. Initial mass ratios  $m_{\text{monoolein}} : m_{\text{DEGDMA}} : m_{\text{PI}} = 1 : 0.6 : 0.03$  (c, e), and  $1 : 0.8 : 0.03$  (d, f). Scale bar is  $50 \mu\text{m}$ . SEM micrographs of polymerized cubosomes with the initial mass ratios,  $m_{\text{monoolein}} : m_{\text{DEGDMA}} : m_{\text{PI}} = 1 : 0.7 : 0.03$  (g), and  $1 : 1 : 0.03$  (h).

with increasing monomer concentration (Figure 4.4e and f), as a sufficiently robust polymer network is a requirement for optimal mechanical shape preservation.

SEM images (Figure 4.4g and h) show that the polyhedral shapes of polymerized particles are on the length scale 2 – 50  $\mu\text{m}$ . They are made up of nanoscale spheres without ordered morphology, indicating that the polymerization is similar to that discussed above for the hexosomes (Figure 4.3). The particle depicted in Figure 4.4g has collapsed, and in other particles porous structures have formed. For particles with smaller sizes and higher concentrations of monomer, structures are denser (Figure 4.4h).

Similar results are obtained using a monomer with a molecular structure that is quite close to DEGDMA, ethylene glycol dimethacrylate or EGDMA. Images of polyhedral particles before and after polymerization are shown in Figure B.7.

#### **4.3.4 Soft polymerized particles by hydrophilic monomer**

Significantly different results from those using hydrophobic monomers are obtained when more hydrophilic monomers are applied. N,N'-methylenebisacrylamide (MBAm) is a water-soluble divinyl monomer which has been used in a recent novel process to polymerize protein crystals, filling the space between crystal unit cells, creating a flexible, integrated polymer network from a protein crystal template.<sup>45</sup> We find here that MBAm can be polymerized in cubosomes and hexosomes in a similar way. After soaking precursor particles in monomer solution, the MBAm diffuses into the water channels inside the bicontinuous structure of the cubosome particles without affecting their shape, while the PI is simultaneously localized in the bicontinuous hydrophobic domains. Photopolymerization then occurs inside the particle during UV exposure, transforming self-assembled liquid crystalline structures into strongly

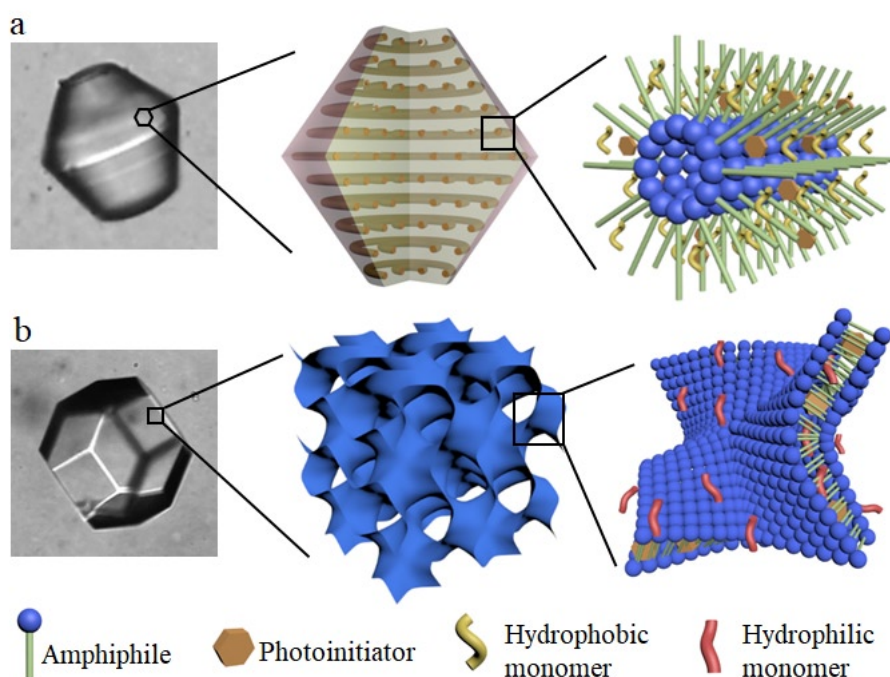


**Figure 4.5:** Schematic of the molecular arrangement of hexosome (a) and cubosome (b) with incorporated photoinitiator and monomers before polymerization. Molecules are not drawn to scale.

bonded soft polymer networks, preserving the shape of precursor particle as shown in Figure 4.5.

Figure 4.6a and c show that after polymerization, particles retain the same polyhedral shape as the precursor cubosomes. After washing away the monoolein template, the particle shape remains unchanged (Figure 4.6b and d). Significantly different from the hydrophobic monomers, however, polymerization does not darken the particle much, and after removing template, the polymeric cubosome hydrogels remain completely transparent with all of their facets visible. Certain levels of monomer concentration are needed here for optimal results. In Figure B.8, at lower concentrations of MBAm, cubosomes are only partially polymerized, with incomplete structures remaining after removal of the lipid template. At a higher MBAm concentration of 2.4%, polymeric cubosomes are obtained in Figure 4.6e that appear identical to

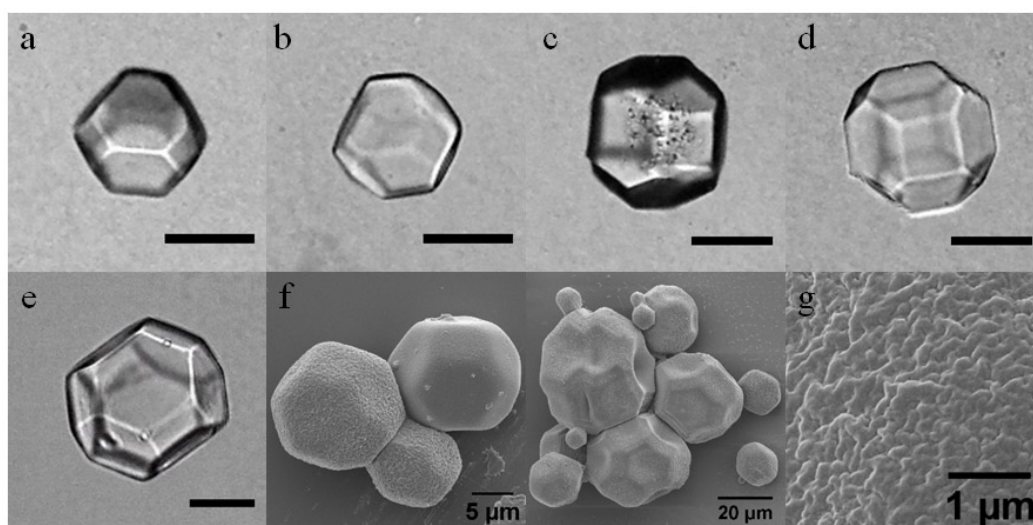


**Figure 4.6:** Polymerized cubosomes using MBAm as monomer. (a-d) Polymerized cubosomes before (a and c) and after (b and d) removing the template, concentration of MBAm in continuous phase  $c_{\text{MBAm}} = 1.6\%$ ; microscopy (e) and SEM micrographs (f and g) of polymeric cubosomes after removing template,  $c_{\text{MBAm}} = 2.4\%$ , scale bar of (e) is  $50\ \mu\text{m}$ , and (g) is a zoomed image of the particle surface. For all the particles, mass ratio of PI to monoolein  $m_{\text{PI}} : m_{\text{monoolein}} = 0.04$ .

their soft liquid crystalline templates. SEM observations in Figure 4.6f confirm the polyhedral shape of the solid cubosomes and highlight the more uniform surface topography of these structures (Figure 4.6g), different from the polymer spheres of polymeric particles from hydrophobic monomers.

Hydrophilic monomers and cross-linkers are polymerized into swollen cross-linked polymer networks, forming hydrogels. Hydrogels are not soluble but can trap solvent, and are deformable and elastic in structure, exhibiting viscoelastic properties. Polymerization of MBAm and similar monomers is commonly used to make hydrogels with desirable soft mechanical properties.<sup>46–48</sup> In this work, we produce hydrogel particles with polyhedral shapes that still possess desirable hydrogel elasticity. Measuring particle sizes with and without solvent we see these polymeric cubosomes have an estimated swelling ratio of 30%. Figure 4.7 demonstrates that the polymeric polyhedra formed from MBAm are highly elastic, as they can be deformed

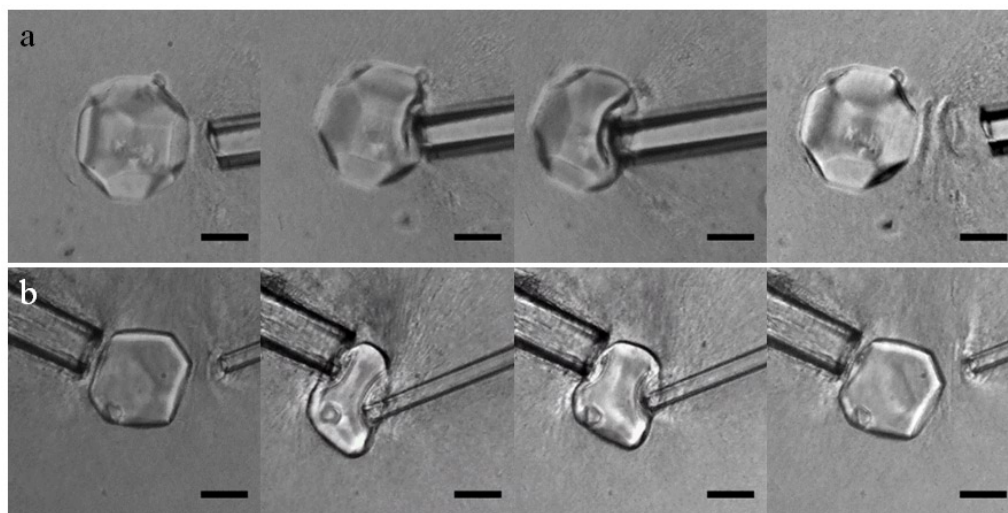


**Figure 4.7:** Deformation and recovery in the truncated octahedron shape of polymeric cubosomes, (a and b) are both frames from videos, images from left to right are in the order of time,  $c_{\text{MBAm}} = 1.6\%$ , mass ratio of PI to monoolein is  $m_{\text{PI}} : m_{\text{monoolein}} = 0.04$ . Scale bar is  $50 \mu\text{m}$ .

by microcapillary pressure with a strain as high as 40% and still completely recover their original shapes once the external force is removed. The hydrogel polyhedra contain a significant amount of solvent, leaving the particles somewhat indented following drying. The SEM images in Figure 4.6f show dried hydrogel polyhedra particles larger than  $30 \mu\text{m}$  exhibiting collapsed and indented facets as a result of solvent removal.

Particles can be polymerized in a wide range of sizes. From optical microscopy observations, cubosomes that range from  $10$  to  $150 \mu\text{m}$  in size can be polymerized while preserving the polyhedral shapes (Figure B.9). SEM micrographs in Figure 4.8 show the polymerized polyhedral cubosomes at smaller length scales,  $40 \mu\text{m}$  to  $500 \text{nm}$ . With decreasing size, the microstructure is looser and less uniform, and drying has more of an effect on stability. This method seems to have a lower particle size limit. Below about  $5 \mu\text{m}$ , polymerization is less effective in preserving shapes compared with larger particles. The reason could be diffusion of PI during the



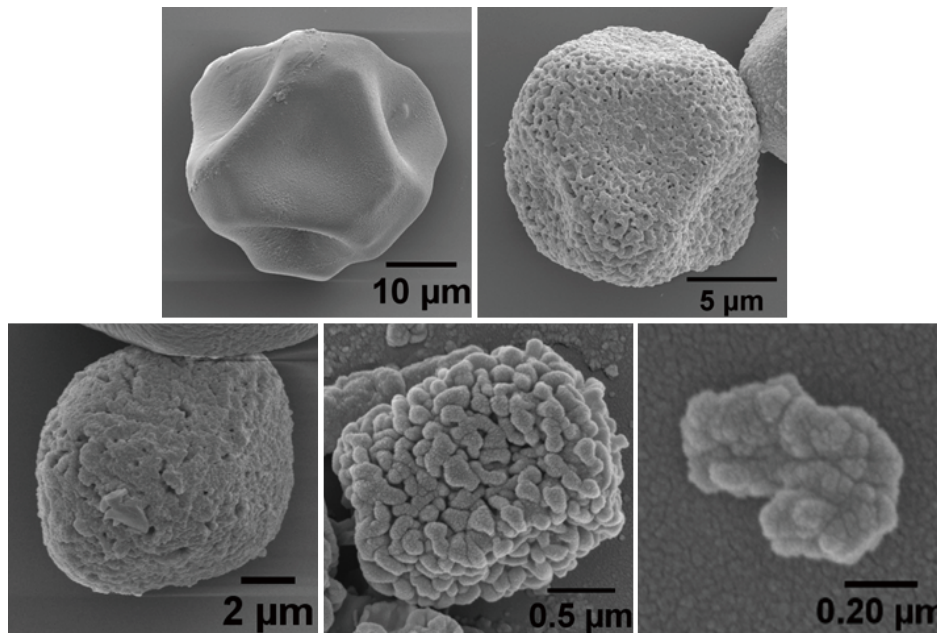
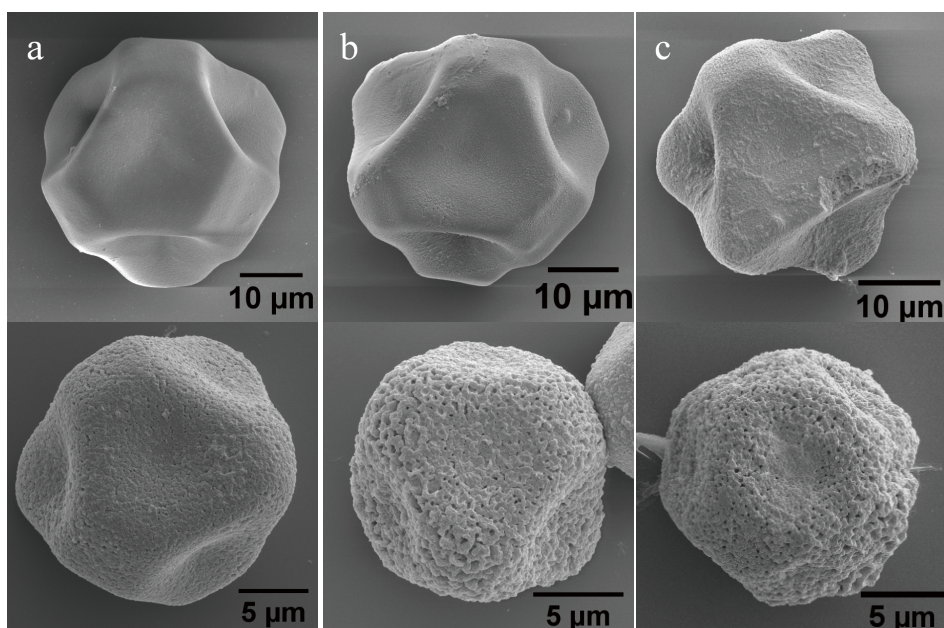


**Figure 4.8:** SEM micrographs of polymeric cubosomes in different sizes from 35  $\mu\text{m}$  to 500 nm.  $c_{\text{MBAm}} = 1.6\%$ , mass ratio of PI to monoolein  $m_{\text{PI}} : m_{\text{monoolein}} = 0.04$ .

evaporation process, as well as uncontrollability of the free radical polymerization, which has stronger effects at smaller length scales.

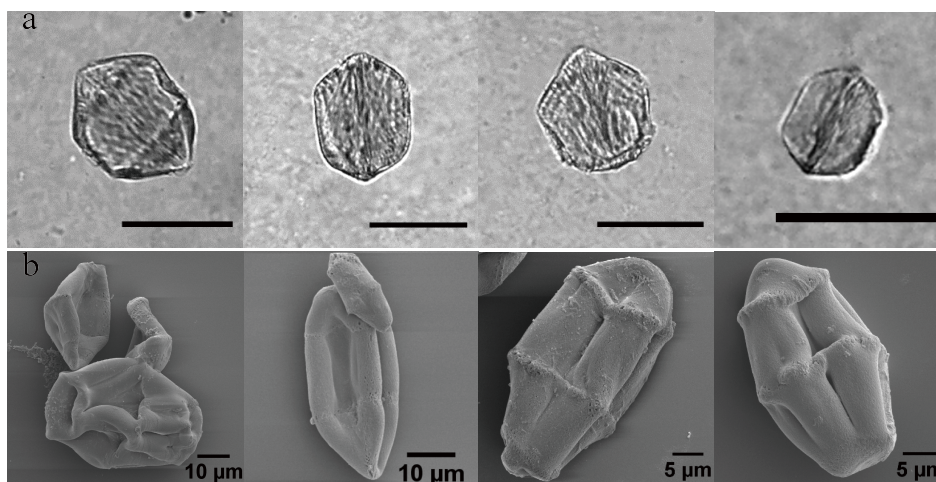
The crosslinked polymer network structure can also be adjusted by monomer concentrations. As shown in the top images of Figure 4.9a-c, the microstructure of polymeric cubosomes becomes more porous with decreasing monomer concentration for precursor particles of the same size, 40  $\mu\text{m}$ . At a different size (15  $\mu\text{m}$  in bottom row of Figure 4.9), particles polymerized from a higher monomer concentration have a denser cross-linked polymer network. This could be a way to control particle elasticity, as higher monomer concentrations should form stiffer particles.

Figure 4.10 shows hexosomes polymerized from MBAm. Because MBAm is hydrophilic, the additional hydrophobic additive hexadecane is used to form the hexagonal phase liquid crystal.<sup>11</sup> The preparation of hexosomes is different from that of cubosomes. Cubosomes are prepared by contacting them with monomer so-



**Figure 4.9:** SEM micrographs of polymeric cubosomes from monomer concentrations  $c_{\text{MBAm}} = 2.4\%$  (a),  $1.6\%$  (b), and  $0.8\%$  (c), mass ratio of PI to monoolein  $m_{\text{PI}} : m_{\text{monoolein}} = 0.04$ .

lution before polymerization to let MBAm diffuse inside the particles. However, before hexosome templates form, MBAm is added in the dilution solution for making droplet precursors. The formed hexosomes contain both monomer and PI, so they can be polymerized directly, and diffusion-based loading of MBAm is not needed. Hexosomes are polymerized better in this way than the cubosome method, as the microstructure of closed micellar cylinders impedes the diffusion of hydrophilic MBAm inside particles. As in Figure 4.10a, MBAm polymerization preserves the spinning-top and biconical shapes of hexosome precursors after removal of the monoolein template. The polymeric hexosomes produced from MBAm are not as transparent as the MBAm cubosomes, with linear wrinkles visible in the particles in Figure 4.10a. From SEM, polymeric hexosomes collapsed more than cubosomes, and the structure indicates probably only a polymerized shell is obtained. While cubosomes with a wide range of sizes can be polymerized from MBAm, hexosome



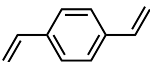
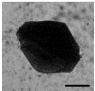
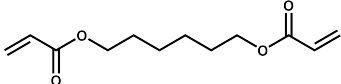
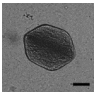
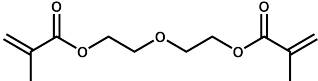
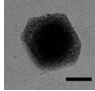
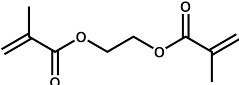
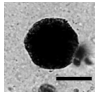
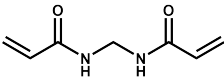
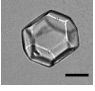

**Figure 4.10:** Microscopy (a) and SEM micrographs (b) of polymeric hexosomes after removing template, hexadecane is the hydrophobic additive with a mass ratio  $m_{\text{monoolein}} : m_{\text{hexadecane}} = 1 : 0.2$ , and MBAm is the monomer with the concentration  $c_{\text{MBAm}} = 1.6\%$ , mass ratio of PI to monoolein is  $m_{\text{PI}} : m_{\text{monoolein}} = 0.06$ . Scale bar is  $50 \mu\text{m}$ .

solids are only produced stably below a length scale of  $50 \mu\text{m}$ , with larger ones only partially polymerizing (Figure B.10a). The polymerization of hexosomes also requires a higher ratio of PI to monoolein ( $m_{\text{PI}} : m_{\text{monoolein}} = 0.06$ ) than cubosomes ( $m_{\text{PI}} : m_{\text{monoolein}} = 0.04$ ). When a ratio of 0.04 is used, hexosome precursors cannot be polymerized completely and only pieces are obtained after washing with ethanol (Figure B.10b). As hexosomes have a larger hydrophobic domain, they accommodate less hydrophilic monomer inside, which is not enough to preserve the whole structure as well.

The molecular structures of all the monomers used in this work, and the polymeric particles formed from each, are listed in Table 1. This work demonstrates the compatibility of this method with a range of different monomers for two distinct liquid crystalline particulate forms and a number of additional shapes. Comparing morphologies of polymeric particles, their precursors and monomers, significant differences in polymerization are found depending on the liquid crystalline mi-

crostructure of the precursors.<sup>28,32</sup> Hexosomes have a more hydrophobic internal environment as they are composed of closed micellar cylinders, and these accommodate hydrophobic monomers in the larger space between their hydrocarbon chains (Figure 4.5a). Cubosomes, however, have bicontinuous water channels that interpenetrate a larger volume of hydrophilic domain, so hydrophilic monomers are mainly dissolved in water channels and a small amount can enter the palisade layer of curved bilayer (Figure 4.5b). In this method, hydrophobic PI is localized in the hydrophobic domain in both precursors, while monomers can be solubilized in different regions according to their hydrophobicity. For hydrophobic monomers, they are accommodated more in hexosomes than cubosomes, so a relatively more loose and porous microstructure forms in polymeric cubosomes than hexosomes, as observed in Figure 4.2, 4.4, B.6, and B.7. Using hydrophilic monomers, the situation is reversed, as the monomers can diffuse inside cubosomes much faster than into hexosomes, and cubosomes can accommodate more hydrophilic monomers than hexosomes because of the less hydrophobic chemical environment. As a result, polymerization of cubosomes occurs in a larger range of particle sizes with a smaller concentration of PI as in comparisons of Figure 4.6, 4.8, 4.10, B.9, and B.10. In addition, the bicontinuous microstructure of cubosomes provides a larger surface for the reaction of hydrophilic monomer and hydrophobic PI, while in hexosomes the hydrophilic monomer is enclosed in the micellar cylinders and the monomer is more segregated from the PI. Therefore polymerization in particles varies with different phases, as reported in previous works,<sup>28</sup> and the shape preservation of liquid crystalline particles needs different monomers depending on the native microstructures.

**Table 4.1:** Molecular structures of monomers and the polymeric particles, scale bar is 50  $\mu\text{m}$ .

Monomer (cross-linker)	Molecular structure	Polymeric particle
Divinylbenzene (DVB)		 Hexosome (hard)
1,6-Hexanediol diacrylate (HDDA)		 Hexosome (hard)
Di(ethylene glycol) dimethacrylate (DEGDMA)		 Cubosome (hard)
Ethylene glycol dimethacrylate (EGDMA)		 Cubosome (hard)
N,N'-methylenebisacrylamide (MBAm)		 Cubosome (soft)
		 Hexosome (soft)

## 4.4 Conclusions

Despite broad research activity in the areas of cubosome and hexosome production, their applications have historically been limited to conditions where their liquid crystalline state remained stable or is formed under desirable conditions.<sup>49</sup> In this chapter we show how to broadly extend the production of uniquely shaped colloids by polymerization of both hexosomes and cubosomes. This method demonstrates compatibility with a range of monomers with different properties. The monomers with larger hydrophobicity, DVB and HDDA, induce the formation of hexosomes,

while the less hydrophobic monomers DEGDMA and EGDMA form cubosomes with aqueous monoolein. The hydrophilic monomer MBAm can diffuse inside cubosomes and hexosomes without affecting particle shapes. The shapes of these two types of particles, before polymerization, depend on the liquid crystalline phase and microstructure: hexosomes are biconical, and cubosomes are polyhedral. The shapes of polymerized particles are controlled by the initial shapes of the liquid crystalline templates. Whether hard or deformable particles are obtained depends on the choice of monomer. Hydrophobic monomers form hard particles, while hydrophilic monomers form elastic hydrogel particles, all preserving the original shape and symmetry of the liquid crystalline precursors. The approach developed in this chapter is useful for synthesis of polymer microparticles of a variety of shapes, with different degrees of curvature and faceting, and a wide range of elasticities. The work broadens our ability to control colloid shape and will enable expanded studies of shape effects on flow, cell uptake and self-assembly.

## 4.5 References

- [1] E. Lutton, *Journal of the American Oil Chemists Society* **1965**, *42*, 1068–1070.
- [2] J. M. Seddon, *Biochimica et Biophysica Acta (BBA)-Reviews on Biomembranes* **1990**, *1031*, 1–69.
- [3] G. L. Robert, *The aqueous phase behavior of surfactants*, **1996**.
- [4] J. Gustafsson, H. Ljusberg-Wahren, M. Almgren, K. Larsson, *Langmuir* **1997**, *13*, 6964–6971.
- [5] C. Neto, G. Aloisi, P. Baglioni, K. Larsson, *The Journal of Physical Chemistry B* **1999**, *103*, 3896–3899.
- [6] X. Mulet, B. J. Boyd, C. J. Drummond, *Journal of colloid and interface science* **2013**, *393*, 1–20.
- [7] C. E. Conn, C. J. Drummond, *Soft Matter* **2013**, *9*, 3449–3464.

- 
- [8] J. Gustafsson, H. Ljusberg-Wahren, M. Almgren, K. Larsson, *Langmuir* **1996**, *12*, 4611–4613.
- [9] B. J. Boyd, S. B. Rizwan, Y.-D. Dong, S. Hook, T. Rades, *Langmuir* **2007**, *23*, 12461–12464.
- [10] H. Wang, P. B. Zetterlund, C. Boyer, B. J. Boyd, S. W. Prescott, P. T. Spicer, *Soft matter* **2017**, *13*, 8492–8501.
- [11] H. Wang, P. B. Zetterlund, C. Boyer, B. J. Boyd, T. J. Atherton, P. T. Spicer, *Langmuir* **2018**, *34*, 13662–13671.
- [12] C. M. Doherty, R. A. Caruso, B. M. Smarsly, P. Adelhelm, C. J. Drummond, *Chemistry of materials* **2009**, *21*, 5300–5306.
- [13] C. K. Nguyen, H. G. Cha, Y. S. Kang, *Crystal Growth & Design* **2011**, *11*, 3947–3953.
- [14] P. F. Damasceno, M. Engel, S. C. Glotzer, *Science* **2012**, *337*, 453–457.
- [15] Y. Lu, R. Ganguli, C. A. Drewien, M. T. Anderson, C. J. Brinker, W. Gong, Y. Guo, H. Soye, B. Dunn, M. H. Huang *et al.*, *Nature* **1997**, *389*, 364.
- [16] C. J. Brinker, Y. Lu, A. Sellinger, H. Fan, *Advanced materials* **1999**, *11*, 579–585.
- [17] C. Kresge, M. Leonowicz, W. J. Roth, J. Vartuli, J. Beck, *nature* **1992**, *359*, 710.
- [18] H. Yang, N. Coombs, G. A. Ozin, *Nature* **1997**, *386*, 692.
- [19] N. J. Carroll, S. B. Rathod, E. Derbins, S. Mendez, D. A. Weitz, D. N. Petsev, *Langmuir* **2008**, *24*, 658–661.
- [20] S. Marre, K. F. Jensen, *Chemical Society Reviews* **2010**, *39*, 1183–1202.
- [21] F. Zhang, D. Gu, T. Yu, F. Zhang, S. Xie, L. Zhang, Y. Deng, Y. Wan, B. Tu, D. Zhao, *Journal of the American Chemical Society* **2007**, *129*, 7746–7747.
- [22] D. Gu, H. Bongard, Y. Meng, K. Miyasaka, O. Terasaki, F. Zhang, Y. Deng, Z. Wu, D. Feng, Y. Fang *et al.*, *Chemistry of Materials* **2010**, *22*, 4828–4833.
- [23] J. D. Morgan, C. A. Johnson, E. W. Kaler, *Langmuir* **1997**, *13*, 6447–6451.
- [24] C. McKelvey, E. Kaler, J. Zasadzinski, B. Coldren, H.-T. Jung, *Langmuir* **2000**, *16*, 8285–8290.
- [25] S. Dong, P. T. Spicer, F. P. Lucien, P. B. Zetterlund, *Soft matter* **2015**, *11*, 8613–8620.

## References

---

- [26] I. Lesov, Z. Valkova, E. Vassileva, G. S. Georgiev, K. Ruseva, M. Simeonov, S. Tcholakova, N. D. Denkov, S. K. Smoukov, *Macromolecules* **2018**, *51*, 7456–7462.
- [27] D. Yang, D. F. O'Brien, S. R. Marder, *Journal of the American Chemical Society* **2002**, *124*, 13388–13389.
- [28] K. S. Worthington, C. Baguenard, B. S. Forney, C. A. Guymon, *Journal of Polymer Science Part B: Polymer Physics* **2017**, *55*, 471–489.
- [29] M. A. DePierro, C. A. Guymon, *Macromolecules* **2014**, *47*, 5728–5738.
- [30] S. Peng, P. G. Hartley, T. C. Hughes, Q. Guo, *Soft Matter* **2015**, *11*, 6318–6326.
- [31] D. L. Gin, W. Gu, B. A. Pindzola, W.-J. Zhou, *Accounts of Chemical Research* **2001**, *34*, 973–980.
- [32] J. Clapper, C. Guymon, *Advanced Materials* **2006**, *18*, 1575–1580.
- [33] J. A. Champion, S. Mitragotri, *Proceedings of the National Academy of Sciences* **2006**, *103*, 4930–4934.
- [34] E. Hinde, K. Thammasiraphop, H. T. Duong, J. Yeow, B. Karagoz, C. Boyer, J. J. Gooding, K. Gaus, *Nature nanotechnology* **2017**, *12*, 81.
- [35] J. Zhao, M. H. Stenzel, *Polymer Chemistry* **2018**, *9*, 259–272.
- [36] J. Cui, M. Björnalm, K. Liang, C. Xu, J. P. Best, X. Zhang, F. Caruso, *Advanced Materials* **2014**, *26*, 7295–7299.
- [37] J. Cui, *Chem* **2017**, *2*, 606–607.
- [38] P. T. Spicer, K. L. Hayden, M. L. Lynch, A. Ofori-Boateng, J. L. Burns, *Langmuir* **2001**, *17*, 5748–5756.
- [39] P. T. Spicer, W. B. Small, M. L. Lynch, J. L. Burns, *Journal of Nanoparticle Research* **2002**, *4*, 297–311.
- [40] J. Jeong, Z. S. Davidson, P. J. Collings, T. C. Lubensky, A. Yodh, *Proceedings of the National Academy of Sciences* **2014**, *111*, 1742–1747.
- [41] T. Oka, N. Ohta, *Langmuir* **2016**, *32*, 7613–7620.
- [42] C. K. Ober, K. P. Lok, *Macromolecules* **1987**, *20*, 268–273.
- [43] J.-S. Song, M. A. Winnik, *Macromolecules* **2006**, *39*, 8318–8325.



- [44] S. Phan, W.-K. Fong, N. Kirby, T. Hanley, B. J. Boyd, *International Journal of Pharmaceutics* **2011**, *421*, 176 – 182.
- [45] L. Zhang, J. B. Bailey, R. H. Subramanian, F. A. Tezcan, *Nature* **2018**, *557*, 86.
- [46] J. Xu, Z. Fan, L. Duan, G. Gao, *Polym. Chem.* **2018**, *9*, 2617–2624.
- [47] T. Celik, N. Orakdogan, *Macromolecular Chemistry and Physics* **2015**, *216*, 2190–2201.
- [48] J. E. Elliott, M. Macdonald, J. Nie, C. N. Bowman, *Polymer* **2004**, *45*, 1503 – 1510.
- [49] W. K. Fong, S. Salentinig, C. A. Prestidge, R. Mezzenga, A. Hawley, B. J. Boyd, *Langmuir* **2014**, *30*, 5373–5377.



## Chapter 5

# Particle-scale studies of hexosome formation by ultrasonication

### 5.1 Introduction

Cubosomes and hexosomes are soft particles of cubic and hexagonal liquid crystalline phases, respectively, formed by self-assembled amphiphilic lipids.<sup>1,2</sup> These colloidal nanostructured dispersions have broad applications, for example as drug delivery vehicles and medical imaging agents.<sup>3-5</sup> Cubosomes and hexosomes are most often made by dispersing bulk liquid crystalline phase in the presence of colloidal stabilizers: the top-down method.<sup>6,7</sup> As bulk liquid crystalline phase is highly viscoelastic, a significant energy input process, like ultrasonication, is needed to produce nanoparticles. Despite its common application, little is known about ultrasonic dispersion of bulk cubic and hexagonal phases because the process occurs at extremely high speeds and small length scales.<sup>8</sup>

Cubosomes and hexosomes form different shapes as a result of the underlying phase symmetry and microstructure.<sup>9</sup> In a bottom-up method we developed in Chapters 2 and 3, microscale cubosomes and hexosomes were made by crystallization of lipids inside emulsion droplets via solvent removal.<sup>10,11</sup> Apart from phase, bottom-up particle shapes can also be affected by size, temperature, crystallization rate, and addition of additives, enabling some control. Nanosized cubosomes and hexosomes prepared using top-down methods can vary significantly in shape, as

wide variations in applied energy levels and durations have been used in past works. Nanoscale cubosomes are mostly cubes,<sup>2,12</sup> but hexosomes vary quite a bit in observed shape,<sup>13</sup> sometimes forming flat hexagonal prisms,<sup>14,15</sup> spheres,<sup>16,17</sup> and bicones.<sup>18</sup>

Although ultrasound is the most popular liquid crystalline dispersion method, what happens to the viscoelastic phases during high-energy ultrasonication is an open question. Previous works have only examined particles produced after ultrasonication is complete, but the specific transformations occurring during this process, and the effects of bulk fluid properties, are not known. A link between particle composition and dispersion behavior is also important to discern, as various hydrophobic molecules are used to induce hexagonal phase formation by aqueous lipids<sup>19,20</sup> to enable, for example, triggered release during lipid digestion.<sup>21,22</sup> Although simulations and structural studies of bulk hexagonal phase flow exist,<sup>23–25</sup> more information is needed to link the bulk studies to hexosome particle size, shape, and performance in multiple new envisioned applications.<sup>26,27</sup>

In this work, a systematic study of formation and evolution of hexosome shapes in an ultrasonic field is carried out. A unique ultrasonic sample cell is mounted on a microscope slide to allow high-speed imaging of the formation of hexosomes and cubosomes *in situ*.<sup>28,29</sup> Ultrasound-generated bubbles oscillate, move, and create micro-streaming flows, which break down the bulk phase and form nano- and microparticles. In this process, the bulk hexagonal phase liquefies, is broken down into droplets, then solidifies and deforms in the oscillating shear field generated by the bubbles. We use the presence of ordered particle shapes as preliminary evidence that hexosomes are not directly fragmented from bulk hexagonal phase but, instead, form from recrystallised liquefied droplets of the yielded bulk phase. Particle shapes depend on the intensity of processing and rheological properties of the bulk phase.

Phases with a lower elastic modulus can more easily yield and deform in a high-intensity field, forming more ordered shapes. This study gives a new, particle-level perspective on a much-used technique for creating liquid crystalline particles and controlling their shapes.

## 5.2 Materials and methods

Commercial grade monoolein, Dimodan MO90K, was obtained from DuPont Danisco (Botany NSW, Australia). Vitamin E ( $\alpha$ -tocopherol, 96%) and hexadecane (99%) were purchased from Sigma Aldrich (Castle Hill, NSW, Australia). Commercial Vitamin E (Blackmores, Australia) was also used and contains structural isomers, unsaturated tocotrienols, and  $\alpha$ -tocopherol.<sup>30</sup> All chemicals were used without further purification. Ultrapure water with a resistivity of 18.25  $M\Omega$ -cm was obtained using a Sartorius ultrapure water purifier. Bulk liquid crystal phases were formed by thorough mixing of monoolein, water, and additives with desired weight concentrations. All experiments were carried out at 25 °C.

Cubosome and hexosome dispersions were prepared by ultrasonication treatment of 0.5 g bulk phase in 20 g water, using a high intensity ultrasonic processor (Qsonica Q500) for 1 min, at 20%-40% of the maximum power, with 5 s pulses interrupted by 5 s breaks.

Direct observations of the ultrasonication process at the single particle scale were carried out using an ultrasonic transducer mounted on a glass microscope slide, as shown in Figure 5.1a.<sup>28,29</sup> Ultrasound waves were produced by a piezoelectric transducer with resonance frequency  $28 \pm 5$  kHz (SMPL60W5T03R, Steminc) glued on the glass slide. The driving signal was generated by a waveform generator (RS 174-557, Thurlby Thandar Instruments) and amplified by a linear, radio-frequency power amplifier (AG Series Amplifier, T&C Power Conversion Inc.). A chamber

made of PDMS, to contain the sample, was also glued on the glass slide beside the piezo. Driving frequencies in the range of 20-180 kHz were applied, which generated oscillating bubbles in the sample.<sup>28,29</sup> The generated bubbles were quite random in size and position, which didn't allow us to control their formation and behaviour in this process.

Microscope observations of particles under bright field and polarized light illumination were conducted on a Leica DM2500M optical microscope with a Moticam 10MP digital camera. Direct observations of ultrasound dispersion of hexosomes were conducted on a Motic AE31E inverted optical microscope with a Phantom V7.3 high-speed camera.

Rheological characterization of bulk liquid crystalline phases was performed using a DHR-1 rheometer (TA Instruments) using an oscillatory stress sweep at a constant frequency of 1 Hz. A cone and plate geometry was used for all measurements with a solvent trap to avoid evaporative losses.

### 5.3 Results and discussion

Microscale hexosomes are made by dispersing bulk hexagonal phase prepared by aqueous monoolein (MO) mixed with the hydrophobic additives vitamin E (vitE) and hexadecane (C16). Figure 5.1a shows the set-up of the device used for direct observations of an ultrasonic dispersion process. A piezo and a sample chamber are glued on a glass slide. When the piezo generates ultrasound, bulk liquid crystalline phase is broken down in excess water inside the adjacent sample chamber, allowing simultaneous observation of the process using an optical microscope.

Observation of the process in Figure 5.1b shows that air bubbles form inside the bulk phase by cavitation under the driving force of the acoustic field.<sup>31</sup> As cubic phase is transparent, bubbles can be observed clearly. As ultrasound is applied,

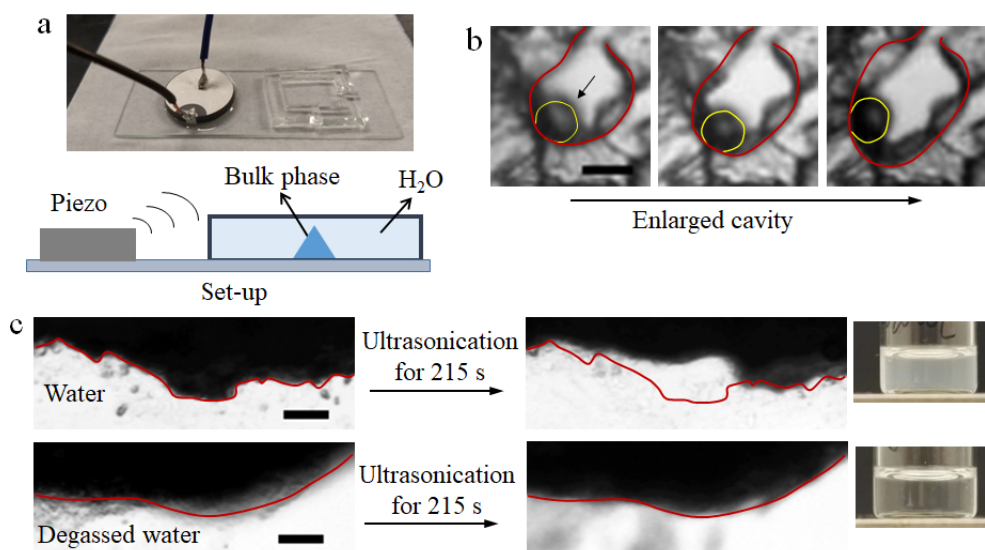


**Figure 5.1:** (a) Set-up of the device used for direct observation of ultrasonic processing; (b) microscopy images of the bulk cubic phase being broken down by ultrasound, the bubble is outlined with yellow, the cavity formed by bubble is outlined with red, and the arrow indicates the movement of the bubble, scale bar is 50  $\mu\text{m}$ ; (c) breakdown of the bulk hexagonal phase by ultrasound in degassed and normal water, and photos of particle dispersions collected after ultrasonication treatment. Cubic phase is prepared by monoolein and water, hexagonal phase contains monoolein, water, and the hydrophobic additive hexadecane at a weight ratio  $m_{\text{C16}} : m_{\text{MO}} = 0.2$ .

bubbles move around inside the bulk phase, eroding away the bulk material. The sequence of frames in Figure 5.1b shows the formation of cavities inside the solid-like cubic phase as they are enlarged by the moving bubbles, breaking down the bulk phase in the process.

Breakdown of opaque hexagonal phase is also studied with this device, as shown in Figure 5.1c. The receding interface demonstrates the erosion of bulk hexagonal phase, producing small hexosomes that cloud the surrounding water during the process. A comparison of the same process performed using degassed water demonstrates that air bubble cavitation is needed for the dispersion process to proceed. The bottom images in Figure 5.1c show that no bubbles form in the degassed water,

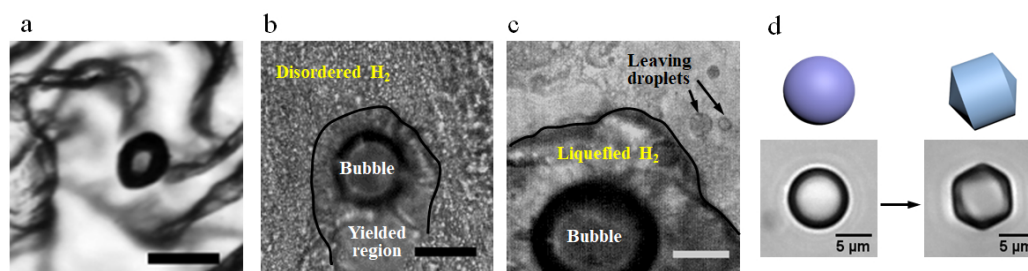


**Figure 5.2:** Illustration of ultrasonication processing and breakdown of bulk phase into particles: (a) a bubble is generated inside the bulk liquid crystal phase; (b and c) microscopy images from high-speed videos of the oscillating bubble and bulk hexagonal phase, showing the yielded and liquefied region as outlined, scale bar is 50  $\mu\text{m}$ ; (d) recrystallization of a droplet, indicating the hypothesized shape transition process occurring.

as no change is observed in the sonicated bulk phase as a result. The water phase collected after ultrasonication is clear and contains very few particles, as seen in the right bottom image.

More detailed observations of individual bubbles in the liquid crystals, using a high-speed camera, allow us to further characterize the dispersion process. As shown in Figure 5.2a, when exposed to an oscillating acoustic signal (20-180 kHz), air bubbles form inside the bulk phase and undergo alternate expansions and contractions<sup>32</sup> similar to what occurs during viscoelastic gel dispersion<sup>33</sup> and stimulated endocytotic cellular uptake of drugs.<sup>34</sup> Here we directly observe the volumetric oscillation of bubbles actually yielding, or fluidizing, the hexagonal phase around it (Figure 5.2b), in a region whose size is determined by the rate of energy dissipation in the bulk phase, Figure 5.2b. The bulk phase outside the yielded region, marked in Figure 5.2b, is still disordered hexagonal phase, as the energy intensity decays rapidly with distance from the bubble. The curved interface of the yielded bulk phase in Figure 5.2c indicates that the region is liquid and interfacial tension dominates over elasticity. In videos we see that the bulk phase is liquefied and undulates rapidly with the highly dynamic deformation of the bubble. The yielded bulk phase is seen to



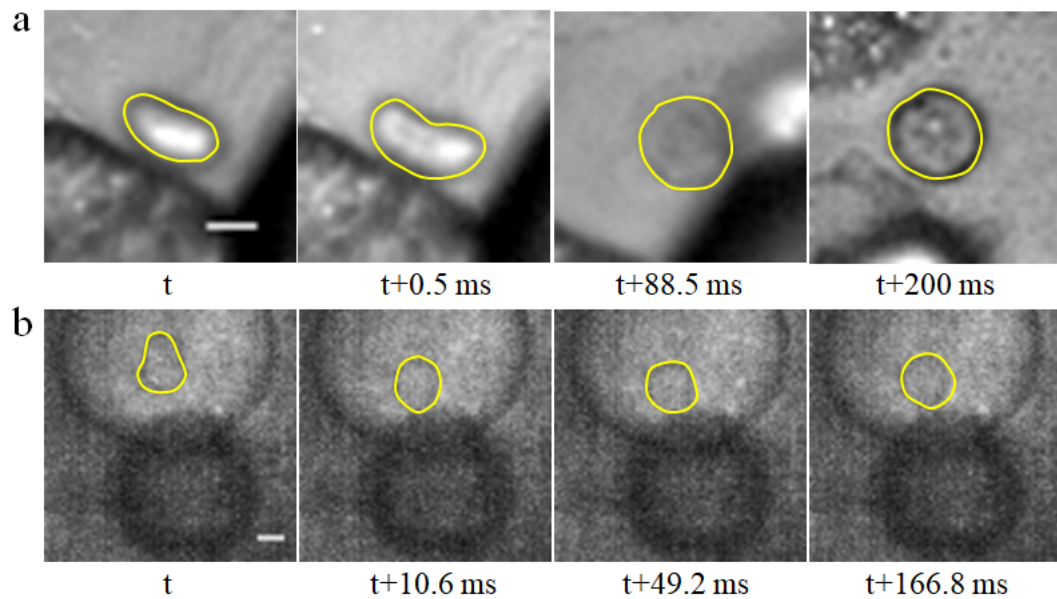


**Figure 5.3:** Microscopy images from high-speed videos of deformation of single hexosome particle by oscillating bubble. Particle shapes are outlined with yellow, vitamin E is the hydrophobic additive with the weight ratio  $m_{\text{vitE}} : m_{\text{monoolein}} = 0.27$ , scale bar is 10  $\mu\text{m}$ .

be broken down into droplets, which then flow with the micro-streams generated by the oscillating bubble<sup>34</sup> in the water phase, driving them away from the yielded region. Away from the bubble, we expect the droplets to relax and recrystallize into hexosomes (Figure 5.2d).

The high speed camera also allows us to capture interactions between the oscillating bubble and individual particles created by the dispersion process described above. Figure 5.3 shows two sequences of frames of a liquefied droplet that became trapped at the bubble surface while leaving the bulk phase. The droplet undulates in the oscillating field, indicating the intensity of the field and the deformation experienced by the droplets after dispersion, similar to vesicles trapped in a similar state.<sup>35,36</sup> Figure 5.3a shows a particle that is stretched into an elongated ellipsoid and then back to a rounded shape by the energy field. In Figure 5.3b we see a particle in the cavity of the bulk phase near a bubble. The initial shape in the observation

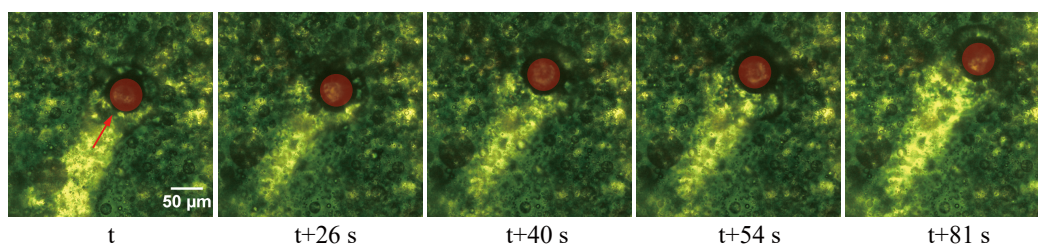


**Figure 5.4:** Microscopy observation under polarized light of the bulk hexagonal phase when an oscillating bubble going through driven by ultrasound, the bubble is coloured red to make it more visible, the arrow points to the moving bubble, vitamin E is the hydrophobic additive with the weight ratio  $m_{\text{vitE}} : m_{\text{monoolein}} = 0.2$ .

resembles partially coalesced particles, possibly two separate ones several milliseconds before. As the ultrasound affects the particle, its shape becomes more rounded, and the irregular shape fuses into a more compact form. Although the resolution at this frame rate is limited, the shape transition for the single particle is clearly observed, demonstrating the types of changes occurring in such an ultrasound process. Only after leaving the intense energy region can the droplets relax into spheres and, presumably, recrystallize into hexosomes.

In hexagonal phase, birefringence textures can reflect certain molecular packing and defects of microstructure.<sup>37</sup> For example, a symmetric pattern is typically observed in mono-domain phases with a microstructure of ringed cylinders, and a bright birefringence with a stripe pattern appears when straight cylinders are arranged in parallel.<sup>11,38</sup> The bulk hexagonal phase made by simply mixing aqueous monoolein and vitamin E has weak birefringence, as the phase is multi-domain without uniform arrangement of the underlying cylindrical micelles. After an oscillating bubble moves through such a relatively disordered phase, however, the birefringence becomes brighter in the area yielded by the bubble, showing the trajectory of the bubble quite clearly in Figure 5.4. When yielded, the bulk phase doesn't lose birefringence, which means the yielded and liquefied material is still in the hexagonal phase

and oscillation does not necessarily break the self-assembled system into unstructured droplets. The change of birefringence indicates microstructural reorientation occurs as a result of deformation, producing a more ordered packing after yielding by ultrasound.

Both simulation and experimental results show that flow can reorient fluid microstructure in hexagonal phase.<sup>23-25</sup> Hexagonal phase is composed of hexagonally packed cylindrical micelles with a distance of several nanometers between them.<sup>38</sup> The bulk hexagonal phase is normally a multi-domain space, with the cylinders packed in varying directions. Simulation<sup>23,39</sup>, rheology, and SAXS<sup>24,25,40</sup> measurements show that for certain deformation rates, the cylindrical micelles can align in the same direction. In an ultrasound process, the shear applied to the bulk hexagonal phase by oscillating bubbles can also cause a shear-induced microstructural reorientation. Microscopic observations indicate that bulk hexagonal phase made by mixing has colorful birefringence, which indicates the system has multiple domains without strong ordering. Reorientation occurs in the yielded phase by bubble oscillation, and the liquefied phase is broken down into droplets. The formation of hexosomes from the yielded droplets is thus a recrystallization, as cylindrical micelles reorient and finally align while forming their final shape.<sup>11</sup> In ultrasound process, bubble size and frequency are not observed to directly affect formation of particles. Although oscillation of bubbles is related to size and ultrasound frequency, the shear caused by bubble oscillation is the main reason for breaking down the bulk phase and producing shaped particles. As a result, hexosomes with biconical shapes can form in a wide range of ultrasound frequencies and oscillating bubble sizes. From the observations made here, we speculate that liquid crystalline particles with specific shapes made by the top-down process are not fragments of the bulk liquid crystalline phase, but are liquefied, dispersed, and recrystallized particles with

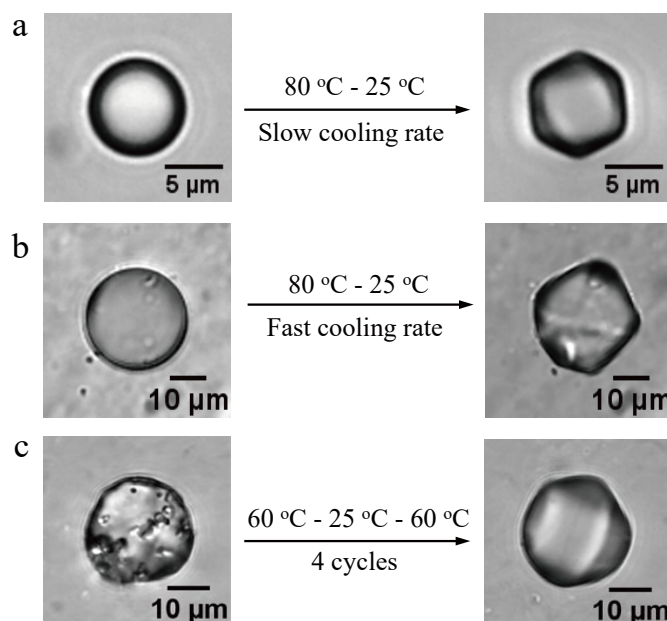


**Figure 5.5:** Microscopy images of hexosome shape transitions under different conditions of temperature change. Vitamin E is the hydrophobic additive with a weight ratio  $m_{\text{vitE}} : m_{\text{monoolein}} = 0.2$ .

highly ordered single-domain microstructures identical to those we previously made from emulsion droplet precursors.<sup>11</sup> Given this, we perform a comparison with more explicitly recrystallized samples to determine the significance of thermal effects on order in the larger hexosomes.

Heat is generated in an ultrasound process, and the effect of temperature change on particle shapes is expected. As Figure 5.5a and b show, after heating up to about 80 °C, hexosomes melt into a spherical oil droplet. Slowly cooling to 25 °C, a biconical shape reforms (Figure 5.5a). However, as cooling rate is increased, the hexosome formed is somewhat less ordered (Figure 5.5b). The results indicate that there may be limiting rates of relaxation in the hexosomes that can affect whether single-domain structures are able to form before the rheology of the material locks in a given shape. Similar to the case for solid crystals, refinement of the particle shape is often possible by cycled temperature steps, even when below the melting temperature,

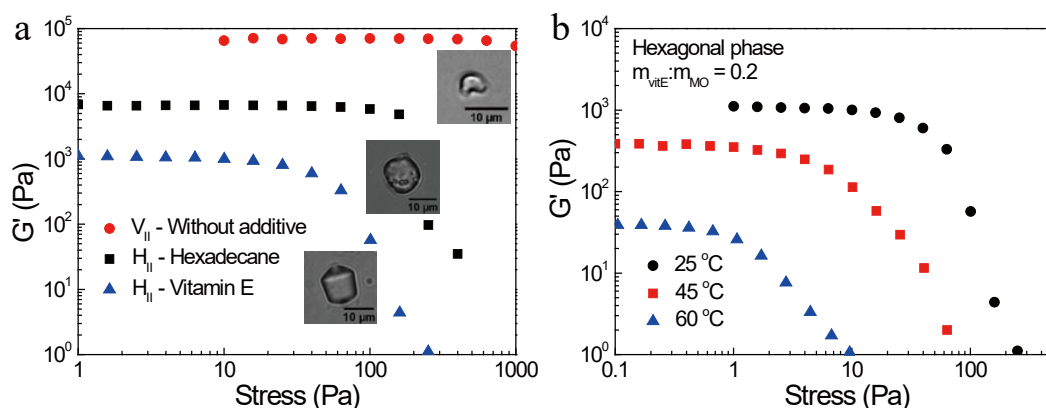


**Figure 5.6:** Elastic modulus  $G'$  of bulk liquid crystal phases: (a) cubic phase formed of monoolein, hexagonal phases of monoolein with addition of hexadecane and vitamin E at weight ratio  $m_{\text{additive}}:m_{\text{monoolein}} = 0.2$  at 25 °C, insets are dispersed particles of the bulk phase with corresponding composition; (b) hexagonal phase with vitamin E as additive at weight ratio  $m_{\text{vitE}} : m_{\text{monoolein}} = 0.2$  at different temperatures.

80 °C, of the system. As Figure 5.5c shows, a poorly-ordered hexosome initial state can transform to a single-domain biconical shape after four cycles of heating to 60 °C and cooling back to 25 °C. It is plausible that particles in a typical ultrasonic dispersion process undergo similar temperature cycling and refinement prior to further study and imaging, resulting in a similar degree of shape uniformity. The rheology of the hexagonal phase is central to determining the material relaxation rate and its response to applied energy, so we measure the bulk material elasticity in order to compare effects of the particle phase and composition on its mechanical properties.

The rheology of three different bulk liquid crystalline phases in a shear flow is determined by an oscillatory stress sweep, as shown in Figure 5.6.  $G'$  is the bulk elastic modulus, which indicates the elasticity of the material and how difficult it is to deform. In Figure 5.6, all three materials exhibit a relatively constant modulus value, albeit of different magnitudes, as the applied stress is gradually increased. At a critical value of the applied stress, however,  $G'$  drops significantly as the structure yields

and begins to flow, identical to the behavior observed in Figures 5.2. In Figure 5.6a, cubic phase has the highest elasticity, more than one order of magnitude higher than a hexagonal phase with hexadecane, with the vitamin E hexagonal phase an order of magnitude lower than that. The two most elastic phases form random-shaped particles when dispersed by high intensity ultrasonic processor, as indicated by the inset images in Figure 5.6a. The least elastic phase, hexagonal phase with vitamin E, forms the most ordered particle shape using the same dispersion method and level of energy input as it has the least resistance to deformation and will relax more rapidly as well. Temperature also impacts the liquid crystal rheology with vitamin E, as we see in Figure 5.6b. The  $G'$  decreases significantly with increased temperature, dropping from a near-solid to a near-flowable fluid when changed from 25 °C to 60 °C. The temperature effect in Figure 5.6b is consistent with the effects of heating and cooling cycles on ordered shape formation seen in Figure 5.5. Dispersion processes can be improved or optimized by comparing the magnitude of the applied energy relative to the magnitude of the resistance to dispersion offered by the liquid crystal elasticity. Similarly, the choice of additives to the bulk phase, as well as process temperature, can be used to tailor the mechanical properties and response to a given process.

## 5.4 Conclusions

The process of breaking down a bulk hexagonal liquid crystalline phase by ultrasonic dispersion is observed at extremely short time scales in this work using high-speed imaging. The top-down method is the most common approach to make dispersed particles of liquid crystals, cubosomes and hexosomes, but there is no clear guide to developing such a process without trial and error or over-design in order to achieve the desired size and shape of particles. A unique sample cell is developed, enabling

us to directly observe the process of bulk hexagonal phase breaking down into hexosomes in an ultrasonic field. Dispersion occurs as oscillating gas bubbles yield the surrounding liquid crystal phase, after which the liquefied region is dispersed into droplets. Shaped liquid crystalline particles then form by recrystallization of the dispersed droplets. The viscoelastic rheology of the liquid crystal is measured and shown to be adjustable over orders of magnitude by additive choice and process temperature, resulting in various responses to the applied ultrasonic energy as well as formation of different shapes with varying quality. Our observations explain the observed variations in particle shapes, and indicate that hexosomes produced by sonication are not the result of direct fragmentation but instead a process of liquefaction, dispersion, and refinement via recrystallization.

## 5.5 References

- [1] C. Fong, T. Le, C. J. Drummond, *Chemical Society Reviews* **2012**, *41*, 1297–1322.
- [2] H. M. Barriga, M. N. Holme, M. M. Stevens, *Angewandte Chemie International Edition* **2019**, *58*, 2958–2978.
- [3] A. Yaghmur, O. Glatter, *Advances in colloid and interface science* **2009**, *147*, 333–342.
- [4] A. Zabara, R. Mezzenga, *Journal of Controlled Release* **2014**, *188*, 31–43.
- [5] J. P. Lagerwall, G. Scalia, *Current Applied Physics* **2012**, *12*, 1387–1412.
- [6] J. Gustafsson, H. Ljusberg-Wahren, M. Almgren, K. Larsson, *Langmuir* **1996**, *12*, 4611–4613.
- [7] J. Gustafsson, H. Ljusberg-Wahren, M. Almgren, K. Larsson, *Langmuir* **1997**, *13*, 6964–6971.
- [8] J. Barauskas, M. Johnsson, F. Joabsson, F. Tiberg, *Langmuir* **2005**, *21*, 2569–2577.
- [9] X. Mulet, B. J. Boyd, C. J. Drummond, *Journal of colloid and interface science* **2013**, *393*, 1–20.

## References

---

- [10] H. Wang, P. B. Zetterlund, C. Boyer, B. J. Boyd, S. W. Prescott, P. T. Spicer, *Soft matter* **2017**, *13*, 8492–8501.
- [11] H. Wang, P. B. Zetterlund, C. Boyer, B. J. Boyd, T. J. Atherton, P. T. Spicer, *Langmuir* **2018**, *34*, 13662–13671.
- [12] J. Zhai, L. Waddington, T. J. Wooster, M.-I. Aguilar, B. J. Boyd, *Langmuir* **2011**, *27*, 14757–14766.
- [13] L. Sagalowicz, M. Michel, M. Adrian, P. Frossard, M. Rouvet, H. J. Watzke, A. Yagmur, L. De Campo, O. Glatter, M. E. Leser, *Journal of microscopy* **2006**, *221*, 110–121.
- [14] M. Johnsson, Y. Lam, J. Barauskas, F. Tiberg, *Langmuir* **2005**, *21*, 5159–5165.
- [15] N. Tran, X. Mulet, A. M. Hawley, C. Fong, J. Zhai, T. C. Le, J. Ratcliffe, C. J. Drummond, *Langmuir* **2018**, *34*, 2764–2773.
- [16] I. Amar-Yuli, E. Wachtel, E. B. Shoshan, D. Danino, A. Aserin, N. Garti, *Langmuir* **2007**, *23*, 3637–3645.
- [17] L. Sagalowicz, S. Guillot, S. Acquistapace, B. Schmitt, M. Maurer, A. Yagmur, L. De Campo, M. Rouvet, M. Leser, O. Glatter, *Langmuir* **2013**, *29*, 8222–8232.
- [18] B. J. Boyd, S. B. Rizwan, Y.-D. Dong, S. Hook, T. Rades, *Langmuir* **2007**, *23*, 12461–12464.
- [19] F. Caboi, G. S. Amico, P. Pitzalis, M. Monduzzi, T. Nylander, K. Larsson, *Chemistry and physics of lipids* **2001**, *109*, 47–62.
- [20] A. Yagmur, L. de Campo, L. Sagalowicz, M. E. Leser, O. Glatter, *Langmuir* **2005**, *21*, 569–577.
- [21] W. K. Fong, S. Salentinig, C. A. Prestidge, R. Mezzenga, A. Hawley, B. J. Boyd, *Langmuir* **2014**, *30*, 5373–5377.
- [22] L. Hong, S. Salentinig, A. Hawley, B. J. Boyd, *Langmuir* **2015**, *31*, 6933–6941.
- [23] K. Luo, Y. Yang, *Polymer* **2004**, *45*, 6745 – 6751.
- [24] M. Singh, V. Agarwal, D. De Kee, G. McPherson, V. John, A. Bose, *Langmuir* **2004**, *20*, 5693–5702.
- [25] W. Richtering, J. Laeuger, R. Linemann, *Langmuir* **1994**, *10*, 4374–4379.



- 
- [26] X. Gong, M. J. Moghaddam, S. M. Sagnella, C. E. Conn, S. J. Danon, L. J. Waddington, C. J. Drummond, *ACS Applied Materials & Interfaces* **2011**, *3*, 1552–1561.
- [27] B. J. Boyd, D. V. Whittaker, S.-M. Khoo, G. Davey, *International Journal of Pharmaceutics* **2006**, *318*, 154 – 162.
- [28] V. Poulichet, V. Garbin, *Proceedings of the National Academy of Sciences* **2015**, *112*, 5932–5937.
- [29] V. Poulichet, A. Huerre, V. Garbin, *Soft Matter* **2017**, *13*, 125–133.
- [30] P. Salo-Väänänen, V. Ollilainen, P. Mattila, K. Lehikoinen, E. Salmela-Mölsä, V. Piironen, *Food Chemistry* **2000**, *71*, 535–543.
- [31] A. Delalande, S. Kotopoulis, M. Postema, P. Midoux, C. Pichon, *Gene* **2013**, *525*, 191–199.
- [32] M. Postema, A. Van Wamel, C. T. Lancée, N. De Jong, *Ultrasound in medicine & biology* **2004**, *30*, 827–840.
- [33] A. Jamburidze, M. De Corato, A. Huerre, A. Pommella, V. Garbin, *Soft matter* **2017**, *13*, 3946–3953.
- [34] I. Lentacker, I. De Cock, R. Deckers, S. De Smedt, C. Moonen, *Advanced drug delivery reviews* **2014**, *72*, 49–64.
- [35] P. Marmottant, S. Hilgenfeldt, *Nature* **2003**, *423*, 153.
- [36] P. Marmottant, S. Hilgenfeldt, *Proceedings of the National Academy of Sciences* **2004**, *101*, 9523–9527.
- [37] F. Rosevear, *Journal of the American Oil Chemists' Society* **1954**, *31*, 628–639.
- [38] T. Oka, N. Ohta, *Langmuir* **2016**, *32*, 7613–7620.
- [39] A. Morozov, A. Zvelindovsky, J. Fraaije, *Physical Review E* **2000**, *61*, 4125.
- [40] L. Ramos, F. Molino, G. Porte, *Langmuir* **2000**, *16*, 5846–5848.



## Chapter 6

### Conclusions and future work

Soft polyhedral particles have been produced with a range of shapes based on variations of the cubic symmetry group and different modes of face growth. Cubosomes are formed from precursor emulsion droplets of lipid and solvent trapped in a yield stress fluid. Upon solvent removal, spherical droplets transform into faceted, highly elastic, but soft three-dimensional particles. The rate of face growth can be varied using straightforward variables like droplet size, temperature, and solubilized and adsorbed additives, to control shape. Time scales of particle growth vary from minutes to hours depending on the driving force for mass transport. Arrest of the system in a desired shape is possible by halting solvent removal, and we are pursuing the templating and polymerization of these shapes to produce solid particles.

The polyhedra created here are unique in that they possess solid-like faceting and shape, but also have a biologically-compatible liquid bicontinuous nanostructure that can encapsulate a wide range of solutes for delivery, reaction, and uptake functions. As a result, the particles can apply shape and structural properties over length scales from the molecular to the millimetric in one particle. The method may also provide a way to study other links between internal, molecular-scale structure and packing and the overall microscopic shape of particles. Far more complex faceting patterns could likely be produced on these particles by applying the insights of past single crystal phase mapping work, as well as the anisotropic methods explored here.

Microfluidic processes are currently being developed to produce these particles in a more continuous fashion so that their self-assembly behavior can be explored.

Hexosomes have been made in the same process from an emulsion precursor, which enables detailed study of structure and shape development during hexagonal liquid crystal formation. The micron-scale hexosomes predominantly form shapes with rotational symmetry, evoking one of several shapes formed by nanoparticle hexosomes. Study of the larger hexosomes also indicates that a significant degree of control over final particle shapes could be attained using experimental variables like droplet size, crystallization rate, and surfactant packing parameter. The findings can be used, to some extent, to explain past work on nanoparticle shape formation, though the lower boundaries of length scale found here match the upper extremes of nanoparticle hexosome sizes previously studied.

Both cubosomes and hexosomes have been polymerized to broadly extend the production of uniquely shaped colloids, and the application conditions of soft particles. This method demonstrates compatibility with a range of monomers with different properties. The monomers with larger hydrophobicity, DVB and HDDA, induce the formation of hexosomes, while the less hydrophobic monomers DEGDMA and EGDMA form cubosomes with aqueous monoolein. The hydrophilic monomer MBAm can diffuse inside cubosomes and hexosomes without affecting particle shapes. The shapes of these two types of particles, before polymerization, depend on the liquid crystalline phase and microstructure: hexosomes are biconical, and cubosomes are polyhedral. The shapes of polymerized particles are controlled by the initial shapes of the liquid crystalline templates. Whether hard or deformable particles are obtained depends on the choice of monomer. Hydrophobic monomers form hard particles, while hydrophilic monomers form elastic hydrogel particles, all preserving the original shape and symmetry of the liquid crystalline precursors. The

---

approach developed in this chapter is useful for synthesis of polymer microparticles of a variety of shapes, with different degrees of curvature and faceting, and a wide range of elasticities. The work broadens our ability to control colloid shape and will enable expanded studies of shape effects on flow, cell uptake and self-assembly.

The top-down method is the most common approach to make dispersed particles of cubosomes and hexosomes, but there is no clear guide to developing such a process without trial and error or over-design in order to achieve the desired size and shape of particles. A unique sample cell has been developed, enabling us to directly observe the process of bulk hexagonal phase breaking down into hexosomes in an ultrasonic field. The process of breaking down a bulk phase by ultrasonic dispersion occurs at extremely short time scales and is observed using high-speed imaging. Dispersion occurs as oscillating gas bubbles yield the surrounding liquid crystal phase, after which the liquefied region is dispersed into droplets. Shaped liquid crystalline particles then form by recrystallization of the dispersed droplets. The viscoelastic rheology of the liquid crystal is measured and shown to be adjustable over orders of magnitude by additive choice and process temperature, resulting in various responses to the applied ultrasonic energy as well as formation of different shapes with varying quality. Our observations explain the observed variations in particle shapes, and indicate that hexosomes produced by sonication are not the result of direct fragmentation but instead a process of liquefaction, dispersion, and refinement via recrystallization.

Overall, this thesis provides a systematic study of micron-scale cubosomes and hexosomes, involving preparation methods, direct observations, controlling shapes, and templating. These results give many insights, especially in shape formation and transition, that cannot be obtained from the majority of works on nanoscale cubosomes and hexosomes in this area. Our observations build a link between

particle shapes and microstructures, which also explains some of the variations in nanoscale particle shapes. This work is helpful to design controlled processes of shape formation of both hard and soft materials.

As an experimental toolkit, the bottom-up approach developed in this work can create widely variable particle shapes to achieve the ambitious vision set for faceted particle assemblies. Sophisticated hierarchical particle self-assembly can be realized not only by simulations, but also in experimental systems by using particles with different shapes as building blocks. This thesis doesn't include applications, but for future works, the shaped and soft particles can be used in many areas. Cubosomes and hexosomes are drug carriers in most works, they can also be carriers for enzyme, catalyst, and other active materials, acting as micro reactors. These liquid crystalline particles are visible in an optical microscope and have a large interfacial area. The reaction inside could be fast and indicated by a change in morphology. For polymerized particles, they are more stable and can be deformed and recover in shape, so they could mimic red blood cells, viruses, and organelles which have similar mechanical properties and anisotropic shapes. Polymerized particles can also be used in studying particle separation as their tunable elasticity, size, and shape may cause different flow behaviours.

However, there are still challenges in applications of cubosomes and hexosomes. The solute used in the bottom-up approach is generally an organic solvent, which is a problem for inclusion of drugs or bioactive substances in liquid crystalline particles. A future development would be exploring biological processes, for example enzymatic degradation, to drive the transition from droplets to structured particles. The limitation of this thesis is that nano-scale particles have not been studied. It is speculated that nano-scale cubosomes prepared via the bottom-up process also have polyhedral shapes, but cannot form as many shapes as what have been observed

---

in micro scale. Some facets with higher energy could disappear when the size is too small. It is also not clear whether nano-scale hexosomes could form the same biconical shapes as as their microscale counterparts. The packing of cylindrical micelles is related to the length scale, and the bending energy of micelles in rotating arrangements would be very high at the nano-scale. In addition, even in a yield stress fluid, nanoparticles may still need stabilizers like block copolymers which could affect particle shapes. Because of the difficulty of direct observation, nanosized cubosomes and hexosomes need more future works to bring a thorough understanding of the bottom up process.





## Appendix A

### Supplementary Figures for Chapter 3

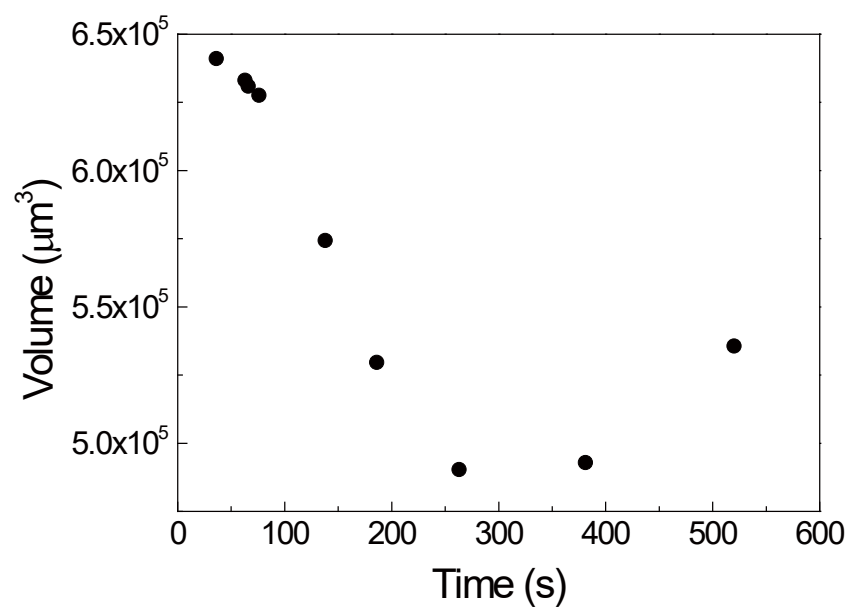


*Figure A.1: The change of particle volume as a function of time during the transition process in Figure 3.3.*

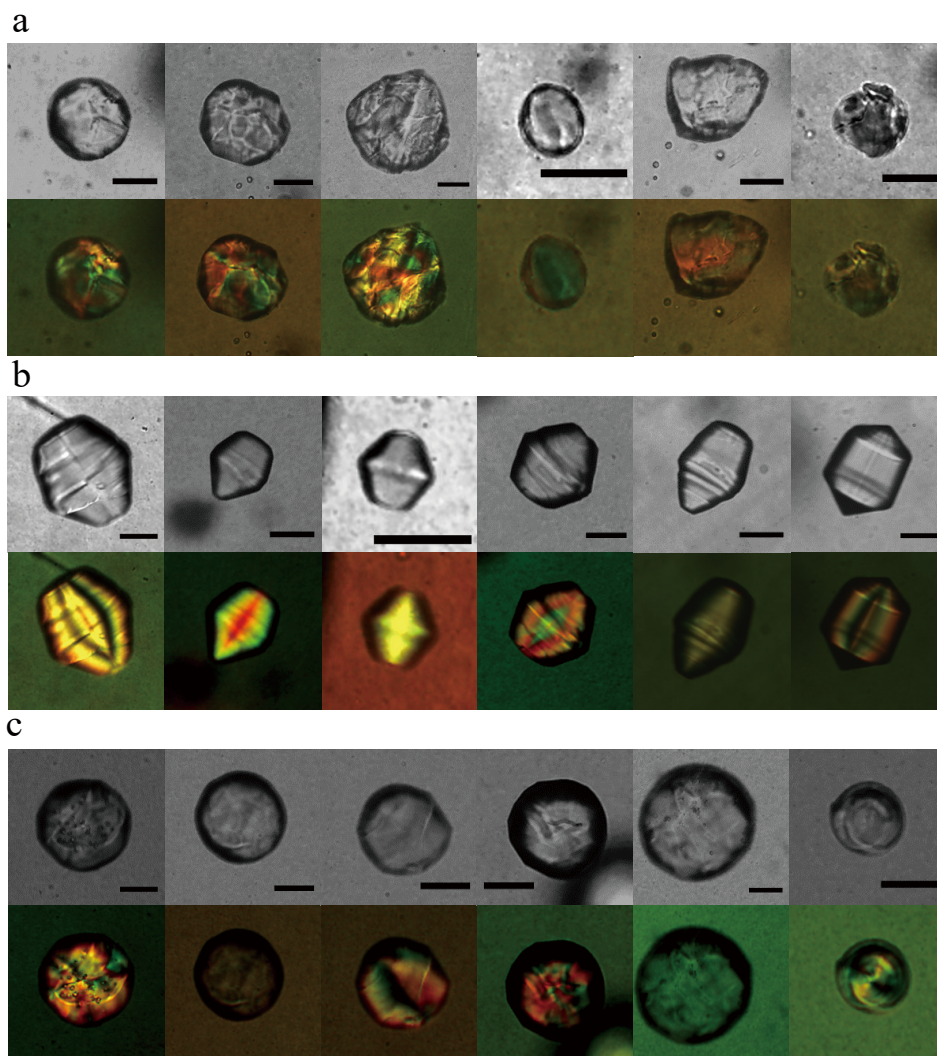


**Figure A.2:** Additional microscope images of hexosomes with different levels of DVB additive. The precursor solutions contain  $n_{\text{DVB}} = 0.2$  (a), 0.6 (b), and 1 (c). The top image is under bright field and the bottom is under polarized light. Scale bar is 50  $\mu\text{m}$ .

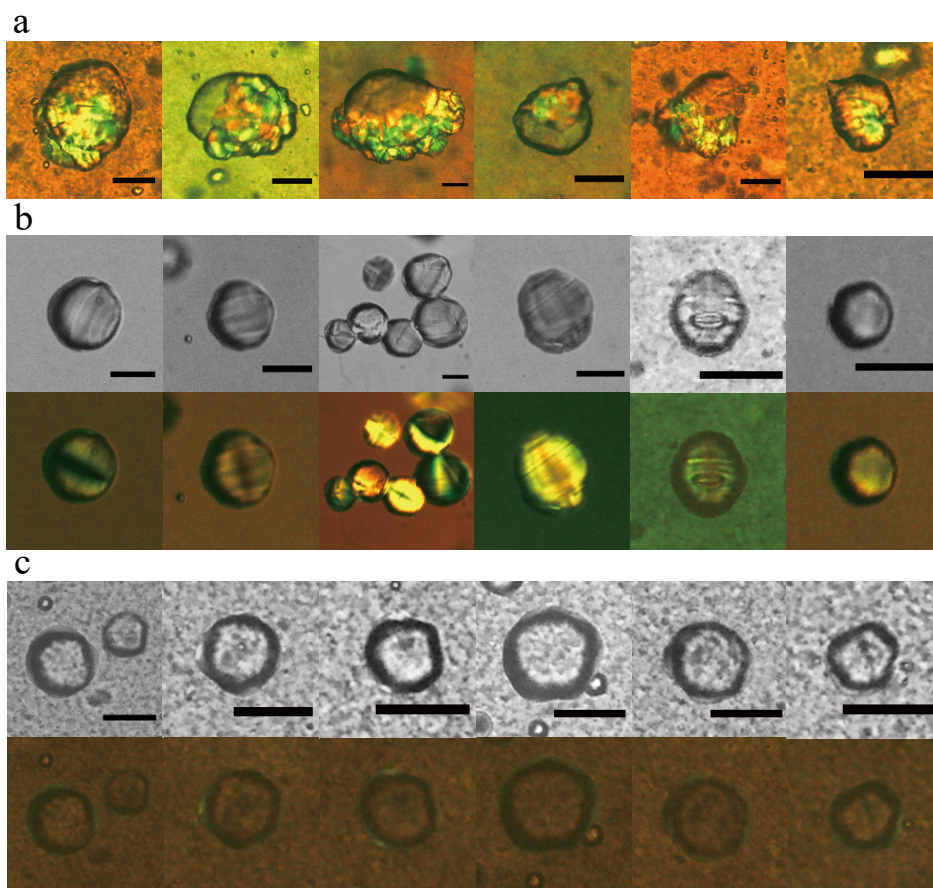


**Figure A.3:** Additional microscope images of hexosomes with different levels of vitamin E additive. The weight ratio of vitamin E and monoolein are  $n_{\text{vitE}} = 0.05$  (a), 0.2 (b), and 0.5 (c). The top image is under bright field and the bottom is under polarized light. Scale bar is 50  $\mu\text{m}$ .



## Appendix B

### Supplementary Figures for Chapter 4

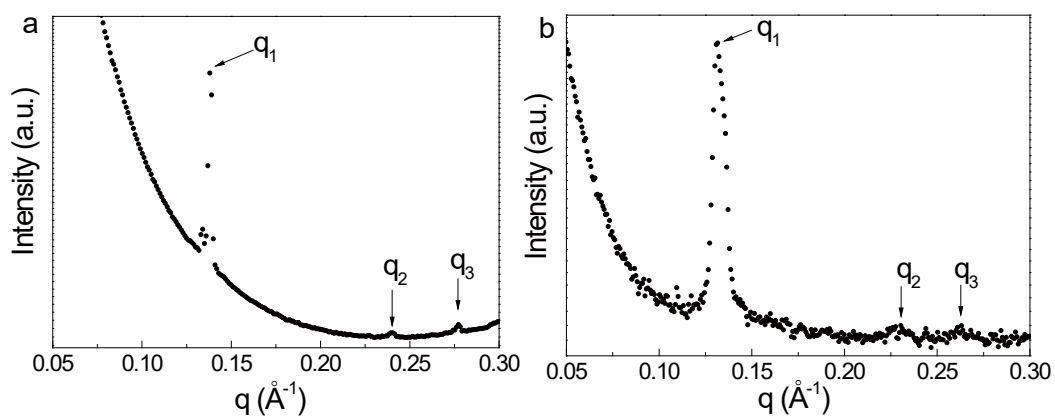


**Figure B.1:** SAXS for particles with  $\mu_{DVB} = 0.6$  before (a) and after polymerization (b),  $q_1 : q_2 : q_3 = \sqrt{1} : \sqrt{3} : \sqrt{4}$ .

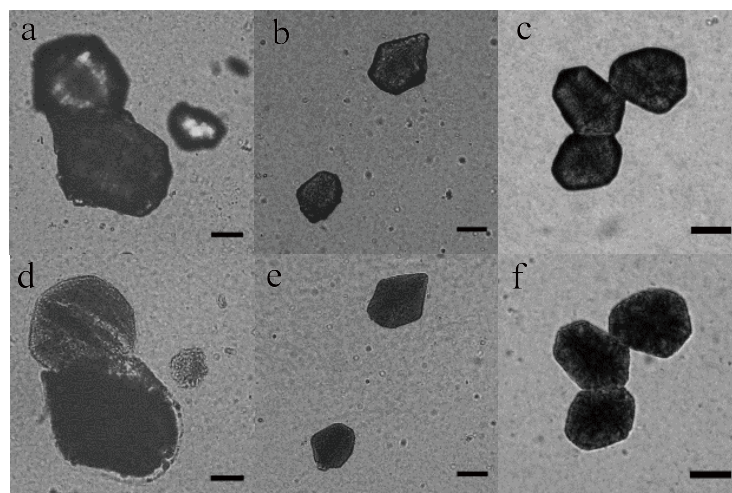


**Figure B.2:** Polymerized particles with  $\mu_{DVB} = 0.4$  (a, d),  $0.6$  (b, e), and  $0.8$  (c, f), before (a-c) and after (d-f) removing monoolein. The mass ratio of DVB to PI  $m_{DVB} : m_{PI} = 10 : 1$ . Scale bar is  $50 \mu\text{m}$ .

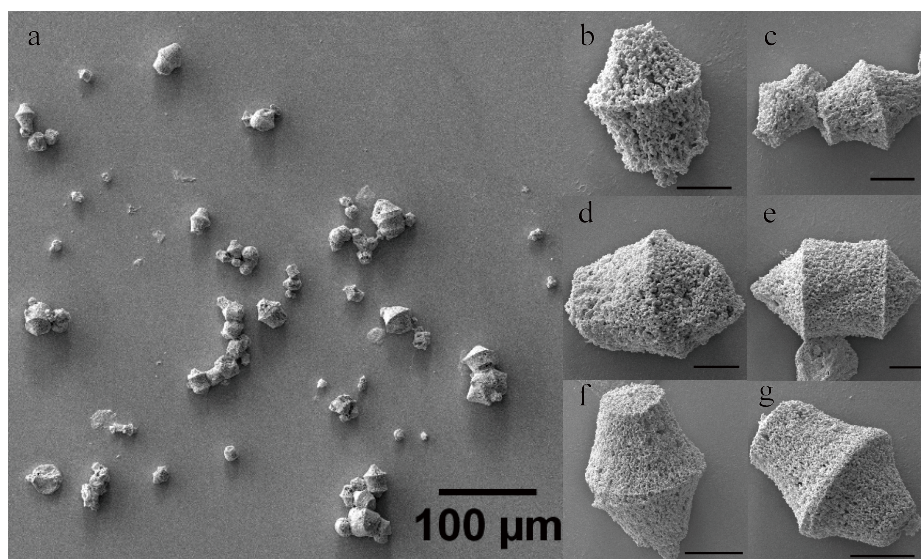


**Figure B.3:** SEM micrographs of polymerized hexosomes, mass ratios  $m_{\text{monoolein}} : m_{\text{DVB}} : m_{\text{PI}} = 1 : 0.8 : 0.08$ . Scale bar is 10 μm in (b-e) and 20 μm in (f and g).

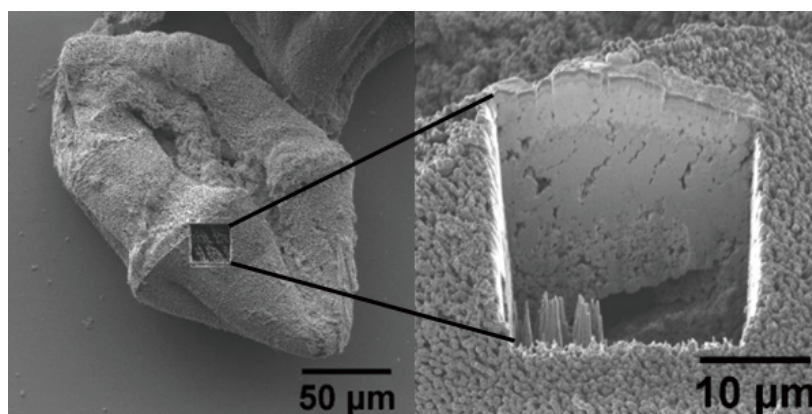


**Figure B.4:** Polymer particles after treatment by FIB, the cross-sectional view reveals the thickness of the particle wall and the uniformity of its polymeric structure. The well-defined nanoparticle morphology on the exterior of the particle is less obvious when viewing the cross-section of the "walls" of the hole – this may be caused by the Pt coating and a "smearing" effect during the ion beam treatment.

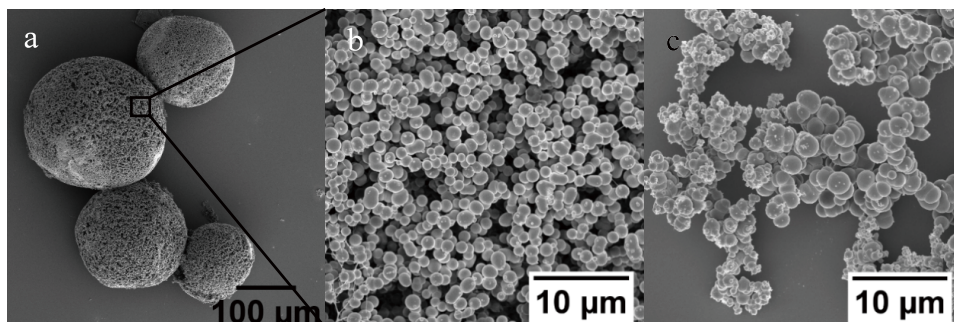


**Figure B.5:** SEM micrographs of (a), (b) polymerized emulsion droplets without hexagonal phase inside and (c) the undispersed precursor solution of monoolein, DVB, photoinitiator, and ethanol. Mass ratio  $m_{\text{monoolein}} : m_{\text{DVB}} : m_{\text{photoinitiator}} = 1 : 0.6 : 0.03$ .

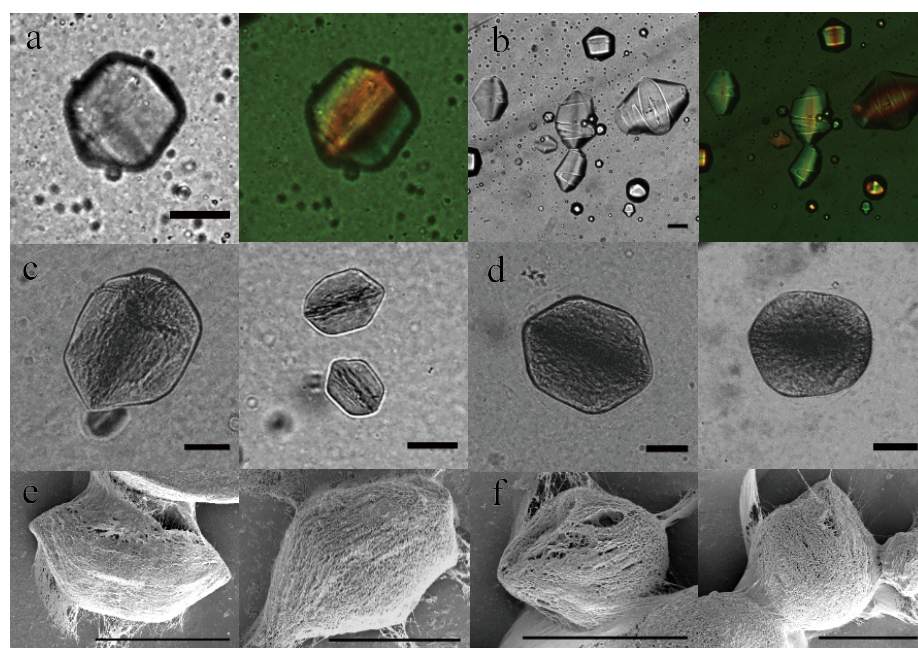


**Figure B.6:** Optical microscope images of hexosomes with inclusion of the monomer HDDA before (a), (b) and after (c), (d) polymerization, black-and-white images are taken under bright field, the colorful ones are under polarized light; SEM micrographs of polymerized hexosomes (e), (f). Each label indicates two images. Mass ratios  $m_{\text{monoolein}} : m_{\text{HDDA}} : m_{\text{PI}} = 1 : 0.2 : 0.02$  (a), (c), (e) and  $1 : 0.4 : 0.04$  (b), (d), (f). Scale bar is  $50 \mu\text{m}$ . Fibers observed are leftover unwashed cellulose used to give the dilution liquid a weak yield stress, and does not affect the observation of polymerized hexosomes.

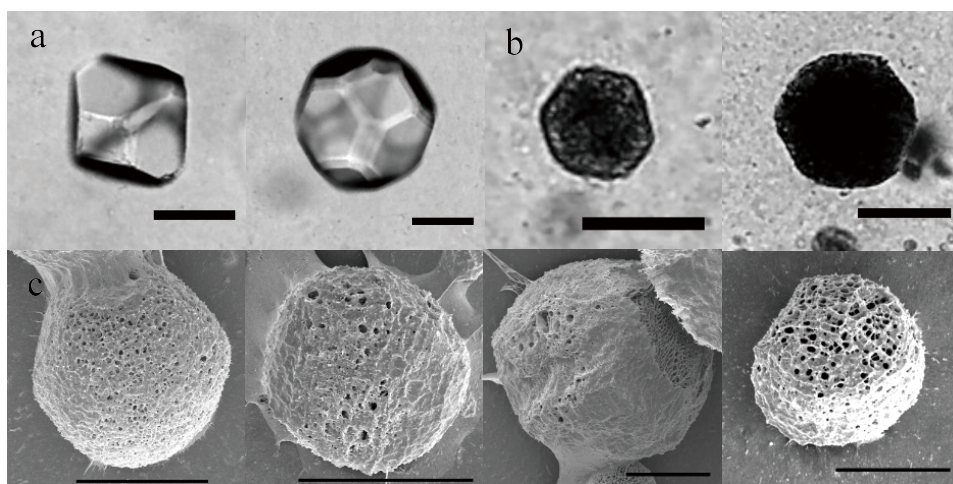


**Figure B.7:** Microscopy of hexosomes with inclusion of monomer EGDMA before (a) and after polymerization with removing the template (b); SEM micrographs of polymerized particles (c). The mass ratios,  $m_{\text{monoolein}} : m_{\text{EGDMA}} : m_{\text{photoinitiator}} = 1:0.6:0.03$ . Scale bar is  $50 \mu\text{m}$ .

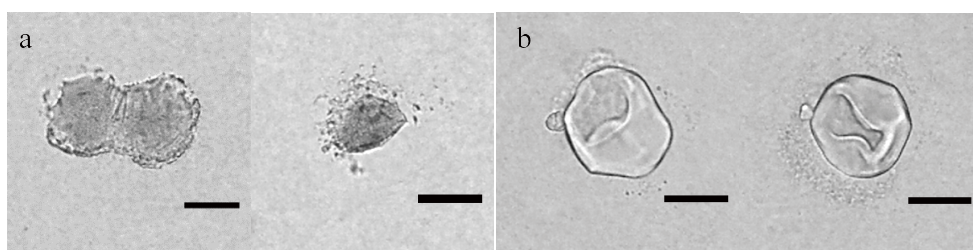


**Figure B.8:** Polymeric cubosomes after removing template with  $c_{\text{MBA}_m} = 0.4\%$  (a) and  $0.8\%$  (b), and mass ratio of PI to monoolein  $m_{\text{PI}} : m_{\text{monoolein}} = 0.04$ . Scale bar is  $50 \mu\text{m}$ .



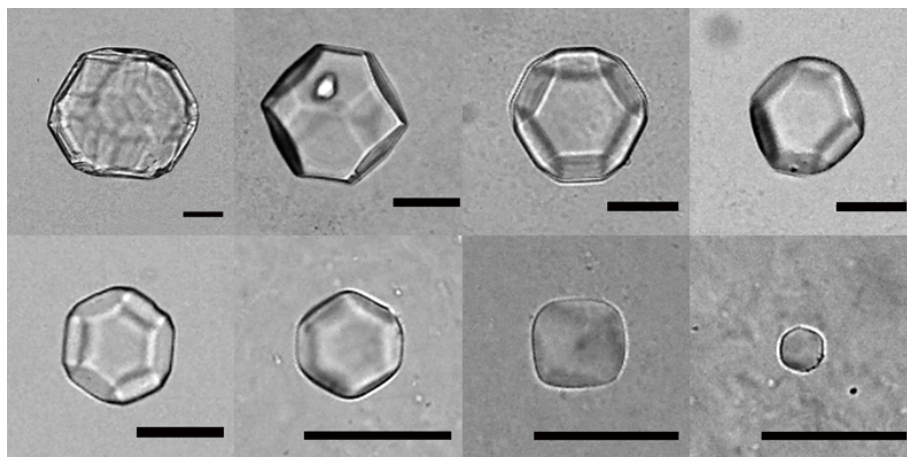


**Figure B.9:** Polymeric cubosomes in different sizes after removing template,  $c_{MBAm} = 2.4\%$ ,  $m_{PI} : m_{monoolein} = 0.04$ . Scale bar is  $50 \mu\text{m}$ .

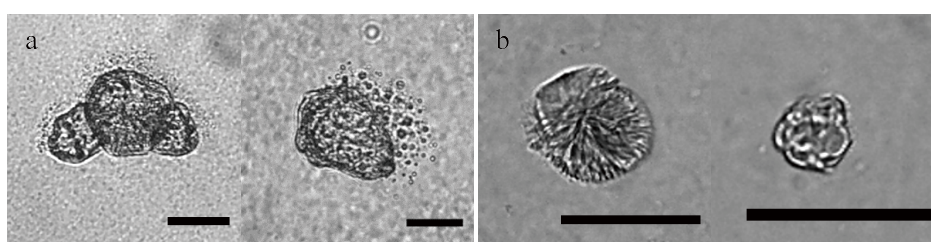


**Figure B.10:** Polymeric hexosomes that are not polymerized completely, hexadecane is the hydrophobic additive with a mass ratio  $m_{monoolein} : m_{hexadecane} = 1:0.2$ , and MBAm is the monomer with the concentration  $c_{MBAm} = 1.6\%$ , mass ratio of PI to monoolein is  $m_{PI} : m_{monoolein} = 0.06:1$  (a) and  $0.04:1$  (b). Scale bar is  $50 \mu\text{m}$ .